



Skolkovo Institute of Science and Technology

Skolkovo Institute of Science and Technology

ASPECTS OF LASER-INDUCED STRUCTURING AND SURFACE
MODIFICATION OF TECHNOLOGICALLY SIGNIFICANT METAL AND
SEMICONDUCTOR MATERIALS

Doctoral Thesis

by

IGOR SALIMON

DOCTORAL PROGRAM IN PHYSICS

Supervisor

Assistant Professor Sakellaris Mailis

Moscow – 2023

© Igor Salimon 2023

I hereby declare that the work presented in this thesis was carried out by myself at Skolkovo Institute of Science and Technology, Moscow, except where due acknowledgement is made, and has not been submitted for any other degree.

Candidate (Igor A. Salimon)

Supervisor (Prof. Sakellaris Mailis)

Abstract

Laser writing is a well-established technique used to modify and synthesize materials for a wide variety of applications. Some examples include laser cutting, laser welding, laser 3D micromachining and laser cladding. Compared to other methods such as chemical vapor deposition or electron beam lithography, laser writing possesses several key benefits. Namely, laser processing is coincidentally a patterning method, and it may be realized in ambient conditions. This could be highly attractive for economics and logistics of mass industrial production or rapid prototyping in laboratories.

Discoveries in novel materials (namely, transitional metal dichalcogenides (TMDCs) and porous silicon) and characterization techniques call to revisit laser writing in terms of overall research flow “synthesis (fabrication) – post-processing – structure characterization – performance testing – applications.”

This research was aimed, in particular, at characterizing topographical, structural and chemical changes occurring in a selection of materials under pulsed laser scanning and continuous wave (non-pulsed, c.w.) laser scanning in context of developing simple methods of surface modification. .

Laser-induced chemistry and topography modification was investigated in regards to processing of technologically important materials, such as GaAs crystals and aluminum alloys.

We observed laser-induced periodic surface structures (LIPSS) on GaAs crystals, formed by periodically preferential oxidation. Additionally, we obtained and studied deep porous oxide layers on GaAs using X-ray photoelectron spectroscopy (XPS) and focused

ion beam – scanning electron microscopy (FIB-SEM) cross sections. This suggests new approaches for controlled localized oxidation of GaAs, used for creating metal-oxide-semiconductor (MOS) devices and for conversion of GaAs oxide towards Ga_2O_3 .

We investigated re-deposition of ablated material during ultrashort pulse ablation of the widely used D16T alloy of aluminum. For irradiation protocols that combine several repetitions of the scanning pattern and energy fluences above 13 J/cm^2 , self-assembled conical structures are formed, reaching heights of $30 \text{ }\mu\text{m}$. FIB-SEM study along with energy dispersive x-ray spectroscopy (EDX) revealed the internal contents of such conical microstructures, showing a non-uniform oxidized layer formed by redeposited material.

We developed the novel method of synthesis of transitional metal dichalcogenides (TMDCs) from thin precursor films by direct laser writing. During rapid local thermal decomposition of the film, we observed the LIPSS phenomenon, which we exploited to demonstrate direct synthesis of regular periodic arrays of MoS_2 nanoribbons.

Such nanostructured MoS_2 films exceed the photoconductivity of non-structured films by three orders. We attribute this to the modification of the defect content, as nanostructured film is known to contain trap states in the bandgap due to higher proportion of edge area. This work shows a route to improve the photoelectric properties of TMDCs obtained with a simple, quick and widely available synthesis method.

Publications

1. I. A. Salimon, E. V. Zharkova, A.V. Averchenko, J. Kumar, P. Somov, O. A. Abbas, P. G. Lagoudakis, S. Mailis, Laser-Synthesized 2D-MoS₂ Nanostructured Photoconductors. *Micromachines*, vol. 14, p. 1036, 2023.
2. I. A. Salimon, A.V. Averchenko, S. A. Lipovskikh, E. A. Skryleva, A. V. Novikov, P. G. Lagoudakis, S. Mailis, UV laser-induced nanostructured porous oxide in GaAs crystals, *Solid State Sciences*, vol. 128, p. 106887, 2022.
3. I. A. Salimon, S. Mailis, A. I. Salimon, E. Skupnevskiy, S. A. Lipovskikh, I. Shakhova, A. V. Novikov, T. F. Yagafarov, A. M. Korsunskiy, FIB-SEM Investigation of Laser-Induced Periodic Surface Structures and Conical Surface Microstructures on D16T (AA2024-T4) Alloy, *Metals*, vol. 10, p. 144, 2020.

Acknowledgements

I would like to express my profound gratitude to my scientific and co-advisors for their belief in me and full support during the entire PhD program. I would not have been able to complete this project without the support of my scientific advisor Prof. Sakellaris Mailis, my colleagues Aleksandr V. Averchenko, Ekaterina V. Zharkova and Omar A. Abbas, the wider Polaritonics group, CPSE, HSM and CEST. Lastly, big thanks to all family and friends who supported me during this program.

Table of Contents

Abstract.....	3
Publications.....	5
Acknowledgements.....	6
Table of Contents.....	7
List of Symbols, Abbreviations	12
List of Figures.....	14
List of Tables	19
Chapter 1. Introduction.....	20
1.1 Lasers for material modification.....	20
1.2 Lasers and laser-material interaction	21
1.2.1 <i>Light Amplification by Stimulated emission of Radiation (LASER).</i>	21
1.2.2 <i>Absorption of ultrashort laser pulses.</i>	22
1.2.3 <i>Non-linear processes in ultrashort pulses.</i>	24
1.2.4 <i>Relaxation or ultrashort laser pulses.</i>	27
1.2.5 <i>Concluding remarks</i>	30
1.3 State of the art in relevant fields	31
1.3.1 <i>Laser-induced periodic surface structures (LIPSS)</i>	31
1.3.2 <i>Existing theories on LIPSS formation</i>	32
1.3.3 <i>Applications of LIPSS</i>	41
1.3.4 <i>Direct laser interference patterning (DLIP) compared to LIPSS</i>	41
1.3.5 <i>Conical microstructures</i>	42

1.3.6 GaAs.....	43
1.3.7 AA2024-T4 (D16T)	46
1.3.8 2D-TMDCs.....	47
1.3.8 Synthesis methods for 2D-TMDCs.....	50
1.3.9 Porous Silicon	53
1.4 Methodology	55
1.4.1 Laser writing setup	56
1.4.2 Laser synthesis of MoS ₂ films	57
1.4.3 Bright Field and Dark Field Optical Microscopy	59
1.4.4 Scanning Electron Microscopy (SEM).....	60
1.4.5 Energy Dispersion X-Ray Spectroscopy (EDX).....	63
1.4.6 Focused Ion Beam (FIB, FIB-SEM) imaging and etching for cross section and lamellae preparation.....	64
1.4.7 Time of flight secondary ion mass spectroscopy (ToF-SIMS)	66
1.4.8 X-ray Photoelectron Spectroscopy (XPS).....	67
1.4.9 Chromatic confocal profilometry.....	68
1.4.10 Atomic Force microscopy (AFM)	70
1.4.11 Raman spectroscopy	70
Chapter 2. Laser processing of technological materials: FIB-SEM characterization.....	72
2.1 Individual contributions	72
2.2 Chapter summary	72
2.3 Localized laser oxidation of GaAs crystals	74

2.3.1	<i>Experimental procedures</i>	74
2.3.2	<i>SEM surface topography investigation</i>	75
2.3.3	<i>AFM surface topography investigation</i>	80
2.3.4	<i>FIB-SEM and EDX examination of internal composition of deep porous oxide layers</i>	81
2.3.5	<i>XPS examination of elementary content</i>	83
2.3.6	<i>Concluding remarks</i>	90
2.4	Surface modification of aluminum alloy by femtosecond pulsed laser scanning	91
2.4.1	<i>Femtosecond laser irradiation of D16T sample</i>	92
2.4.2	<i>Confocal profilometry of ablated areas</i>	96
2.4.3	<i>SEM surface topography investigation</i>	100
2.4.4	<i>FIB-SEM and EDX examination of internal composition of conical microstructures</i>	103
2.4.5	<i>Study of optical properties of ablated areas</i>	109
2.4.6	<i>Concluding remarks</i>	110
Chapter 3.	Laser-assisted production of nanostructured 2D-TMDCs	112
3.1	Individual contributions	112
3.2	Chapter summary	112
3.3	Laser irradiation parameters	113
3.4	Parametric study of LIPSS formation	115
3.4.1	<i>Laser-irradiated track morphology</i>	115
3.4.2	<i>Linear 1D LIPSS and formation of nanoribbons</i>	120

3.4.3 2D LIPSS.....	127
3.4.4 Experiments with variable scanning speed.....	129
3.4.5 Role of SiO ₂ layer in LIPSS formation.....	134
3.5 Properties of MoS ₂ 1D LIPSS.....	138
3.5.1 AFM scanning.....	138
3.5.2 Raman spectroscopy.....	139
3.5.3 Photoconductivity characterization.....	140
3.6 Concluding remarks.....	147
Chapter 4. Laser-induced densification of porous silicon.....	148
4.1 Individual contributions.....	148
4.2 Chapter summary.....	148
4.3 Details of experiment.....	149
4.4 Observations on rapid laser scanning of porous silicon.....	150
4.4.1 Observations of 532 laser scan tracks.....	150
4.4.2 Observations of 244 laser scan tracks.....	154
4.4.3 FIB etching and ToF-SIMS characterization of laser scan tracks.....	160
4.5 Concluding remarks.....	172
Chapter 5. Patterning of precursor films for TMDC synthesis by e-beam scanning.....	173
5.1 Individual contributions.....	173
5.2 Chapter summary.....	173
5.3 Patterning of precursor films for TMDC synthesis by e-beam scanning.....	175
5.4 Laser synthesis of patterned MoS ₂ features from patterned precursor films.....	183

5.5 Concluding remarks	186
Conclusions	188
Bibliography	192

List of Symbols, Abbreviations

LIPSS – Laser Induced Periodic Surface Structures

LIFT – Laser Induced Forward Transfer

μ SLA – microstereolithography

MAP – Multiphoton Absorption Polymerization

Q-factor – Quality factor (of laser resonator)

c.w. – Continuous Wave (non-pulsed uniform output of lasers)

LSFL – Low Spatial Frequency LIPSS

HSFL – High Spatial Frequency LIPSS

TLIPSS - Thermochemical LIPSS

UV – ultraviolet

IR – infrared

SEM – Scanning Electron Microscopy

FIB – Focused Ion Beam

AFM – Atomic Force Microscopy

EDX (also EDS, EDAX) – Energy-Dispersive X-ray Spectroscopy

XPS – X-ray Photoelectron Spectroscopy

TMDC – Transitional Metal DiChalcogenide

BF – Bright Field

DF – Dark Field

SE – Secondary Electrons

BSE – Back-Scattered Electrons

I_{PC} – Photocurrent

DMF – Dimethylformamide

V_{CPD} – Contact Potential Difference

ToF-SIMS – Time of Flight Secondary Ion Mass Spectroscopy

DLIP – Direct Laser Interference Patterning

MPI – MultiPhoton Ionization

MPA – MultiPhoton Absorption

List of Figures

Figure 1 Schematic outlining the characteristic time scales of processes involved in ultra short pulse laser irradiation [24].	24
Figure 2 a) Interference of incident light with light scattered from single defect (modelled as an emitting dipole), b) cross sections of the intensity distribution from (a). Blue line is the cross section along x and the incident polarization, red line is the cross section along y and perpendicular to the incident polarization. Reproduced from [59].	39
Figure 3 Schematic of laser writing setup.....	56
Figure 4 A laser-irradiated track containing LIPSS features in bright field and dark field modes of imaging.....	60
Figure 5 Principle of chromatic confocal profilometry [188].....	69
Figure 6 a) SEM image of laser-induced topography modifications corresponding to a single laser-irradiated track. The Gaussian intensity distribution of the laser beam allows the simultaneous observation of laser-induced porosity (at the central region of the track) and laser-induced periodic surface structures (LIPSS) at the periphery of the track. The polarization of the beam is perpendicular to the scanning direction. b) SEM image of GaAs surface topography changes observed on a single track with polarization parallel to the scanning direction. c) Regular LIPSS patterns are formed throughout the width of the track using appropriate irradiation conditions. The laser scanning direction is indicated by the white outline arrow, while the solid white double arrowhead lines indicate the polarization of the irradiating beam.	76
Figure 7 Distortion in the LIPSS patterns observed after static laser beam exposure of an area with a surface defect (crack with a zigzag-like trajectory).	79
Figure 8 LIPSS produced by expanding the beam spot during laser scanning. The laser scanning direction is indicated by the white outline arrow, while the solid white double arrowhead line indicates the polarization of the irradiating beam.	79
Figure 9 AFM topography map of a single track section with LIPSS. The peak laser intensity used for the UV laser irradiation was 12 kW/cm ² and the scanning speed was 6 μm/s.	80
Figure 10 a) SEM image of the uniform porous layer obtained by overlapping adjacent laser tracks. Inset: Cross section of the porous GaAs layer viewed at an angle of 52°. The cross section was produced using FIB etching. The unaffected GaAs crystal can be seen under the porous layer. b) Plot of oxygen, gallium and arsenic levels, as a function of position, acquired along a line that is parallel to the surface. That line begins on the irradiated area and crosses the border between the irradiated area and virgin surface at the 35 μm mark. The corresponding sections on the plot are: irradiated 0 - 35 μm, non-irradiated 35 - 65 μm.	81
Figure 11 Survey spectra of a non-irradiated area a) before and b) after purification.....	84
Figure 12 Survey spectra of the laser-irradiated area a) before and b) after purification.	85
Figure 13 Survey spectra of a) a non-irradiated area after 4.2 min of Ar ⁺ 1 keV ion etching and b) the laser-irradiated area after 4.2 min of Ar ⁺ 1 keV ion etching and 9 min of Ar ⁺ 2 keV.....	86

Figure 14 a,b) Concentration profiles, estimated by XPS, for Ga, As and O on: (a) non-irradiated area and (b) UV laser raster scanned area, as a function of etching time. c-f) High resolution XPS spectra of the binding energy (BE) of Ga3d and As3d. Spectra c, d correspond to the non-irradiated crystal surface. Spectra e, f correspond to the laser-irradiated area. Solid black lines correspond to experimental spectra, blue dash lines correspond to fitted GaAs peak, red dash lines correspond to fitted oxide peaks. 87

Figure 15 Layout and principal geometry characteristics of laser treatment: (a) photograph of the top surface of the cylindrical D16T sample, with the various irradiated areas marked; (b) laser scan schematic diagram, with space coordinate system shown and scanning (long arrows) and scan progression (short arrows) directions indicated; (c) typical treated area schematic, with typical profiles shown. 94

Figure 16 Typical ablation profiles for 21 J/cm². The profiles shown here correspond to an area that was subjected to three scan repetitions (SR): (a) longitudinal profile of treated area; (b) transversal profile of treated area. 96

Figure 17 Profiles of laser-treated areas: (a) color-coded chart; (b) example profile for “green” profiles which are parallel to the initial surface; (c) example profile for “yellow” profiles with an observable slope; (d) example profile for “red” profiles with high roughness. SR: scan repetitions. 98

Figure 18 Profile parameters: a) depth of laser-treated areas at 160 μJ; (b) average slope angle of treated area bottom. 99

Figure 19 SEM images showing appearance of ablated areas (top view). 101

Figure 20 SEM images corresponding to an energy fluence of 9 J/cm² and five scan repetitions. (a) SEM image demonstrating semi regular LIPSS; (b) SEM close-up on LIPSS features, revealing a granular structure (observed at a 52° sample tilt). 103

Figure 21 SEM images of conical microstructures corresponding to an energy fluence of 33 J/cm² and five scan repetitions: (a) conical microstructures (observed at a 52° sample tilt) with an impurity particle and the site of FIB milling; (b) close-up of the conical structures’ slopes with the contrast enhanced, ripples are observable (observed with 52° sample tilt); (c) tip of a conical microstructure before cleaning in acetone; (d) slope of a conical microstructure after cleaning in acetone; (e) internal content of a conical structure sectioned in half by FIB (observed with 52° sample tilt), a protective layer of platinum is deposited on top. 105

Figure 22 FIB sectioning of a cone formed by laser ablation treatment at 33 J/cm² with five scan repetitions: (a) SEM image of FIB-cut conical structure; (b) EDX showing Al concentration inside the FIB-cut conical structure; (c) EDX showing O concentration inside the FIB-cut conical structure; (d) EDX showing Cu concentration inside the FIB-cut conical structure; (e) SEM image of lamella cut from the conical structure; (f) EDX showing Al concentration inside the lamella cut from the conical structure; (g) EDX showing O concentration inside the lamella cut from the conical structure; (h) EDX... 108

Figure 23 AFM image corresponding to a section of a single laser-irradiated track, the overlay shows the thickness profile of the track along the dash line [165] 117

Figure 24 SEM images showing a) SEM images showing (a) continuous MoS₂ film; (b) film with periodically modulated thickness (1D LIPSS); (c) 1D LIPSS formed with beam polarization oriented along the direction of scanning; and (d) 2D LIPSS. The laser

scanning direction is indicated by the white outline arrow, while the solid white double arrowhead lines indicate the polarization of the irradiating beam. The track runs along the horizontal direction corresponding to a section of a single laser-irradiated track, the overlay shows the thickness profile of the track along the dash line.....	118
Figure 25 a) SEM image of LIPSS formation in a laser synthesized WS ₂ track, b) corresponding Raman spectrum showing the in- and out- of plane vibrational modes, typical for WS ₂ . The laser scanning direction is indicated by the white outline arrow, while the solid white double arrowhead lines indicate the polarization of the irradiating beam.....	120
Figure 26 SEM images showing an over-developed track with one side-lobe (bottom part of the image) partially detached from the substrate, leading to detachment and bending of nanoribbons. SEM images produced by Somov P.....	123
Figure 27 Series of SEM close-ups showing an over-developed track with one side-lobe (bottom part of the image) partially detached from the substrate, leading to detachment of nanoribbons. Smaller irregular structures were observed between the periodic nanoribbons. SEM images produced by Somov P.....	124
Figure 28 SEM images of laser-irradiated tracks showcasing 1D LIPSS length and width depending on laser beam intensity.....	126
Figure 29 Close-up SEM images of laser-irradiated tracks showcasing 1D LIPSS length and width depending on laser beam intensity.....	127
Figure 30 SEM images of 2D LIPSS structures produced using the irradiating laser intensities of (a) 0.51 MW/cm ² , (b) 0.64 MW/cm ² , (c) 0.76 MW/cm ² , and (d) 0.89 MW/cm ² . The laser scanning direction is indicated by the white outline arrow, while the solid white double arrowhead lines indicate the polarization of the irradiating beam. The insets correspond to a Fourier transform of the 2D LIPSS pattern.....	128
Figure 31 Parameter maps (laser intensity, scanning speed) indicating the regions where various types of LIPSS formation were observed on scanned films prepared with a) 24 mM, b) 32 mM, c) 40 mM, and d) 48 mM precursor solution concentrations. The color key for the various observations is shown as an inset on a).	131
Figure 32 1D to 2D LIPSS transition caused by a defect of the film (scanning direction is from bottom to top). The laser scanning direction is indicated by the white outline arrow, while the solid white double arrowhead lines indicate the polarization of the irradiating beam.....	133
Figure 33 Features obtained on non-layered substrates: a,b) crystalline Si wafers without SiO ₂ layer, c) crystalline sapphire wafers, d) glass microscope slides,.....	135
Figure 34 SEM image showing an LIPSS pattern, which is formed directly on the SiO ₂ layer under intense irradiation. The surface is covered with debris, indicating the occurrence of direct optical damage, induced by the laser irradiation.	137
Figure 35 a) AFM scan of a section of laser-irradiated track produced with a scanning speed of ~ 8 mm/s, b) a topography contour extracted from the AFM image (along the black line on a)). The thickness of the uniform film was measured to be 4 nm.	138
Figure 36 a) AFM scan of a section of a nanostructured photodetector consisting of MoS ₂ nanoribbons, b) a topography contour extracted from the AFM image (along the black line on a)). The thickness of the nanoribbons may vary from 10 to 15 nm.	139

Figure 37 Raman spectra of nanostructured MoS ₂ tracks corresponding to a) 1D LIPSS and b) 2D LIPSS obtained for a variety of parameters. The variety of synthesis parameters result in different film characteristics, i.e. thickness, which is reflected in the shifts of the A _{1g} and E _{2g} ¹ peaks.....	140
Figure 38 Schematic of a photodetector device.....	141
Figure 39 (a) AFM image of the nanostructured device. The central section consists of an array of isolated nanoribbons enveloped by a pair of metal (Au) electrodes (top and bottom); (b) temporal evolution of photocurrent (growth and decay when excitation laser is switched on and off, respectively) for 650 and 450 nm excitation, at the same power (5.3 μW); (c) saturation values of the photocurrent as a function of incident power for 650 and 450 nm excitation, for nanostructured (LIPSS) and continuous devices; (d) decay curves of the photocurrent corresponding to 450 nm (top graph) and 650 nm (bottom graph) excitation, for various excitation powers.....	142
Figure 40 Optical microscope top view of 532 nm laser scan tracks obtained under laser intensity of 2.16 MW/cm ² for various scanning speeds.	152
Figure 41 FIB cross-sections of 532 nm laser-irradiated tracks obtained using laser intensity of 0.57 MW/cm ² for various scanning speeds. As shown in the figure, at the top of the cross-sections is a protective layer of Pt deposited on the surface of the PorSi layer to facilitate producing a smooth surface of the cross-section. In the middle is the PorSi layer. Lastly, at the bottom of the images is the bulk Si crystal. SEM images were produced by Lipovskikh S. A.	153
Figure 42 SEM images of FIB-produced cross-sections of 244 nm laser-irradiated tracks obtained using two different laser intensities (as indicated in the figure) for a scanning speed of 256 μm/s. SEM images were produced by Lipovskikh S. A.	155
Figure 43 SEM images of cleaved edges showing cross sections of laser-irradiated tracks, indicating the effect of laser intensity (at 244 nm) for a constant scanning speed of 180 μm/s.	156
Figure 44 SEM image showing cleaved edges of laser irradiated tracks (at 244 nm) obtained using laser intensity of 30.96 kW/cm ² and various scanning speeds, as indicated in the figure.	158
Figure 45 Stylus profilometry data: Stylus profilometry data: a) depth of surface recess, b) width of the surface recess at half depth.....	159
Figure 46 SEM images showing 30 × 30 μm ² areas etched by ion beam milling. Close-ups show the interface between the PorSi layer and the bulk Si crystal underneath. The pits contain sections of laser-irradiated tracks (at 244 nm) obtained using laser intensity of 30.96 kW/cm ² for various scanning speeds as indicated in the figure. SEM images were produced by Somov P.	161
Figure 47 O ⁻ signal collected during etching the pits on Figure 46: front projection with areas (center, left side and right side) selected and depth profiles of oxygen concentration collected in the selected areas.	164
Figure 48 Depth profile of O ⁻ signal collected during etching the pit on Figure 46a corresponding to 500 μm/s. FIB images (gray) and front projections of O ⁻ signal collected (colored) provided for specific etching frames.....	167

Figure 49 FIB topography images collected during etching the pit on Figure 46a. The frame numbers as indicated in the figure show a sequence of 9 frames of etching.....	169
Figure 50 Estimated resistance to ion milling for 244 nm laser scan tracks obtained under laser intensity of 30.96 kW/cm ² for various scanning speeds.	171
Figure 51 Development process snapshots of e-beam irradiated precursor film (24 mM) corresponding to various development times in NMP solvent as indicated in the figure. Rectangular features with aspect ratios varying from 2:1 to 10:1 were pre-patterned using varying dose of electrons. E-beam irradiation conditions correspond to a) 1 nA and b) 10 nA e-beam currents.	176
Figure 52 Development process snapshots of e-beam irradiated precursor film (24 mM) corresponding to various development times in NMP solvent as indicated in the figure. Thin line features were pre-patterned using varying dose of electrons. E-beam irradiation conditions correspond to a) 1 nA and b) 10 nA e-beam currents.	177
Figure 53 Development process snapshots of e-beam irradiated precursor film (12 mM) corresponding to various development times in NMP solvent as indicated in the figure. Thin line features with aspect ratios varying from 2:1 to 10:1 were pre-patterned using varying dose of electrons. E-beam irradiation conditions correspond to a) 1 nA and b) 10 nA e-beam currents.	178
Figure 54 Development process snapshots of e-beam irradiated precursor film (12 mM) corresponding to various development times in NMP solvent as indicated in the figure. Thin line features were pre-patterned using varying dose of electrons. E-beam irradiation conditions correspond to a) 1 nA and b) 10 nA e-beam currents.	179
Figure 55 “Halo” features formed around overexposed rectangular features of patterned precursor film.....	181
Figure 56 Width as a function of exposure (irradiation) time for thin lines with a 50 μm length, corresponding to precursor films which have been produced with initial precursor solution concentrations of 24mM and 48 mM.....	182
Figure 57 Rectangular features consisting of selectively e-beam irradiated regions of (NH ₄) ₂ MoS ₄ precursor followed by development in NMP. The features have been laser-irradiated along the horizontal direction to locally synthesize MoS ₂	184
Figure 58 a) AFM image of a thin e-beam patterned line. The line was partially post-irradiated with a laser beam at a direction perpendicular to its length (across the line) with successive overlapping laser tracks to convert the precursor to MoS ₂ , b)Surface profiles corresponding to locations inside and outside the post-irradiated areas indicate the changes in height and width between the two areas. Red graph corresponds to area post-irradiated with laser, while the black graph, corresponds to the untreated patterned area. The locations of the two profiles are indicated by the two vertical lines 1 and 2.....	185
Figure 59 Raman spectra of MoS ₂ thin line features converted from patterned precursor thin line features, which have been produced at different e-beam irradiation conditions.	186

List of Tables

Table 1.....	93
Table 2.....	94
Table 3.....	114
Table 4.....	144
Table 5.....	145

Chapter 1. Introduction

1.1 Lasers for material modification

Lasers are widely used in industrial material processing [1]. Compared to other methods of material processing, such as mechanical machining [2], chemical milling [3], electrochemical machining [4], electrical discharge machining [5] etc. they possess several key benefits; i) Laser can reach high power intensities and be easily automated by using optical elements, ii) Due to high spatial and spectral coherency, laser allow to exploit optical phenomena such as interference [6], diffraction, multi-photon excitation [7] and LIPSS [8].

Common industrial examples of laser material processing include laser cutting [1], laser welding [9] and laser cladding [10].

Some materials synthesis methods involve the direct [11, 12] or indirect [13] use of lasers, i.e. in pulsed laser deposition. Lasers are ideal for surface modifications and are today widely used for the manufacturing of surface structures. Additionally, versatile 2D fabrication can be achieved through laser-induced forward transfer (LIFT) [14], which uses laser pulses to eject voxels of material from a film, which has been previously deposited onto a transparent substrate, to an arbitrary receiving substrate. 3D microfabrication on nanoscale features is also made possible by techniques such as microstereolithography (μ SLA) [15] and multi-photon absorption polymerization (MAP) [7]. These techniques utilize the ability to focus the laser beam inside the bulk of a photoresist layer and induce photopolymerization by simultaneous absorption of more than one photons that occurs preferentially in the high intensity volume of the focus.

While the above-mentioned methods achieve highly impressive results, these are top-down approaches, which require additional manufacturing steps or the use of complex equipment. For economic, logistical and environmental reasons, this research seeks to explore fabrication methods that exploit laser-related phenomena to achieve a bottom-up self-organization of material. Such methods could be simpler and more viable for low-cost large-scale production or rapid prototyping in research environments.

This work utilizes several possible avenues that involve laser writing: i) for the surface modification of bulk opaque materials (ultraviolet (UV) oxidation of GaAs and femtosecond ablation forming conical microstructures on aluminum alloys), ii) for the treatment of thin films (laser synthesis of MoS₂ from precursor films with simultaneous periodic submicron patterning) and iii) for the volume modification on transparent materials (UV densification of porous silicon).

1.2 Lasers and laser-material interaction

1.2.1 Light Amplification by Stimulated emission of Radiation (LASER).

Devices known as lasers are capable of emitting highly coherent light, which could be focused to obtain a high intensity. The operation of laser relies on the phenomenon of stimulated emission and requires a gain medium in which an inverse population of energy levels is created. This is achieved by supplying energy to the gain medium by optical or electrical pumping. Additionally, a laser device typically has a cavity (or resonator) with reflecting elements that allow laser radiation to pass through the gain medium multiple

times. In each such cycle, some part of energy is lost, either due to optical losses or due to being irradiated outside the laser cavity. A number which is equal to 2π times the portion of the total energy lost in one cycle is known as the Q factor of the laser. Depending on the parameters of the cavity, multiple modes of the laser irradiation with different phases can be present simultaneously.

By modifying the Q-factor of the resonator [16] or by phase locking of lasing mode trains [17], it is possible to modulate the intensity output of a laser system. Pulsed lasing may achieve extremely high intensities by reducing the amount of time needed to unleash the energy stored in the laser cavity. For example, the duration of the pulse can be as short as $5 \cdot 10^{-14}$ seconds, or 5 fs [18], and during the pulse peak intensities higher than $10^{19} \text{ W} \cdot \text{cm}^{-2}$ were reached [19].

1.2.2 Absorption of ultrashort laser pulses.

In light–matter interaction an incident photon may transfer its energy to an atom or molecule, exciting them and causing them to ascend to a higher energy level. A subsequent re-emission of a photon with that same energy is referred to as scattering. While scattering is a common process, the energy of the absorbed light can relaxate without scattering, for example, instead spent on increasing the thermal energy of the lattice, which is referred to as absorption [20].

Femtosecond pulses may be absorbed through linear and non-linear processes [21]; the first case is possible in metals and semiconductors with a bandgap lower than the energy

of incident photons, and the latter becomes relevant when a single photon is unable to excite an electron to the conduction band.

The energy of the pulse can be absorbed in a time as short as dozens of fs (1). The electrons (or carriers in general, since there exist electron-hole scattering and hole-hole scattering besides electron-electron scattering [22]) exchange energy between themselves on similarly short time scales, which can be as short as 10 fs [23]. The carrier-carrier scattering becomes faster with increasing carrier concentration. For example, in GaAs with an electron density of 10^{18} cm^{-3} the time of electron-electron scattering can be as short as 20 fs. Establishing a thermal equilibrium of the free carriers could take a few hundred femtoseconds [22]. This can be viewed as carrier thermalization, electrons reaching a thermal equilibrium at a temperature T_e . The temperature of the ions in the lattice T_i may be temporarily different.

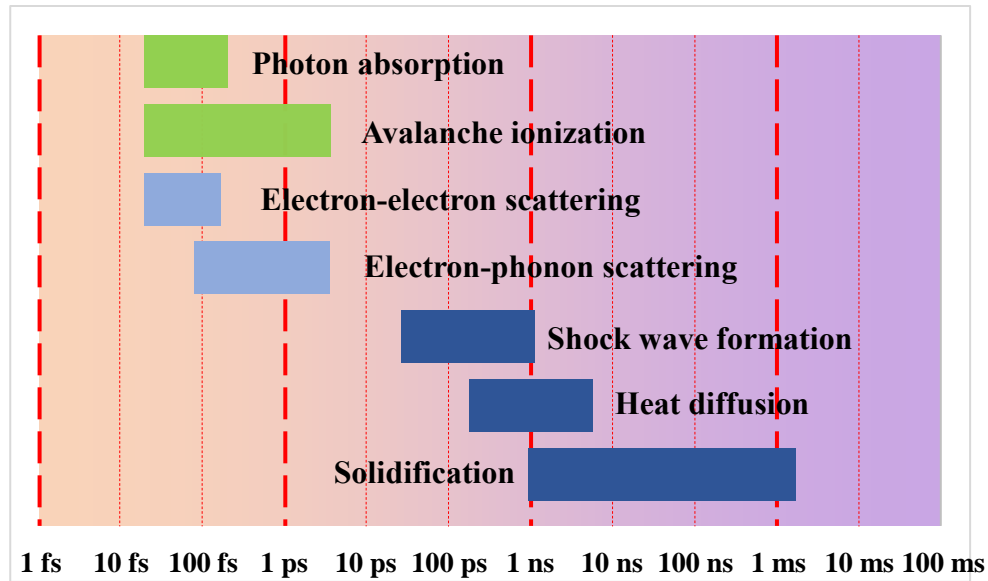


Figure 1 Schematic outlining the characteristic time scales of processes involved in ultra short pulse laser irradiation [24].

1.2.3 Non-linear processes in ultrashort pulses.

Due to extreme peak intensities achievable by ultrashort laser pulses, they can trigger non-linear absorption phenomena in materials with large bandgaps which are normally transparent at the respective wavelength [21]. Such phenomena include multiphoton ionization (MPI), tunneling ionization and avalanche ionization.

The tunneling ionization is observed for low (more than several times lower than the bandgap) energy photons if the energy fields of the laser pulses is sufficient to distort the Coulomb potential wells trapping valence electrons, causing tunneling through a narrowed potential barrier. If, however, the energy of several photons is higher than the bandgap, ionization can be achieved by the electron absorbing several photons at once

(multiphoton ionization). MPI is a strongly nonlinear process, with a rate provided by $P = \sigma_k I^k$, where K is the number of photons required and σ_k is the respective constant coefficient. The criterion for the occurrence of one such process or the other is provided by the Keldysh parameter γ .

$$\gamma = \frac{\omega}{e} \left(\frac{m c n \epsilon_0 E_g}{I} \right)^{\frac{1}{2}}$$

For Keldysh parameters higher than 1.5, MPI is to be expected, and for lower values of γ photopolarization should occur via tunneling. For γ values close to 1.5 an intermediate regime occurs in which electrons that absorb photons must then tunnel through the potential barrier.

Multi-photon absorption (MPA) is especially relevant in the context of nanofabrication in transparent materials, such as glasses [25] and polymers [26]. Due to the strong non-linearity of MPA, by adjusting the peak intensity of the pulse just above the threshold required for MPA, it is possible to affect only voxels with widths of ~100 nm within micron-scale beam spots, significantly surpassing the diffraction limit [26]. The material remains unaffected outside of those voxels; this allows not just for high resolution, but also for three-dimensional fabrication due to the possibility of focusing the pulses at any depth within the transparent material.

Polymers with large MPA cross-sections were developed; there exist both positive and negative photoresistive polymers that allow for resolution high resolution three-dimensional lithography that uses ultrashort laser pulses [26].

Another important mechanism for the ionization of transparent materials is the avalanche ionization. When due to tunneling, multiphoton or intermediate phenomena an electron crosses the bandgap, it becomes capable of increasing its energy by linear absorption. When this excess of energy (over the minimum of the conduction band energy) becomes higher than the energy required to cross the bandgap, the electron may relay that excess energy to an electron in the valence band, allowing it to also reach the conduction band. This may result in an exponential increase of the number of electrons in the conduction band [21].

It is possible that the avalanche ionization stops due to the end of the ultra short pulse. It is also possible that it increases the concentration of electrons to such a degree that the plasma frequency reaches the frequency of the incident laser. At this critical frequency, free electron absorption can happen in the plasma [21].

In sub-picosecond pulses, the first “seed” electrons of the avalanche can be reliably provided by photoionization processes, or photoionization may even be sufficient to cause damage in the material [27]. However, in longer pulses (several tens of picoseconds) avalanche ionization could occur without photoionization, instead being triggered by impurities, structural defects and thermal excitation. This strong dependence on random defects, impurities and thermally excited electrons makes the threshold for laser damage non-deterministic [27].

The determination of laser damage threshold in bulk materials is complicated by the self-focusing effect. Ultrashort pulses have high peak intensities, which enable

nonlinear processes, including non-linear refraction, described by the formula $n = n_0 + n_2 I$. Most materials possess a positive nonlinear refractive index n_2 . This means that in the central area, where the laser irradiation is most intense, the refractive index is increased, effectively creating a lens [21] and possibly resulting in the catastrophic collapse of the pulse [28].

1.2.4 Relaxation or ultrashort laser pulses

For pulses as short as 50 fs, a phenomenon known as Coulomb explosion may cause the destruction of the irradiated material even before the energy absorbed by the electrons is dissipated through electron-phonon scattering [29]. Following the fast electronic processes, the atoms of the lattice become ionized and positively charged to an extent that leads to the lattice being destroyed by repulsive forces [30]. This results in the expulsion of particles; those particles may be positive or neutral due to capture of electrons near the surface [29].

Besides the Coulomb explosion, ablation also takes place at larger timescales; in a metal, after the initial plume of ions ejected by Coulomb forces at ~ 500 fs, a later plume of neutral atoms may follow with a maximum ablation rate registered at 3 ps. These atoms are ejected due to intense local heating of the lattice occurring after electron-phonon relaxation. This creates a supersonic (for example, in Al, 2.59 km/s compared to the speed of sound of 1.48 km/s [31]) shockwave in the bulk of the material [32].

It is through electron-phonon scattering, which typically happens in times on the order of hundreds of ps [22] or ones of ps [33] that the electron temperature can achieve

equilibrium with the temperature of the lattice. That process is referred to as carrier cooling [34]. It is worth noting that since the phonons have small energies of the order of tens of meV (which corresponds to infrared frequencies), multiple acts of carrier-phonon scattering are required to cool down even one hot carrier [22]. In GaAs, the electron-lattice equilibrium is achieved in a few picoseconds for high frequency excitations [35]. The time of relaxation τ_a depends on the properties of phonons in the lattice:

$$\frac{1}{\tau_a} = \frac{\sqrt{2} E_1^2 m^{3/2} k_0 T (\mathcal{E} - \mathcal{E}_0)^{1/2}}{\pi \hbar^4 \rho u_1^2}$$

Here, E_1 is the deformation potential for the acoustic phonons [36], $\mathcal{E} - \mathcal{E}_0$ is the excess energy of the electron over the minimum of the valley, ρ the density of lattice and u_1 the velocity for longitudinal acoustic waves.

It could be compared to Si, another well-known semiconductor, in which electron thermalization and electron cooling were measured to be <150 fs and hundreds to thousands of picoseconds respectively, with the electron-phonon relaxation rate depending significantly on the density of excited carriers [37].

In metals, the time of electron thermalization is dependent on the density of states [38] and the Coulomb screening [39]. For example, Al exhibits electron thermalization as fast as 11 fs, while for Au and Ni it takes 47 and 86 fs respectively [38]. The subsequent electron cooling in Al occurs on the scale of ones of picoseconds depending on the electron-phonon coupling [40, 41], which in turn depends on the electron temperature [42].

An illustration of how the lattice properties affect the dynamics of ultrashort pulse relaxation is given in MoS₂, a layered material, that exhibits time scales of ~100 fs and 50 ps respectively for hot electron scattering (which includes scattering with electrons, phonons, defects and other elementary excitations) and carrier cooling in its bulk form. In a few-layer form MoS₂ features shorter times of <20 fs and ~300 fs respectively for those processes [34].

Despite thermal diffusion being slower than the absorption of ultrashort pulses, it has a significant influence on the ablation or melting threshold. For pulses longer than a critical pulse width, thermal diffusivity κ [cm²s⁻¹] defines the penetration depth l_{th} of the pulse (of duration τ):

$$l_{th} = 2\sqrt{\kappa\tau}$$

The critical pulse width (which differentiates “ultrashort” pulses from “long” pulses) varies in different materials. For example, in Al this critical pulse width was estimated to be ones of ps. For the shorter pulse duration of 100 fs (much shorter than critical pulse width), the ablation rate is several times higher compared to a longer pulse duration of 4.5 ps (comparable to pulse width): ~150 nm/pulse and 50 nm/pulse respectively for an energy fluence of 10 J/cm² [43]. The heat propagation is more significant from irradiation with higher energy fluences, which prompts to denote a “low fluence” and a “high fluence” regime with different dependences of ablation rate on energy fluence [43]. In the low fluence regime (below 1.5 J/cm² for Al) the penetration depth of the pulse can be well estimated as the optical penetration depth, and thermal effects are

insignificant for femtosecond pulses. For high fluence, the depth of penetration of the pulses becomes up to ~10-20 times higher and thermal effects are important even for pulses shorter than 1 ps [43]. For example, the ablation threshold for steel, Al and Cu were found to be 20, 110 and 190 mJ/cm² respectively for 100 fs irradiation. Melting thresholds also depend on the pulse duration, possibly differing by ~2 times in Si for 25 fs and 400 fs pulses (170 mJ/cm² and 280 mJ/cm²) [44].

1.2.5 Concluding remarks

Due to their numerous benefits, pulsed lasers found an extremely wide array of applications in industry and medicine [45]. Still, c.w. lasers are used instead to treat crack sensitive materials, such as some stainless steels, and in production lines with high feed rate, due to not being limited by a pulse repetition rate. In processes such as laser CVD, c.w. lasers are used to provide constant thermal output [46].

In this work, effects of femtosecond ablation by a pulsed laser and purely thermal effects easily achieved with c.w. lasers were investigated. Featured are multiple cases of using continuous wave lasers (UV oxidation of GaAs, laser synthesis of MoS₂ from precursor films with simultaneous periodic submicron patterning and UV densification of porous silicon) and one case of using a femtosecond pulse laser (forming conical microstructures on aluminum alloys).

1.3 State of the art in relevant fields

1.3.1 Laser-induced periodic surface structures (LIPSS)

The phenomenon of LIPSS was first observed almost six decades ago [47], but the term “LIPSS” was coined in 1982 [48]. In certain conditions, laser irradiation leads to the spontaneous formation of periodic features with periods comparable to the wavelength of the incident laser. This is a universal phenomenon of laser-matter interaction, observed on materials ranging from metals and inorganic insulators to polymers [8] and even 2D materials such as graphene [49] and other van der Waals materials [50, 51].

The multitude of observed LIPSS effects is generally divided in two categories. Low Spatial Frequency LIPSS (LSFL) usually have a period $\Lambda \approx \lambda > \lambda/2$, where λ is the wavelength of the inciting laser, while High Spatial Frequency LIPSS (HSFL) have lower periods of $\Lambda < \lambda/2$ [52]. This work features observations of LSFL, which are better explained by existing models. Such models include analytical models such as the “efficacy factor” theory proposed by Sipe and Siegman in 1983 [53], which was later expanded to include the Drude model [54] and reformulated for easier mathematical computation [55]. HSFL, on the other hand, are yet discussed without a wide consensus [56] and are outside of the scope of this work.

LSFL can be 1D periodic features (linear gratings) or 2D patterns with periods close to that of the laser wavelength. 2D LIPSS have been reported in the literature to be associated with pulsed irradiation with circular polarization [57, 58]. On the other hand, 1D features are associated with linearly polarized incident laser beams. Depending on how these features are oriented in regards to the polarization of the incident beam, they are

divided between “LSFL-I” or “normal” features, which are perpendicular to the direction of polarization, and “LSFL-II” or “anomalous” [8, 59], which are parallel to the polarization.

In this work LSFL-II patterns are featured, which have been observed on GaAs and on laser-synthesized thin films of MoS₂ and WS₂.

1.3.2 Existing theories on LIPSS formation

The LIPSS phenomenon was referred to as “scientific evergreen” [60, 61] due to the vast scope of the involved mechanisms and phenomena and its universal nature. One could divide existing efforts to explain the formation of LIPSS into two general groups: theories and numerical electromagnetic models that analyze the spatial modulation of energy conveyed to the material; and theories and numerical models that analyze how homogeneously absorbed laser energy could lead to self-organization into periodic structures [52]. In this work, the focus is on the former. This is because of the clear dependence of the obtained structure’s direction on the polarization of the incident laser beam, which was not satisfyingly accounted for in matter reorganization theories without involving considerations of electromagnetic nature.

Electromagnetic models applied to LIPSS can be divided between numerical methods such as finite difference time domain (FDTD) [62] and particle in cell (PIC) simulations [63] and those based on analytical mathematical derivations. FDTD simulations are based on solving Maxwell equations for geometrical boundary conditions

[64]. PIC simulations, on the other hand, focus on calculating how charged particles move under electromagnetic fields within fixed cells [65].

Analytical theories on the formation of LIPSS generally use the idea of a surface electromagnetic wave being excited on the interface between the material and the surrounding medium, such as vacuum, air or possibly water. It is common in the event of irradiating metals with a small number of ultrashort pulses that the period of induced LIPSS (which are observed to be directed parallel to incident polarization, LSFL-I) is well described by the period of the surface plasmon polaritons (SPPs). For the interface between the metal m and the dielectric d :

$$\Lambda_{LSFL} = \Lambda_{SPP} = \lambda \cdot \text{Re} \left(\sqrt{\frac{\epsilon_m + \epsilon_d}{\epsilon_m \epsilon_d}} \right)$$

It is worth noting that the dielectric permittivity ϵ of the material can change transiently within the duration of the pulses, according to the Drude model [66].

$$\tilde{\epsilon}_{excited} = \tilde{\epsilon}_0 + \Delta\tilde{\epsilon}_{Drude}$$

$$\tilde{\epsilon}_{Drude} = -e^2 N_e / (\epsilon_0 m_{opt}^* m_e \omega^2 [1 + \frac{i}{\omega \tau_D}])$$

Here, e and m_e represent the charge and mass of a free electron. N_e is the density of electrons in the conduction band. ω is the optical angular frequency and ϵ_0 is the vacuum dielectric permittivity. m_{opt}^* and τ_D are the optical effective mass and the Drude damping time [67].

Here, the coupling of free-space photon in to the SPP is made possible by the roughness that is produced by the first pulses or several pulses. The random roughness can be viewed as a spectrum of diffraction gratings; only the roughness features that act as a grating with the period Λ_{LSFL} will fit the law of momentum conservation for SPPs. In the subsequent pulses, positive feedback mechanisms will reinforce these features, usually through ablation [68].

This simple model does not explain the formation of LSFL-II. Additionally, it is not suitable to describe irradiation with a large number of pulses in which LIPSS of significant height are produced, since the requirement of $h \gg \lambda$, where h is the modulation of height of the treated surface, no longer holds.

A wider theory that allows to account for both LSFL-I and LSFL-II is the widely accepted and often cited theory [52] developed in the early 1980s by the group of van Driel and Sipe [69, 53] with contribution from the group of Fauchet and Siegman [70]. It will be referred to as “Sipe’s theory”.

Sipe’s theory addresses the excitation of surface electromagnetic waves (SEWs) in the interaction of the incident wave and a rough surface. In this view, LIPSS are due to the interference of the incident field and these SEWs, which modulates the amount of energy conveyed to the material. This theory operates with the Fourier space of wave vectors κ describing directions and periods of periodic structures on the surface for the sake of “avoiding the difficulties of the heuristic “surface-scattered wave” picture” [53]. By using

Maxwell equations and Green symbolism, this theory finds the absorption of incident light to be inhomogeneous in the $\mathbf{\kappa}$ space. Absorption is proportional to

$$I(\vec{\kappa}) \sim \eta(\vec{\kappa}) \cdot b(\vec{\kappa})$$

Here, $b(\mathbf{\kappa})$ measures the amplitude of random roughness of a certain wave vector and is a slowly varying function while $\eta(\mathbf{\kappa})$ is the efficacy factor showing how effectively the roughness of this wave vector contributes to inhomogeneous absorption. This $\eta(\mathbf{\kappa})$ exhibits sharp peaks in the $\mathbf{\kappa}$ space. Sipe's theory predicts that these sharp peaks of inhomogeneous absorption show at which $\mathbf{\kappa}$ LIPSS can be observed, which means their direction compared to the polarization of the incident field and their period. However, a peak of $\eta(\mathbf{\kappa})$ does not always guarantee that LIPSS with a particular $\mathbf{\kappa}$ will be observed; if, however, LIPSS will appear, they will correspond to one such $\eta(\mathbf{\kappa})$ peak.

For normal incidence, the predicted $\mathbf{\kappa}$ values should satisfy either $\mathbf{\kappa} \approx 2\pi/\lambda$ or $\mathbf{\kappa} \approx 2\pi \cdot n/\lambda$, which is in many cases in agreement with experimental results. Metals and dielectrics with large n usually follow the rule of $\mathbf{\kappa} \approx 2\pi/\lambda$, while materials with small n satisfy $2\pi \cdot n/\lambda$ [53].

In this model, the randomly rough surface is confined to a thin layer called the "selvedge region" with a thickness of l . Above the selvedge layer is vacuum, from which the field is incident, and below the selvedge layer is an infinite volume of bulk material. The material of the selvedge layer is considered to have the same susceptibility as the material of the bulk, though according to Sipe et al. it would be straightforward to consider a more general case in which it has a different susceptibility [53].

It is required that $l \ll \lambda$ (the thickness of the selvedge layer is much smaller than the wavelength of the laser), and that $\mathbf{k} \cdot l \ll 1$ (the thickness of the selvedge layer is much smaller than the period of the periodic structures obtained). The features of roughness are described by the “filling” and “shape” parameters F and s . The filling factor $0 < f < 1$ simply denotes the portion of the selvedge layer’s volume that is filled with the material (the rest is filled with void). The shape factor in some sense defines the aspect ratio of the roughness features in the selvedge: a “pancake” shape for $s \rightarrow \infty$ and a “spike” shape for $s \rightarrow 0$.

Typically, for polished surfaces [53] and deposited films of low (< 5 nm) roughness [71] those factors are taken to be $F=0.1$ (low roughness) and $s=0.4$ (spherically shaped islands). Indeed, LIPSS are observed on polished surfaces. Imprinting a periodic structure is possible even with a single pulse [72]; however, to observe well-defined LIPSS a multitude of pulses [61] or c.w. irradiation are required. Sipe’s theory arrives to the conclusion that while for p-polarized irradiation the factors F and s have an influence on $\eta(\mathbf{\kappa})$, for s-polarized light those factors do not affect $\eta(\mathbf{\kappa})$ and only influence the amplitude of $I(\mathbf{\kappa})$ [53]. It was, however, shown that a change in the filling factor can change the width of the $\eta(\mathbf{\kappa})$ sharp peak, causing a difference in the observed direction of LIPSS [71]. Overall, this roughness model is consistent with some experimental observations [71]. However, it has a significant drawback of not being able to account for the changes of the surface in the event of the material being irradiated with a large number of ultrashort pulses [52].

Sipe's theory uses the term "radiation remnants" to refer to non-radiative fields imposed by the scattering in the selvedge. Indeed, a plane wave may not propagate along the interface of two different materials, otherwise it would require a longitudinal component [53].

The interference leading to inhomogeneous absorption occurs not in the selvedge layer, but in the bulk, which experiences the selvedge layer as a dipole sheet with a dipole moment per unit area of $Q(\kappa)$, which creates an image polarization in the bulk. The far-field dipole-dipole interaction is what creates the periodic modulation in the bulk. This modulation is enhanced in the direction perpendicular to the polarization in metallic (or transiently metallic) materials with $\epsilon < 0$ or in the direction parallel to that polarization in non-metallic materials with $\epsilon > 0$. This is contrary to the simple SPP model, in which the propagation of SPPs would require $\epsilon < -1$ [73].

The mechanism that translates the incoupling of energy into a change of the surface topography is typically laser ablation [74], but in case of low peak laser intensities it could also involve localized melting combined with subsequent hydrodynamic re-deposition of the molten material [75]. Low intensity irradiation can also cause localized photo/thermo-chemical effects (e. g., oxidation) [76], which can also result in topography changes.

The formation of various types of LSFL can be showcased by modelling the effect of surface roughness features as dipole emitters (to describe the formation of the scattered

wave that interferes with the incident one) [59]. A numerical simulation of a single TiO_2 spherical defect on a Ti surface [59] illustrates this (Figure 2).

In the near-field, the scattered field may couple into surface plasmon-polariton (SPP) modes, even if the wavelength of the incident irradiation is not precisely corresponding to the SPP resonant wavelength. The SPP will propagate along the direction of polarization of the incident irradiation, creating a modulation of the electric field in that same direction. If this modulation would result in the formation of linear ripples, those would be perpendicular to the incident polarization. This falls under the category of the LSFL-I type, which is the most frequently observed, especially in the case of ablation of metal surfaces by ultrashort laser pulses.

In the far field, the electric field may not propagate along the surface, as in the case of SPPs, but it can interfere with the incident wave. As it originates from a dipole emitter, this field will be most intense in a direction that is perpendicular to the dipole axis and therefore perpendicular to the incident polarization. Therefore, the modulation with a vector perpendicular to the incident polarization will result in forming ripples parallel to incident polarization, LSFL-II.

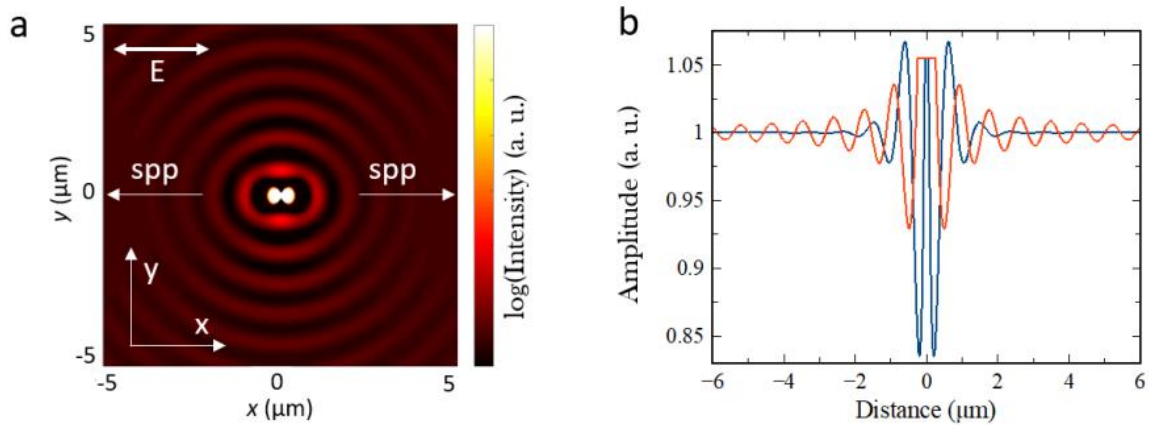


Figure 2 a) Interference of incident light with light scattered from single defect (modelled as an emitting dipole), b) cross sections of the intensity distribution from (a). Blue line is the cross section along x and the incident polarization, red line is the cross section along y and perpendicular to the incident polarization. Reproduced from [59].

These considerations are helpful to explain the physical origin responsible for the formation of various LIPSS types. Ablation of metals predominantly results in LSFL-I, rather than LSFL-II because, as can be seen from Figure 2, the modulation caused by the SPP prevails at short range. If this modulation exceeds the ablation threshold, LSFL-I will easily dominate and LSFL-II will not be induced. On the other hand, for dielectrics [77] or polymers [78] that do not support SPPs, or in the case of low intensity irradiation that cannot induce ablation, LSFL-II may emerge. Due to a lower depth of modulation (Figure 2), such features rely significantly on feedback from previously induced features and require a larger number ($\sim 10^3$) of laser pulses to develop.

In this work, we observed formation of LSFL-II on transitional metal dichalcogenides (TMDCs) during synthesis from insulating films of ammonium

tetrathiomolybdate ((NH₄)₂MoS₄) deposited on a layer of silica on silicon wafers and formation of LSFL-II on GaAs crystals. For these films, we believe the effect responsible for the periodic modification to be entirely thermal. However, it is novel in the sense that we demonstrate simultaneous periodic patterning of the (NH₄)₂MoS₄ film and synthesis of MoS₂ due to its thermal decomposition in a single step of processing. Previously, LIPSS patterning of films convertible to MoS₂ was demonstrated, but the conversion resulted in substantial loss of the patterning's quality [79].

On another note, we observed LSFL-II induced by photothermal and photoelectric oxidation of GaAs crystals. Oxidation of GaAs is a well-established [80, 81, 82] technological process used to create protective coatings and metal-oxide-semiconductor (MOS) devices. This work explored UV irradiation in a high intensity range leading to formation of deep oxide with large pores in GaAs layers through UV irradiation, as well as LIPSS-II caused by periodically preferential oxidation.

Another distinctive aspect of this work is the use of c.w. laser irradiation rather than short pulses. It is much simpler to obtain LIPSS by using pulsed irradiation, because short pulses can allow to significantly reduce thermal relaxation that would reduce the contrast of the structures. By using pulsed irradiation, it is easier to reach peak beam intensities that surpass energy thresholds needed to ablate, melt or oxidize the material (***1.2.4 Relaxation or ultrashort laser pulses***). Though most studies on the LIPSS effect feature structures formed by pulsed irradiation, it was known that c.w. irradiation is also capable of inducing LIPSS [83]. As the studied processes are entirely ((NH₄)₂MoS₄ decomposition) or partially (GaAs oxidation) thermal, c.w. laser irradiation was used.

1.3.3 Applications of LIPSS

The potential areas of application of the LIPSS effect are diverse, but the most promising applications can be divided into the following groups: tribological applications, optical applications, surface wetting control and biomedical and chemical applications [61].

Engineering applications of LIPSS exploit this effect to modify and control the roughness of technological surfaces, resulting in reduction of wear and friction [84], or in other effects such as fuel atomization [85].

Most notable optical applications of LIPSS, of which there are many, include generation of structural color [86], enhancement of efficiency for light-emitting filaments [87] and increasing the efficiency of light in-coupling of solar cells [88].

In surface wetting applications, LIPSS are suggested for creating superhydrophobic self-cleaning surfaces and directional liquid transfer achieved by controlling gradients of hydrophobicity [89].

Lastly, the biological and medical applications of LIPSS take advantage of the ability of surface microstructuring to either promote [90] or suppress [91] proliferation of cell cultures on various substrates.

1.3.4 Direct laser interference patterning (DLIP) compared to LIPSS

It is possible to draw a comparison between surface treatment performed through the use of the LIPSS phenomenon (which can be described as interference between

incident beam and a field scattered by the roughness of the surface) and surface treatments that use interference of laser beams.

Such a method is known as DLIP, and its execution requires a grating interferometer [92]. By adjusting the pulse energy, it is possible to achieve periodically selective ablation with periods potentially as small as $\lambda/2$.

DLIP techniques have several advantages over LIPSS: it allows to achieve modulation depths up to 2 μm [92], provides better regularity of gratings and allows for independent control of period and depth of modulation. However, LIPSS have different advantages: using HSFL allows to obtain periods of modulation as low as $\lambda/10$, and fs pulses could be used, while in DLIP only ps pulses retain sufficient coherency. Additionally, the setups required for DLIP are more complex, and global beam coherency is required. Both methods are promising for surface modification and potentially allow to process up to a meter of surface per minute [93].

Interference is also used in laser interference lithography (LIL), a well-established lithographic process that uses a photoresist layer rather than direct laser irradiation of the surface [12].

1.3.5 Conical microstructures

At high fluences, ablation may lead to the formation of conical microstructures on the surface of pure metals and alloys. This is attributed to the contribution of two mechanisms; i) preferential ablation and ii) re-deposition of nanoparticles stimulated by ablation [94]. Initially, random impurities or defects leads to the formation of small

(several microns in size) precursor cones at locations where the material is ablated to a lesser extent. Then, precursor cones grow due to the preferential ablation in the surrounding areas. This preferential ablation is caused by two factors. First, the sloped cone edges (forming an angle with the incident beam) have a larger area for the same energy fluence, and therefore ablate less. Second, some of the radiation is reflected from the sloped cone edges to the surrounding areas. This explains the growth of the precursor cones into larger (tens of microns) conical microstructures. In the case of the scanning ablation regime, multiple layers of nanoparticles redeposit when the laser beam is moved away, and then are re-melted when the beam returns [94]. Such structures grow both in height and in width, until two cones meet. Then the cones become linked and grow only upwards, while the furrows between them grow deeper downwards [95]. The change in the surface morphology was shown to have a significant effect on the surface wettability [96].

1.3.6 GaAs

GaAs is a technologically important semiconductor, which is widely used in the areas of photonics and electronics (light-emitting diodes (LEDs) [97], lasers [98]), power electronics [99], photovoltaics [100], THz radiation [101] and microwave electronics [102], to name a few. This is due to attractive properties such as high carrier mobility [103], and a wide direct band gap (1.64 eV, or 756 nm), which enables the fabrication of efficient light sources.

GaAs has a cubic sphalerite lattice unit with a 5.65 Å side. It melts at 1513 K [104].

The refractive index of GaAs at 244 nm was measured by two-channel polarization modulation ellipsometry to be $2.063 + i * 4.052$ [105], resulting in a reflectance of 68% at normal incidence. A similar precise measurement was not found for GaAs oxide obtained by UV oxidation. Anodically grown native oxide of GaAs [106] was used for comparison instead. According to this study, the oxide becomes completely opaque for wavelengths shorter than 220 nm. There does not appear to be a more detailed study of the GaAs oxide UV reflectance in the literature.

Additionally, it is known that GaAs exhibits a notable peak of anisotropy of reflectance at ~ 276 nm [107]. At 244 nm, the difference of reflectance $\Delta R/R$ may still reach 0.001.

The established industry standard for creating GaAs chip devices (for example, mobile phones [108]) is using techniques such as metal-organic chemical vapor deposition (MOCVD) and molecular beam epitaxy (MBE) [108]. Additionally, atomic layer deposition (ALD) may be used to create oxide gates for GaAs devices [109].

For logistical technological purposes such as surface preparation [110] and in applications that involve metal-oxide-semiconductor (MOS) devices [111] and memristors [112], it is important to be able to create oxide layers on GaAs in a controllable manner. Furthermore, Ga_2O_3 , obtained by thermal annealing of GaAs oxide [113], is an important material for catalysis applications [114], electroluminescent devices [115], sensing [116], power and high voltage devices [117], Schottky diodes, FETs and other devices [118]. To this end, techniques that involve thermal [80], plasma, chemical [119] and electrochemical [81] interactions have been developed. Anodic

electrochemical oxidation of GaAs allows to create oxide that are up to 500 nm thick [110]. This protective layer may be removed by HCl etching along with contaminants and shallow surface damage, providing a high quality crystalline surface [110].

Lasers are used in GaAs modification and structuring mainly in laser interference methods, allowing to deposit ordered arrays of quantum dots during under an arsenic flux [120] or to induce a pattern of nanoholes via using a positive UV photoresist [121]. Alternatively, LIPSS patterning was suggested for creating anti-reflective coatings on GaAs [122].

There has been evidence in the literature that exposure to UV radiation has the capacity to produce ultra-thin uniform and continuous oxide layers on the surface of this semiconductor [82]. Here, results that are associated with the interaction of GaAs surfaces with c.w. UV laser radiation at intensities which are several orders of magnitude higher than previous reports [82] but still below the melting threshold are presented. It is shown that under these conditions of irradiation a well defined layer of nanoporous oxide is formed with a thickness of up to several hundreds of nanometers.

Furthermore, self-organized periodic patterning of the oxide layer, which depends on the intensity and polarization of the irradiating laser beam, is observed. This spontaneously formed periodic patterning matches the description for LSFL-II [60]. While LSFL-I induced by ultrafast pulse laser ablation on GaAs were well covered in the literature, the LSFL-II induced by periodically preferential oxidation are a relatively recent observation. It is demonstrated how such structures were induced on GaAs with c.w. UV irradiation.

1.3.7 AA2024-T4 (D16T)

The present work focuses on the ultrafast laser processing of D16T alloy. This Russian designation describes an alloy that is fully equivalent to the alloy AA2024-T4 according to the International Alloy Designation system. This type of artificially aged Al-Cu alloy is used in aviation because of its attractive mechanical properties (e.g., strength-to-weight ratio) and resistance to mechanical damage. The present work focuses on the ultrafast laser processing of D16T alloy. This Russian designation describes an alloy that is fully equivalent to the alloy AA2024-T4 according to the International Alloy Designation system. This type of artificially aged Al-Cu alloy is used in aviation because of its attractive mechanical properties (e.g., strength-to-weight ratio) and resistance to mechanical damage.

Femtosecond laser treatment was shown to increase nanohardness of aluminum and its alloys both under vacuum and in ambient conditions. When processing in ambient conditions, the presence of oxygen leads to the formation of oxide phases. The concentration of oxygen may reach 16% [123].

A detailed coverage of conical microstructure growth on aluminum and other metals at 800 nm 130 fs laser pulses is provided by Nayak [124]. A focused ion beam (FIB) cutting of a conical structure grown on titanium is provided, but no internal structural change was reported. One can conclude that the complex character of laser-matter interaction over a wide range of energy fluences causes versatile topological surface modification for commonly used engineering alloys and offers a promising dedicated procedure for advanced surface enhancement.

Hill-like microstructures along with maze-like microstructures were observed on various laser-irradiated metal surfaces [125]. The differences in the surface structures, which were observed on different metals, were explained by differences in the strength of electron-phonon coupling and the thermal conductivities. Another work providing significant insight into the properties of microstructures grown on D16T via femtosecond ablation examines the effect of laser energy fluence and number of passes on the roughness and reflectivity of ablated areas [126]. Finally, it is worth mentioning the work revealing the contents of an onion-like aggregated nanoparticle sphere on D16T via focused ion beam milling [127]. This highlights the importance of rigorous characterization of surface structures using modern techniques such as focused ion beam (FIB) milling and lamella cutting.

For the aluminum alloys in particular, there is interest in studying the corrosion mechanism to improve resistance to corrosion, including the use of laser-based methods such as laser surface melting (LSM). The introduced elemental inhomogeneity of the alloy's surface has an effect on its corrosive properties, which may be positive or negative (for AA2014-T6, LSM was shown to cause significant reduction of pitting potential, while for AA2024-T351 the treatment caused less significant increase of the pitting potential) [128]. This emphasizes the relevance of an in-depth FIB-SEM investigation of the conical microstructures obtained through ablation.

1.3.8 2D-TMDCs

Two-dimensional materials are ultrathin crystalline layers that bond to each other by van der Waals forces and therefore single layers have been isolated, starting from the

Nobel prize-yielding work on graphene [129], which is a monolayer of graphite. Among 2D materials there exists a subclass of semiconducting layered crystals called transition metal dichalcogenides (TMDCs) [130]. These materials have attracted much interest lately due to a plethora of interesting physical properties, spanning from optical nonlinearity [131] and magnetism [132] to superconductivity [133], to name a few. Some of those properties stem from their compositional tuneability. By changing the combinations of transition metals and chalcogens, doping or alloying, it is possible to tailor their electrical and optical properties to match various applications. Additionally, properties of TMDCs such as MoS₂ and WS₂ depend strongly on the thickness of few-layer films, for example, both MoS₂ and WS₂ exhibit an increase in bandgap width and a transition from indirect to direct bandgap [134, 135].

Consequently, much research has been conducted in recent years on various aspects of the synthesis and utility of these compounds to investigate the length and breadth of their capability to be implemented in cutting edge technological applications such as optoelectronics, sensing, and quantum information [136].

It has been reported that nano-structuring of 2D-TMDCs has the potential to improve the performance of these materials in applications such as switching and sensing [137]. For instance, Daus et al. demonstrated a flexible monolayer MoS₂ FET with a channel length of 60 nm, which possesses ultra-high on-current ($\sim 500 \mu\text{A}$) at a very low gate voltage (1 V) [138]. Furthermore, a superior photosensitivity ($2.67 \times 10^6 \text{ A/W}$ at $\lambda = 520 \text{ nm}$) has been demonstrated by applying nanobridge technology to fabricate multi-nanoheterojunctions MoS₂ phototransistors [139].

A significant consequence of such submicron patterning is the ability to create a variety of defects associated with crystal edges. A type of defect very frequently observed in TMDCs is the chalcogen vacancy [140]. While chalcogen vacancies are sometimes observed on continuous surfaces of TMDC films, an alternative way to obtain large numbers of such chalcogen vacancies could be to create nanostructured TMDC films that feature a lot of edge length per surface area. The sulfur-terminated edges of the TMDC atomic layers are known to exhibit more sulfur vacancies [141].

Such a vacancy is a defect from the crystallographic point of view; however, its effect on the photoelectrical properties can be beneficial. Chalcogen vacancies introduce energy states inside the bandgap and act as shallow traps for free carriers. The difference between shallow and deep traps in the bandgap is how far they are from the valence or the conduction band and what is the likely outcome of a carrier being trapped in one. Carriers in a deep trap are far away from the conduction and valence bands, and the most likely outcome for them is recombination with a carrier of the opposite sign, which results in them no longer participating in the photocurrent. On the other hand, shallow traps are close to either the valence or the conduction band. A charge carrier in a shallow trap is likely to be thermally re-excited and become a free carrier thus contributing to the photocurrent. Effectively, the carrier in a shallow trap is put on pause, neither participating in photocurrent nor exiting it. As a result, the presence of shallow traps in the material's bandgap will increase the lifetime of photogenerated carriers, as they are less likely to recombine [142]. Therefore, an increase of the photocurrent will occur at the cost of increasing the response time.

The shallow traps' effect on photoconductivity and phototransistor performance is twofold: while they reduce the response time of photosensitive devices significantly, the photocurrent grows in magnitude. In this way, defect engineering allows multilayer TMDCs to achieve remarkably high photoresponsivities [143].

While high response times are not desirable for every application (in typical and wide-spread building monitoring photodiodes may be preferred over photoresistors [144]), there is interest in materials that exhibit “persistent photoconductivity” (PPC) [145, 142, 146, 147]. Elements that retain photocurrent over a prolonged time allows to avoid reacting to fluctuations, and there is a growing interest [148] in applications of PPC in optical memory [149], charge storage [150], solar cells [151] and simulation of neurotypical devices [152].

1.3.9 Synthesis methods for 2D-TMDCs

A significant variety of methods of obtaining few-layer or monolayer TMDC films was proposed; these different methods can be generally divided in the categories of top-down and bottom-up approaches. In the first case, few-layer or monolayer TMDC structures are created by separating bulk TMDC, while in the second case few-layer or monolayer TMDS are obtained from composing atoms.

The most known top-down processes for TMDCs are mechanical exfoliation, micromechanical exfoliation [153] and liquid solvent exfoliation [154]. Mechanical exfoliation is a very simple technique that requires only scotch tape and the bulk materials [155], but it allows to obtain high quality TMDC flakes as thin as a monolayer;

however, this process is not scalable and does not provide good control over the size and shape of obtained flakes.

Bottom-up processes include: chemical vapor deposition [156], atomic layer deposition [157], metal-organic chemical vapor deposition [158], molecular beam epitaxy [159] and others.

One particularly promising route for industrially viable synthesis of TMDCs is the solution-based synthesis that produces TMDCs by decomposing a single source precursor [160]. A variety of ways to coat the surface with a precursor film for subsequent MoS₂ synthesis was demonstrated [161, 162, 163]. Despite challenges with solubility of (NH₄)₂MoS₄ in common solvents, this approach was successfully demonstrated for WS₂ as well [164]. This method, however, requires addressing challenges on low wettability of precursor solutions on common substrates.

Recently, it was demonstrated that it is possible to employ a laser-based method to synthesize in situ MoS₂, WS₂ or their alloys (Mo_xW_{1-x}S₂) [11, 165], which are among the most extensively studied TMDCs [165]. The local nature of the laser synthesis process leads to readily micro-structured films, which provides another level of convenience and ease to this synthesis method. This simplifies the fabrication of electronic or photonic devices. Indeed, the films are synthesized within laser-irradiated tracks that have widths comparable to the width of the focused laser beam used.

This method relies on localized thermal decomposition of single-source precursors ((NH₄)₂MoS₄, (NH₄)₂WS₄) [161, 164] induced by focusing a laser beam on the precursor film.

Interestingly, laser synthesis of TMDCs occurs in ambient conditions and with a minimum thermal load on the substrate, making it suitable for additive manufacturing. Working in ambient conditions does not allow to entirely exclude oxidation of the synthesized films; however, the degree of oxidation is comparable to other methods [11, 166, 167, 168] and does not negate the properties of the synthesized TMDCs.

The details of this method are provided below; however, this work is focused on the particular aspect of the synthesis, which is the ability to induce a submicron periodic structuring along with synthesis in a single processing step.

The existing literature contains reports of patterning films of metal-organic patterning with LSFL features by pulsed irradiation [169], and inducing HSFL features on exfoliated [170] TMDC layers or during CVD synthesis [51] of TMDCs. Additionally, nanoscale patterning of MoS₂ could be achieved with block copolymer lithography [143] or ultra-high resolution e-beam lithography.

However, this work presents a very simple approach to achieve submicron patterning of MoS₂ simultaneously with its synthesis from precursor film through the exploitation of the LIPSS phenomenon (*1.3.1 Laser-induced periodic surface structures (LIPSS)*) as a sub-micron structuring tool for TMDC defect engineering [143]. Here, the periodically preferential incoupling of the laser beam's energy causes both thermal decomposition of the precursor film (leading to MoS₂ synthesis) and laser thinning of already synthesized MoS₂ layers in a manner that reflects the intensity modulation, thus forming regular TMDC nanostructures. We also demonstrate the significant effect of this structural modification on the obtained semiconductor film's photoconductivity. While

highly regular and controllable LSFL patterning was demonstrated on metal-organic precursors [79], the conversion towards MoS₂ lead the definition and regularity of the patterns to deteriorate; here, the patterning is conserved on the films despite successful conversion to MoS₂.

The use of well-established and available precursor compounds and ambient condition synthesis could make this approach suitable for scalable production or rapid prototyping of nanostructured 2D-TMDCs.

1.3.10 Porous Silicon

Porous silicon is a material used in sensing and integrated optics [171, 172]. To obtain porous silicon, single crystal silicon wafers are immersed in an HF-containing solution and are subjected to anodic current [173, 174]. Porous Si predominantly maintains the superior crystal order of the single crystal, but has diverse properties from normal crystalline Si due to high surface area per volume. Layers of porous silicon are produced on standard single crystal silicon wafers by an electrochemically driven etching process [173]. Narrow, deep pores are formed, which extend from the surface of the porous layer to the interface between porous layer and bulk substrate.

The speed and spatial direction of the reaction with HF depends on the crystal face that is presented on the Si wafer. For the (100) orientation of a p-doped Si crystal, that type of etching process forms porous layers with narrow, deep pores connecting the surface of the porous layer and the interface between porous layer and bulk substrate [173]. This could be envisioned as the PorSi/bulk Si interface propagating deeper inside the material.

The porosity of the PorSi layer depends on the value of the anodic current [175] and may vary within a range of 30%-82% [174]. The porosity does affect the refractive index in a fashion that can be approximated by a linear function [176].

It is possible to etch distinct layers with varying porosities by modifying the anodic current during etching. In particular, it is possible to separate the bulk Si crystal and an optically denser layer of lower porosity with an optically rarer layer with higher porosity, creating a planar waveguide for visible and infrared ranges [177, 178].

However, for a large variety of applications, in-plane confinement is required to produce to define channel waveguides.

PorSi waveguides are widely applied in optical interference devices (e.g. tuned photodetectors [178]), particularly chemical sensing and biosensing [179, 180]. Volume scattering losses in PorSi depend, naturally, on the propagating wavelength, but also on the size of the pores, possibly being as low as $10^{-3} - 10^{-2}$ dB/cm for pores with a low (10-20 nm) diameter [181].

Several methods of creating PorSi channel waveguides are known, such as lithography and localized laser oxidation [182, 183].

In this work, however, an alternative possibility of defining channel waveguides in PorSi through laser densification of PorSi was studied. Laser annealing is shown to lead to formation of internal cavities and material rearrangement in uniform layers of PorSi, with some effects more pronounced under faster scanning rather than under slower scanning. Potentially, a very simple single-step method of directly writing PorSi channel waveguides

can be developed, showing promise for cheap mass production or rapid prototyping in lab environment.

1.4 Methodology

To facilitate the fulfilment of the objectives associated with this thesis, it was necessary to employ a laser writing setup and a variety of materials characterization techniques to investigate/characterize a wide range of laser-modified materials. More specifically, it was necessary to investigate surface structures on bulk materials, thin films on substrates and laser-modified volumes inside porous layers.

Optical microscopy and Scanning Electron Microscopy (SEM) were used for imaging and study of surface morphology.

To study surface profiles, stylus profilometry and Atomic Force Microscopy (AFM) were mainly used for features such as c.w. laser-irradiated tracks. However, in the case of conical microstructures on aluminum alloy surface sharp drops of height up to tens of microns were present, which required a different method. For this sample, confocal optical profilometry was used instead.

For some of the studied samples, determining the elemental composition was important. Energy Dispersion X-ray spectroscopy (EDX) was used in tandem with SEM imaging to obtain such information locally when studying the laser irradiation of GaAs and the D16T aluminum alloy. In the case of GaAs UV oxidation, more precise quantitative information about elemental composition was obtained by using X-ray Photoelectron Spectroscopy (XPS). For studying layers of porous silicon (PorSi), time of flight secondary

ion mass spectroscopy (ToF-SIMS) was used to track the distribution of oxygen in the volume. Alternatively, in our studies of thin films of MoS₂ Raman spectroscopy was better suited to confirm the presence of TMDC materials. When internal elemental composition was studied, these methods were supported by ion beam milling.

1.4.1 Laser writing setup

Laser irradiation experiments were performed using a custom laser writing system (Figure 3), which utilizes a high precision 2D translation stage (AEROTECH Nanopositioner ANT95-XY) that was used to scan the sample in front of the focused laser beam. A scanning speed of up to 20 mm/s could be reached.

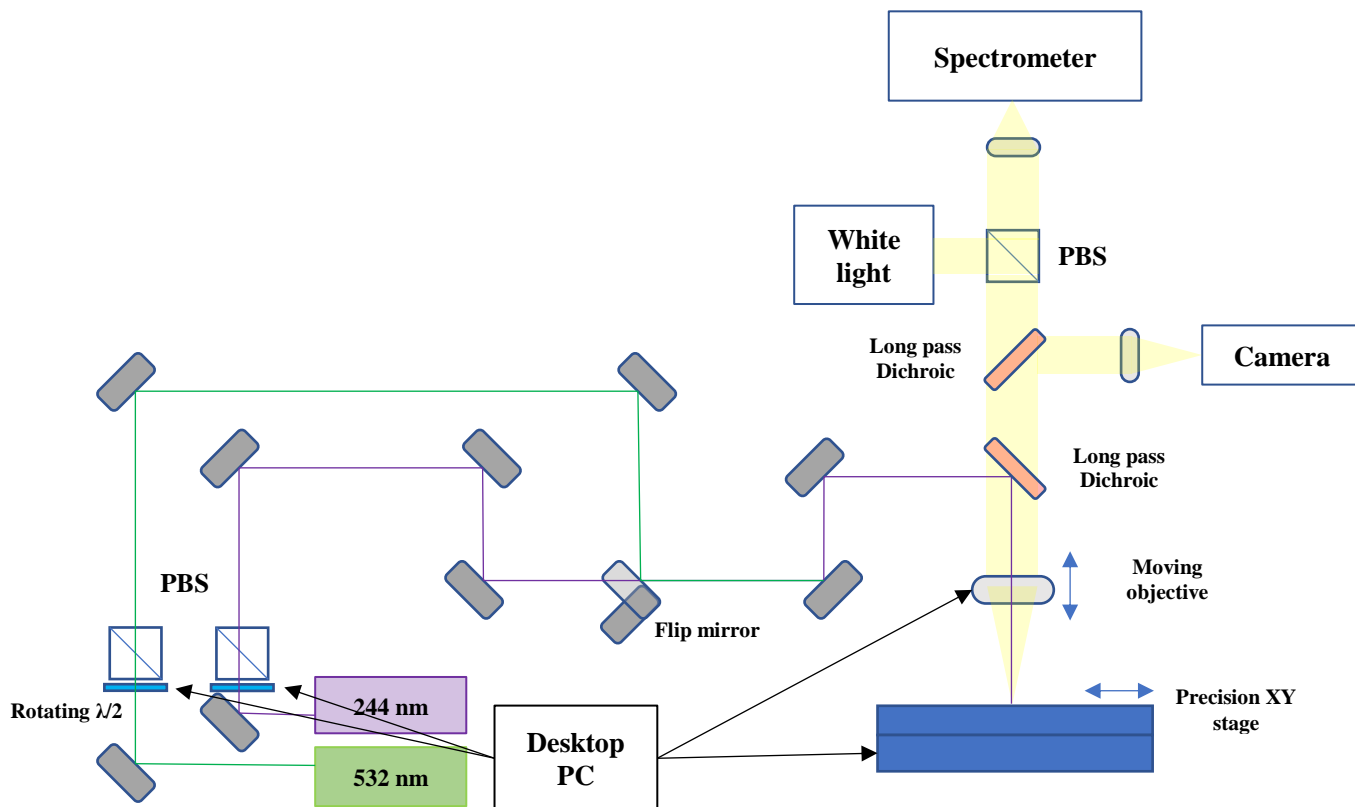


Figure 3 Schematic of laser writing setup.

Throughout laser scanning protocols, the beam power could be varied by rotating a programmable $\lambda/2$ plate, therefore rotating the polarization of the laser beam incident on a polarizing beam splitter (PBS) cube.

The sample was tightly fixated on the scanning stage by a vacuum pump.

A frequency-doubled Argon Ion laser Coherent Innova FreD ($\lambda=244$ nm) was used as the UV laser source ($\lambda=244$ nm). For UV irradiation, the laser spot size at focus was 6.0 μm , obtained using a spherical lens with a 35 mm focal length. A continuous wave (c.w.) 532 nm laser system, Coherent-Verdi G20, was used to irradiate the precursor films. The laser beam was focused to a spot with a diameter of ~ 11 μm , using a microscope objective ($\times 4$). The LBP2-HR-VIS2 Beam Profiler (Newport) was used to measure the beam spot size.

By using dichroic long pass mirrors, it was possible to receive live camera feed and collect IR spectra during laser operation.

1.4.2 Laser synthesis of MoS₂ films

The laser synthesis of MoS₂ consists of performing three steps in the following manner.

Step one: a solution of the precursor in a system of organic solvents is spin-coated onto SiO₂/Si substrates and then allowed to dry at a temperature of ~ 90 °C for 5 min.

Step two: the dried precursor film is irradiated locally using a focused laser beam in the visible wavelength range (here we used a c.w. laser emitting at $\lambda = 532$ nm, as it is sufficiently well absorbed by the precursor film while allowing for convenient operation at high beam powers), which results in the synthesis of MoS₂ tracks.

Step three: the laser-irradiated sample is “developed” by immersion in organic solvents, which remove the unexposed precursor, revealing only the synthesized TMDC tracks.

Wafers of n-type single crystal silicon with a 300 nm oxide layer were diced into 1.5 cm² squares that were used as substrates for the deposition of TMDC films. The substrates underwent cleaning by ultrasonication in acetone, isopropanol, and then deionized water in this order. After the deionized water cleaning step, followed by drying under nitrogen flow, they underwent plasma etching in a mixed argon and nitrogen atmosphere for 15 min to remove any traces of organic contaminants and to produce a hydrophilic surface that improves the coverage during the spin coating step.

The concentrations of the ammonium tetrathiomolybdate ((NH₄)₂MoS₄) precursor solutions that were used here were: 24, 32, 40, and 48 mM. The system of organic solvents that was used to dissolve (NH₄)₂MoS₄ consists of dimethylformamide (DMF), butylamine, and ethanolamine (at volumes of 2, 2, and 1 mL, respectively). That particular formula of liquid precursor solution was optimized in previous works [162] as one that allows for uniform spin-coating of precursor films. The precursor solution was sonicated for 40 min. The resulting precursor solution was spin-coated on the substrates. The top speed of spin coating was 3500 rpm with a ramp speed of 500 rpm/s. The total duration of the spin coating was 1 min. After spin coating, the film was dried on a hot plate for 5 min at a 90 °C to remove the organic compounds.

The concentration of the liquid precursor solution directly affects the thickness of the precursor films obtained after drying the spin-coated solution on a hot plate. Due to

the low concentration of the precursor compound, a variation of concentration from 0 to 48 mM does not affect the viscosity of the overall solution significantly. The film is spin-coated to thickness that depends primarily on the viscosity of the solution and to a lesser extent on the parameters on rotation speed during spin-coating [162, 164]. During the subsequent drying step, the liquid organic solvents evaporate, leaving behind a thin solid film of the $(\text{NH}_4)_2\text{MoS}_4$ precursor compound, the thickness of which is defined by $(\text{NH}_4)_2\text{MoS}_4$'s concentration in the liquid solution.

The precise measurement of the thickness of the thin films of $(\text{NH}_4)_2\text{MoS}_4$ that cover large areas is relatively challenging. The solution concentration is chosen as a characteristic parameter instead, as it is clearly observable.

Following laser irradiation, the samples were immersed in n-methylpyrrolidone (NMP). This solvent removes the areas of the precursor film that were not irradiated without affecting the synthesized MoS_2 – this process is called “developing” the film, in a photolithographic sense.

1.4.3 Bright Field and Dark Field Optical Microscopy

Bright Field (BF) Optical Microscopy is a conventional technique, in which the sample is illuminated by a source of light, and the entire reflected signal is collected. On the other hand, Dark Field (DF) Optical Microscopy entails blocking off the specular part of the reflected light, therefore only collecting reflected light that underwent scattering. In that sense, DF mode tends to highlight strongly scattering features. In many cases, such features are simply particles of dust and other impurities. While in many cases BF

imaging was preferable, in this work DF imaging was indispensable, as it allowed spotting the strongly scattering LIPSS features with only a moderate 20X magnification. Figure 4 shows how DF imaging highlights LIPSS in the middle of a laser-irradiated track and an impurity in the top left corner of the image.

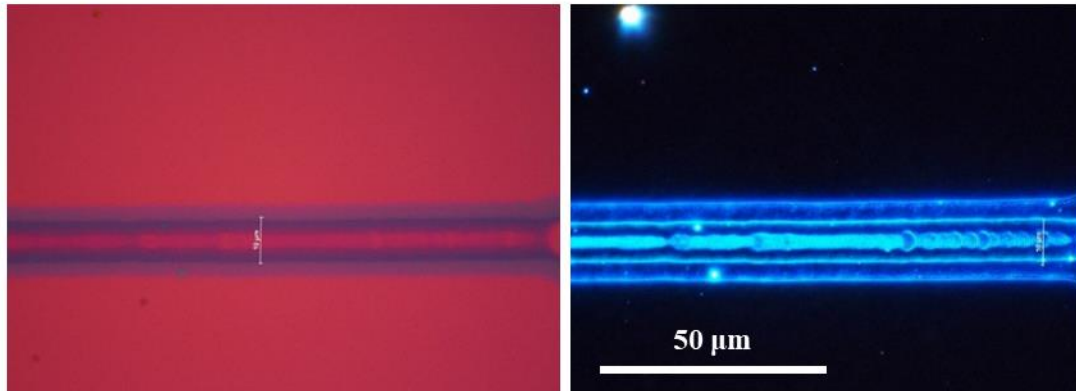


Figure 4 A laser-irradiated track containing LIPSS features in bright field and dark field modes of imaging.

1.4.4 Scanning Electron Microscopy (SEM)

SEM imaging was used extensively in this work for the observation of morphological features. Conventional optical microscopy has a diffraction limit comparable with the wavelength range of visible light, and therefore tends to have a small depth of focus of the order of a few microns. SEM microscopy allows surpassing such limitations, since the de Broglie wavelength of electrons, which are accelerated to tens of kilovolts, is only a few nanometers. The narrow e-beam allows to obtain depths of focus up to ~ 0.8 mm. However, the mechanisms responsible for obtaining image contrast

are different in optical and SE microscopy, and a vacuum chamber is required in the latter case.

The main physical principle behind SEM is scanning the sample with a focused beam of electrons. As scanning progresses, for each position of the beam of primary electrons, detectors collect a signal corresponding to the current position of the electron beam. That allows building an image that consists of pixels, each corresponding to a certain position of the primary beam. The slower the scanning, the more signal is collected. The magnification is changed by modifying the size of the area that is scanned. The resolution is determined by the electron beam spot size, which in turn depends on factors such as the acceleration voltage and the beam current. Higher acceleration voltages reduce the beam spot size and increase its penetration, while higher beam currents increase the beam spot size and the amount of signal collected. Usually an optimal trade-off between depth of analysis, resolution and contrast has to be found.

Where conventional optical microscopy relies on refraction of light to focus the beam, in SEM the focusing is achieved by a column of electromagnetic elements such as coils and capacitors. Scanning with a high resolution can, as well, be achieved by using these elements to shift the direction of the beam. The electron beam itself is emitted by cathodes or Shottky diodes.

While the interaction between the electron beam and matter may produce various types of signals, SEM focuses on registering secondary electrons (SE) and back-scattered electrons (BSE) through p-n junction or scintillator screen-based detectors. Back-scattered electrons are produced in elastic interactions between primary electrons (those

incident on the sample from the original electron beam) and atoms of the sample, while secondary electrons are produced by inelastic interactions.

Both types of signal collection, SE and BSE, are sensitive to the atomic weight (Z) of the analyzed sample and to the topography of the sample to some extent. However, BSE is primarily used to obtain contrast based on the atomic weight (Z -contrast) and SE is more suitable for collecting topography information. This is due to the different depth at which information is collected. Secondary electrons have lower energies compared to back-scattered electrons and can only escape from depths of a few nm, providing good sensitivity and contrast for examining thin layers and features on the very surface without overwhelming the signal by collecting information from deeper regions. Back-scattered electrons, however, collect information from deeper areas from tens of nm to hundreds of nm as well (~ 10 - 100 nm), which allows to retrieve crystallographic information and is beneficial for Z -contrast of thick layers or bulk samples. Conventionally, detectors of BSE signal are located close to the electron beam, while SE detectors collect electrons at large angles and are located further away from the electron beam (though SE detectors located close to the beam exist as well).

In this work, the features that have been studied had such thickness that SE imaging was mainly used with lower (typically 5kV) accelerating voltages and beam currents. This has occasionally caused carbon contamination [184]. When working with laser-synthesized TMDC materials (or their precursor films), which have been deposited on insulating layers of silica, accumulation of charge under the electron beam causes distortion of the image due to electrostatic deflection of the e-beam by the space charge.

To mitigate it, we occasionally used low vacuum mode of operation or applied bridges of conductive tape in the vicinity of the interest area.

Devices such as Tescan VEGA 3 LMU (Tescan, Brno, Czech Republic), Thermo Scientific Quattro ESEM (ThermoFischer, Waltham, MA, USA), Thermo Scientific Helios G4 PFIB-SEM UXe DualBeam (ThermoFischer, Waltham, MA, USA) and Tescan Solaris dual-beam scanning electron microscope (Tescan, Brno, Czech Republic) were used to perform SEM imaging.

1.4.5 Energy Dispersion X-Ray Spectroscopy (EDX)

EDX is a method of elemental analysis, again utilizing the interaction of a focused electron beam with matter. As in secondary electrons SEM imaging, it involves inelastic interactions of primary electrons with atoms of the sample. However, instead of secondary electrons, which can only escape from depths of several nm, x-ray photons emitted during relaxation of excited electrons are collected. X-rays can escape from deeper layers of the sample, which allows to collect information from deeper layers at depths of the order of several μm . The energies of the collected x-ray photons depend on the energy levels which are specific to atoms, and therefore various elements can be identified. EDX is highly sensitive to heavier atoms and struggles with light elements that have atomic weights below $Z=11$ [185].

It can be challenging to obtain quantitative EDX data for samples that are inhomogeneous within the analyzed volume of several cube microns. In this work, we did not use EDX for analysis of thin TMDC films, which were too thin. Instead, we utilized

EDX investigations on qualitative observations of FIB cross sections of layered and/or porous materials.

One way to improve the otherwise limited spatial resolution of EDX spectroscopy is to extract thin (~ 100 nm) lamellae from the sample. This procedure may be performed inside dual beam setups using a focused ion beam (FIB). The cutting out of a lamella forcefully confines the area of interest to a thin (~ 100 nm) layer by removing excess material. We used this for the investigation of the internal contents of conical microstructures of aluminum alloy.

The composition of the laser-modified areas was investigated by EDX using the Octave Elite Super module installed in the FIB-SEM system, Helios G4 PFIB-SEM UXe DualBeam (ThermoFischer, Waltham, MA, USA).

1.4.6 Focused Ion Beam (FIB, FIB-SEM) imaging and etching for cross section and lamellae preparation

The use of ion beam in FIB setups is in many ways similar to the use of electrons in SEM setups. Just as the electron beam, the ion (Ga^+ or Xe^+) beam can be focused by a column of electromagnetic elements and shifted for fine resolution scanning. Mainly, the task of the ion beam is localized ion bombardment of the sample, which results in localized material removal. This is predominantly used for either preparing cross sections of the sample, or to prepare thin lamellae for use with transmission electron microscopy (TEM) or Energy Dispersion X-Ray spectroscopy (EDX). As with SEM, this technique allows to obtain an image of the sample by collecting electrons that are expelled from the

substrate under ion beam scanning, but the quality of such imaging is usually inferior to SEM. However, FIB imaging is useful to support FIB cross sections.

High roughness of the sample's initial surface may lead to vertical wrinkles on the vertical surface obtained by ion milling. Additionally, the edge between the horizontal surface of the sample and the newly-produced vertical surface may be too round and smooth. To prevent these undesirable effects, FIB milling is in some cases preceded by the local deposition of a protective layer. In particular, Pt layers with thicknesses of $\sim 1-2$ μm are often produced for that purpose. A metal-organic gaseous compound is released in the immediate vicinity of the surface of the sample, and a low voltage FIB causes the decomposition of that compound, which allows to deposit a smooth layer of Pt on top of the sample.

In this work, all FIB setups used, namely Thermo Scientific Helios G4 PFIB-SEM UXe DualBeam (ThermoFischer, Waltham, MA, USA) and Tescan Solaris dual-beam scanning electron microscope (Tescan, Brno, Czech Republic), were FIB-SEM dual beam systems. In such systems, both an electron cannon and an ion cannon are present in the vacuum chamber, arranged at diverse angles of incidence (e.g., for Solaris the angle between the Xe^- ion beam and electron beam is 55 degrees). This allows to use the ion beam and the electron beam in tandem to observe the area of interest under different angles, or to obtain SEM images while etching the sample with the ion beam.

Using FIB, we produced cross sections for GaAs samples to verify the uniformity of the porous oxide layer and measure its thickness. Additionally, FIB milling was used to reveal the internal structure and composition of conical microstructures self-organized

through femtosecond pulse ablation on aluminum alloy. Finally, FIB cross-section were used to observe laser-induced changes in porous silicon.

1.4.7 Time of flight secondary ion mass spectroscopy (ToF-SIMS)

ToF-SIMS is a method of chemical analysis that uses an incident focused beam of ions to bombard the surface of the sample [186]. After a cascade of collisions caused by the primary ion, species such as electrons, single neutral atoms, single atom ions, molecular ions and neutral and ionized atom clusters are ejected. Using a time of flight detector, it is possible to measure the mass-to-charge ratio (m/z) of the secondary ions, which can be correlated to the element or elements that this ion consists of. Usually those secondary ions have charge of $z = 1$, be it positive or negative.

Ion bombardment makes ToF-SIMS an inherently a destructive analysis method, but it can be adjusted to cause minimal damage while still achieving the sputtering of some secondary ions. When used in this manner, most of the signal will be collected from the atomic layers on the very surface of the sample, as they are the easiest to eject. This provides high surface to the method. Alternatively, it is possible to induce significant ion etching of the sample, which would allow to gradually remove the surface of the sample layer by layer, acquiring a depth profile of signal or each mass to charge ratio.

This method is used for structural analysis of both organic [186] and inorganic [187] samples. The ability to construct a high resolution map of chemical content for the area of interest is a great advantage of the ToF-SIMS method. However, to use it for

quantitative comparisons is highly challenging due to both the ion sputtering yields and ionization efficiency being highly dependent on the local environment.

In this work, ToF-SIMS was used for depth profiling of laser-irradiated porous silicon (PorSi). Due to the high local inhomogeneity of the object of interest, the information extracted was qualitative. The Tescan Solaris dual-beam scanning electron microscope (Tescan, Brno, Czech Republic) system was used.

1.4.8 X-ray Photoelectron Spectroscopy (XPS)

X-ray Photoelectron Spectroscopy can be in some way seen as reverse EDX. X-rays are used to probe the sample, and the signal is collected in the form of photoelectrons emitted from the excited samples. The information is collected from a depth of several nm, and contains, in addition to the elemental distribution, data about the chemical states of the atoms in the area of interest. If information about deeper layers of the samples needs to be collected, the depth profile of elementary composition can be obtained by collecting XPS data and etching the sample with ions to expose deeper layers. This is a precise and quantitative method, which is, however, limited by the need to deconvolute a complex signal with poor in-plane spatial resolution due to the difficulty of tightly focusing an x-ray beam.

In this work, XPS was used for a study of the thick layers of porous oxide on UV-oxidized GaAs. For conical microstructures on aluminum alloy and laser tracks of TMDC, it was not well-suited due to the small size or rough surface morphology of those features.

XPS analysis was performed using the PHI 5000 VersaProbe II spectrometer (Materials Science and Metallurgy Shared Use Research and Development Center, NUST MISIS).

Monochromatic Al K α irradiation was used for excitation ($h\nu = 1486,6$ eV). The diameter of the beam and the beam power used were 200 μm and 50 W respectively for analyzing untreated GaAs and 100 μm and 25 W respectively for the laser-irradiated area.

The binding energies of the photoelectrons were found by analyzing high resolution spectra obtained with definition of 0.2 eV/step. The approximation of the spectra was performed by the least squares method using the Gauss-Lorentz function. The calibration of the binding energies was done using the peaks of Au4f – 84.0 eV and Cu2p₃ – 932.6 eV.

1.4.9 Chromatic confocal profilometry

Profiles of rough surfaces can be obtained with considerable (up to ~ 40 nm) precision by using distance sensing based on chromatic confocal imaging (Figure 5). In this method polychromatic light is focused onto a range of distances using a chromatic lens. For a certain wavelength of the incident light, the beam will be focused on the surface of the sample, while for other wavelengths the surface will be out of focus. The reflected or back-scattered light passes through the same chromatic lens and can be filtered with a pinhole. The filtered signal of the wavelength that was reflected or back-scattered at focus will dominate the signal from different wavelengths. By measuring that

wavelength, it is possible to deduce the distance between the chromatic lens and the surface, allowing for collecting profiles.

This technique was used to measure the profiles of ablated areas containing conical microstructures with high aspect ratios. For surface profiles of smoother surfaces corresponding to thin TMDC film laser-irradiated tracks and oxidized GaAs tracks, the more sensitive AFM method was used.

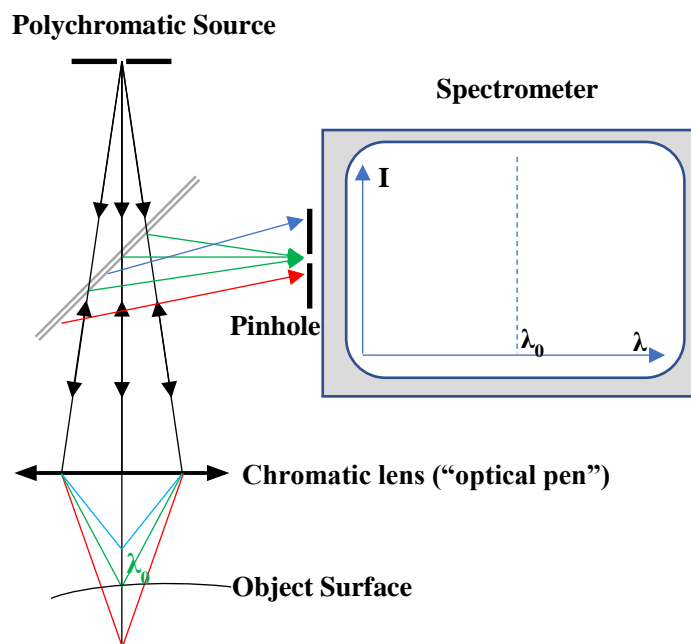


Figure 5 Principle of chromatic confocal profilometry [188].

A confocal laser profilometer CCS Optima+ (STIL SAS, Aix-en Provence, France) with a CL2MG140 optical pen having a z-sensitivity of 40 nm was used for non-contact surface profilometry of conical microstructures on laser-treated aluminum alloy surface.

1.4.10 Atomic Force microscopy (AFM)

AFM is a highly sensitive distance sensing technique that utilizes a thin needle-like probe that approaches the surface of the sample to a distance at which atomic forces can be registered. The probe is attached to a flexible cantilever and moved along the surface of the sample by precise piezoelectric elements. Its position can be tracked by monitoring the reflection of a laser beam from the cantilever. Scanning is executed in a way that maintains a constant force of interaction between the tip of the probe and the surface of the sample or a constant height of the probe, and by recording the position of the probe or the force of interaction, correspondingly, a profile of the surface can be modeled.

Various ways of operating AFM are known, ranging from i) contact mode, in which the probe is kept in constant contact with the surface to ii) semi-contact (tapping) mode, in which the probe oscillates near the surface and periodically enters in contact with it, and to iii) non-contact mode, in which the tip oscillates near the surface without entering in contact. In this work, the NTMDT-SMENA AFM setup was used to scan profiles of laser-irradiated tracks on GaAs crystals and deposited thin films of MoS₂ in the semi-contact (tapping) mode of AFM operation.

1.4.11 Raman spectroscopy

Raman spectroscopy is an essential tool of nanotechnology, allowing to extract information about the vibrations present in the sample, such as oscillations of particular molecules or vibrational modes of crystal lattices. The principle behind it is the use of inelastic photon scattering. While most incidents of scattering involve re-emission of

photons that have the same energy as the adsorbed photons, a small fraction of the excited electrons will relax to an energy level different from the one they got excited from, emitting a photon with a shifted frequency and a different energy. This energy difference usually corresponds to a frequency of oscillations; therefore, the frequency-shifted signal allows to deduce the presence of certain molecular states, estimate crystallinity of materials and detect strains that would shift the frequency of characteristic vibrations. In 2D materials such as graphene and TMDCs, Raman spectroscopy is an indispensable tool. It allows to detect even a flat monolayer film on the substrate, or to distinguish between the number of layers in few-layer films [189].

In this work, Raman spectroscopy was used to validate the laser synthesis of MoS₂ from the precursor compound [190]. The Raman fingerprint of MoS₂ is the presence of characteristic peaks E¹_{2g} and A_{1g}. These peaks correspond to vibration occurring in-plane and out of plane respectively in regards to the atomic layers of MoS₂ [191]. The distance between these Raman peaks depends on the number of layers for few-layer MoS₂ films, and it is increased from ~19 cm⁻¹ to ~25 cm⁻¹ as the thickness of MoS₂ is varied from monolayer to bulk. While the E¹_{2g} peak is red-shifted due to screening of in-plane Mo atom vibrations, the A_{1g} peak is blue-shifted with the interlayer interaction reinforcing the out of plane S atom vibrations.

The LabRAM HR Evolution (HORIBA) system was used to conduct Raman spectroscopy. The 532 nm off-resonance [190] laser irradiation was focused to a spot of ~1-2 μm, allowing to focus in the center of 10 μm wide laser-irradiated tracks.

Chapter 2. Laser processing of technological materials: FIB-SEM characterization

2.1 Individual contributions

The current chapter is based predominantly on the published articles [192] and [193]. In both of those works, Salimon I. A. performed characterization and data analysis.

In the study of AA2024 femtosecond laser scanning was performed at Lasers & Apparatus Ltd., Zelenograd, by Skupnevskiy E.

Salimon I. A. performed all microscopy characterization, (optical, SEM), and confocal profilometry.

FIB cross-section and an EDX measurement were performed by Lipovskikh S. A., under instructions of Salimon I. Integrating sphere measurement was performed by Yagafarov T.A.

On the GaAs oxidation study, Salimon I. A. performed SEM microscopy investigation, and a parametric study of the laser-oxidation process, using the laser-writing.

Additional characterization, namely an FIB cross-section and an EDX measurement were performed by equipment specialist Lipovskikh S. A, and XPS study was performed by Skryleva E. A. at NUST MISIS and AFM study was performed by Novikov A.V. under instructions by Salimon I.

2.2 Chapter summary

In this chapter, treatments of two established technological materials (GaAs crystals and an aluminum alloy used in aeronautics) were revisited with the intent of

obtaining new insight of the underlying physical and chemical processes by applying advanced contemporary characterization methods, namely FIB-SEM cross sectioning and EDX integrated with FIB-SEM. That allowed the investigation of internal topographical and chemical changes that occur underneath the surface of the samples.

C.w. and pulsed laser sources were used to demonstrate the c.w. UV laser oxidation GaAs crystals and femtosecond laser pulse surface modification of the D16T aluminum alloy.

For a study of topography changes, SEM was applied as means of imaging in all cases. However, the choice of means of profilometry was defined by the scale of topography features. In the case of laser induced oxidation of GaAs, it was possible to use AFM in order to achieve high resolution images of the surface topography. However, the severe topographical range involved in the laser-induced roughness of the conical microstructures on ablated D16T alloys required to use the non-contact laser confocal profilometry, which offers a larger dynamic range as compared to AFM.

For the study of chemical changes in GaAs, XPS analysis was performed on large areas of uniform GaAs porous oxide. On the other hand, for elementary analysis of the conical microstructures EDX was used. This technique provides lower qualitative precision in the elementary analysis, but higher spatial resolution. In particular, EDX analysis allowed the mapping of FIB cross sections, as well as investigation of a lamella cut from a single conical structure.

The findings in this chapter reveal the possibility of achieving distinct and complex material rearrangement by direct laser irradiation.

2.3 Localized laser oxidation of GaAs crystals

Here, results that are associated with the interaction of GaAs surfaces with c.w. UV laser radiation at intensities which are several orders of magnitude higher than previous reports [82] but still below the melting threshold are presented. It is shown that under these conditions of irradiation a well defined layer of nanoporous oxide is formed with a thickness of up to several hundreds of nanometers.

Furthermore, self-organized periodic patterning of the oxide layer, which depends on the intensity and polarization of the irradiating laser beam, is observed. This spontaneously formed periodic patterning matches the description for LSFL-II [60]. While LSFL-I induced by ultrafast pulse laser ablation on GaAs were well covered in the literature, the LSFL-II induced by periodically preferential oxidation are a relatively recent observation. It is demonstrated how such structures were induced on GaAs with c.w. UV irradiation.

Observations are presented such as topography data, obtained by FIB-SEM and AFM microscopy techniques, and composition mapping data, obtained by electron dispersive X-ray (EDX) and X-ray photoelectron spectroscopy (XPS) analysis.

2.3.1 *Experimental procedures*

The sample used in our experiments was a section of an undoped semi-insulating GaAs (100) wafer with a thickness of 0.5 mm that was supplied by our collaborators. Such high quality wafers are used for MBE growth of semiconductor microcavities.

For laser irradiation, it was chosen to define the varying laser irradiation parameters varied as laser intensity and beam “dwell time”, which is derived from the

scanning speed and the laser spot size at focus. The peak intensity and the scanning speed range used were 2.6 - 45 kW/cm² and 3 - 60 μm/s respectively. The corresponding dwell times varied between 0.2 s and 4 s.

Larger irradiated areas of approximately 1x1 mm², which were required for conducting composition studies, were produced by overlapping adjacent laser irradiated tracks in a raster scanning fashion.

2.3.2 SEM surface topography investigation

The SEM images which are shown in Figure 6a,b correspond to sections of UV laser irradiated tracks obtained using different orientations of the laser beam polarization with respect to the scanning direction. The all-white double arrowhead lines superimposed to the image indicate the orientation of the beam polarization. The white-outlined arrow corresponds to the direction of scanning. Both images (Figure 6a,b) show a porous central section that runs along the scanning direction. This section corresponds to the peak intensity region at the center of the Gaussian beam intensity distribution. On either side of this central region regular (periodic) surface features can be observed, which correspond to lower laser intensities. These features are slightly curved stripes of darker SEM contrast separated by lines or brighter SEM contrast. These lines are oriented very closely to the direction of polarization. These lines fit the description of LIPSS, particularly LSFL-II. By adjusting the irradiation conditions (laser beam intensity and dwell time), it was possible to obtain regular LIPSS across the whole width of the track, as shown in Figure 6c.

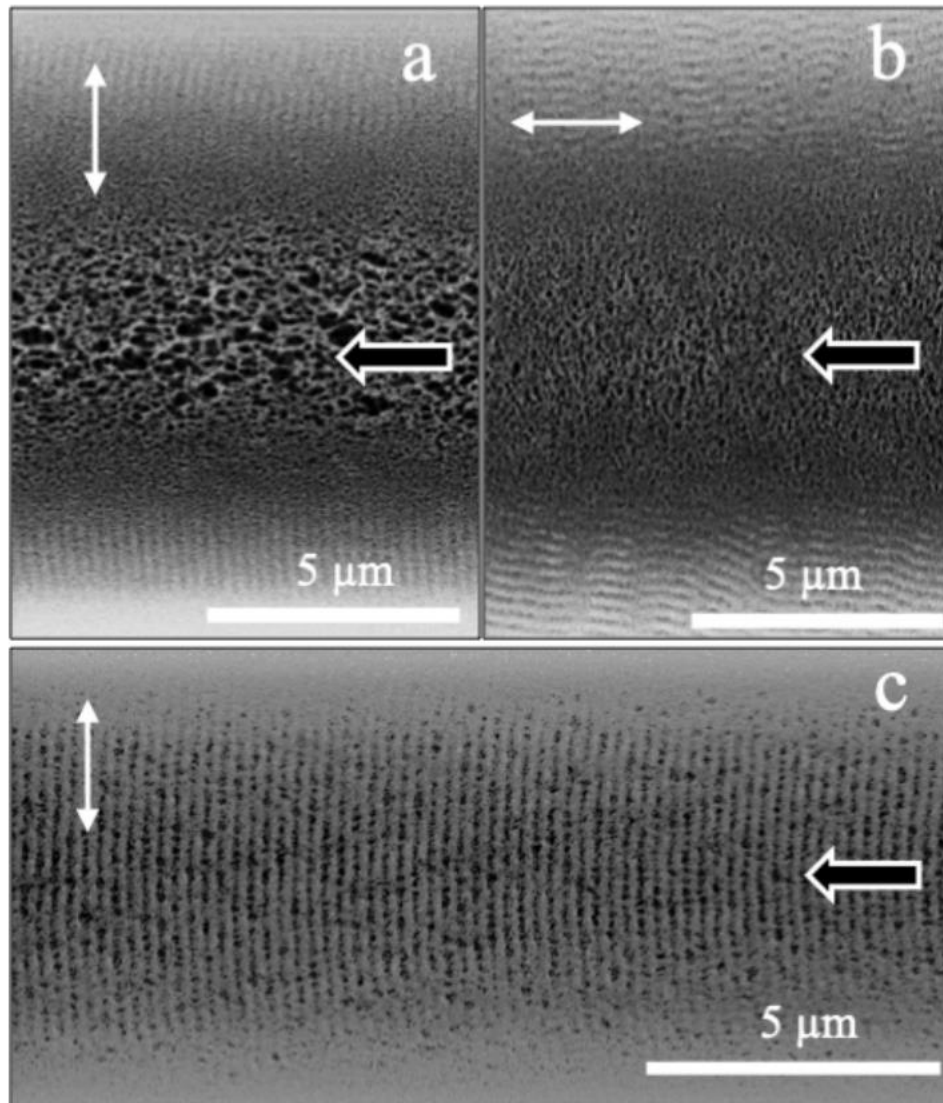


Figure 6 a) SEM image of laser-induced topography modifications corresponding to a single laser-irradiated track. The Gaussian intensity distribution of the laser beam allows the simultaneous observation of laser-induced porosity (at the central region of the track) and laser-induced periodic surface structures (LIPSS) at the periphery of the track. The polarization of the beam is perpendicular to the scanning direction. b) SEM image of GaAs surface topography changes observed on a single track with polarization parallel to

the scanning direction. c) Regular LIPSS patterns are formed throughout the width of the track using appropriate irradiation conditions. The laser scanning direction is indicated by the white outline arrow, while the solid white double arrowhead lines indicate the polarization of the irradiating beam.

Assuming a Gaussian beam profile, one can assign an intensity range to various sections of the track that is shown in Figure 6a. The peak intensity (corresponding to the center of the track) was estimated in this way to be $\sim 45 \text{ kW/cm}^2$. The periodic features (LIPSS) appear at intensities between 12 and 22 kW/cm^2 . The scanning speed was $6 \text{ }\mu\text{m/s}$, which corresponds to a dwell time of $\sim 2 \text{ s}$.

The LIPSS observed here have a period of 253 nm , which is very close to the wavelength of the laser. This characteristic fits the description for LSFL-II observed in ultrafast laser irradiation of Si [60] and thin metal films [71].

LIPSS that are formed by static irradiation of the surface and those formed by scanning performed along the polarization of the incident laser beam appear to be distorted, noticeably affected by surface defects, as shown in Figure 6b and Figure 7. On Figure 7, one can observe how the zigzag-like trajectory of a crack is repeated and propagated by the LIPSS formed by static irradiation.

This distortion is greatly reduced in dynamic (scanned) irradiation experiments when the polarization of the beam is perpendicular to the scanning direction. In this case spatially regular LIPSS are formed, which are also oriented perpendicular to the direction of the track (Figure 6c). This increase in regularity is caused by the presence of an

additional positive feedback. As the scanning progresses, the already induced LIPSS cause diffraction which reinforces the induction of the next LIPSS down the line. That positive feedback is absent when the polarization (and, therefore, the LIPSS) are oriented along the direction of the scanning, leading to a less orderly structure.

No evidence of anisotropy having a strong effect on formation of LSFL-II was registered. Scanning performed under various random orientations of the GaAs crystal led to similar results. It is likely that the directionality of LSFL-II formation outpaces such anisotropy.

The question could be raised about whether it is possible to achieve uniform coverage of LIPSS features over large areas by using c.w. UV irradiation. One avenue to achieve this is to expand the beam spot by drifting slightly away from focus. This allowed to induce LIPSS fringes that are more than 38 μm long. While the structures observed in this way look slightly curved, they are quite regular over distances of several tens of microns (Figure 8).

Periodic micro texturing (LIPSS) can be used as a diffractive optical element for coupling of light in optical waveguides, and has been demonstrated to be suited for reducing reflective losses in photonic devices [194]. It may be possible that a single step irradiation procedure could be used to create an oxide layer that serves for both protection and modification of optical properties on the surface of GaAs.

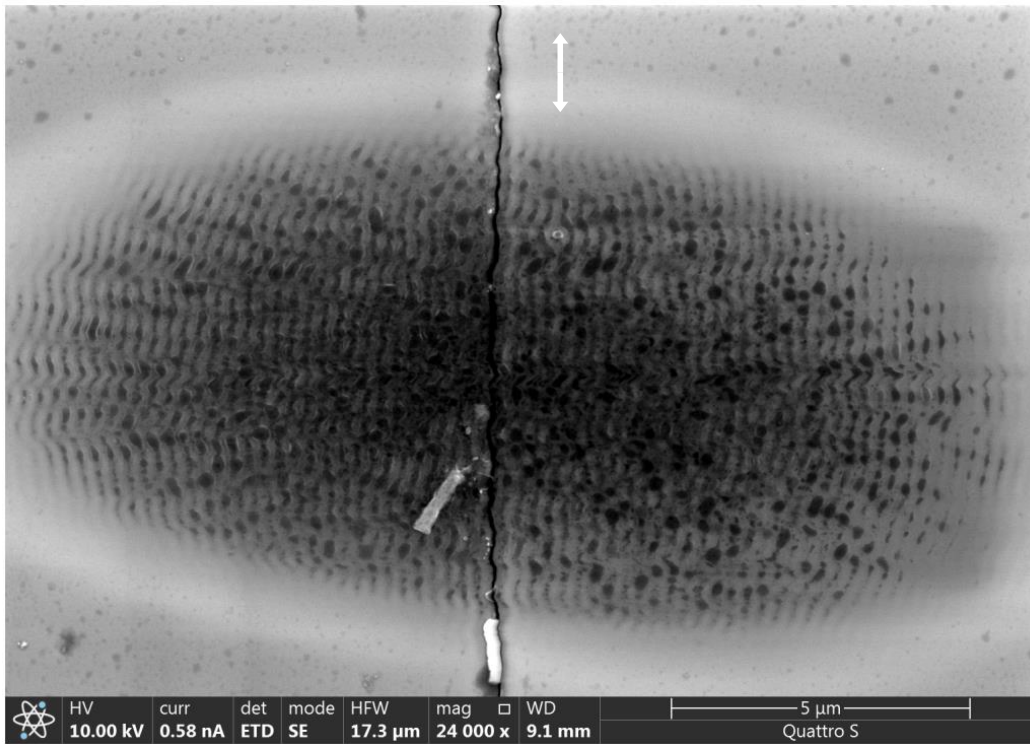


Figure 7 Distortion in the LIPSS patterns observed after static laser beam exposure of an area with a surface defect (crack with a zigzag-like trajectory).

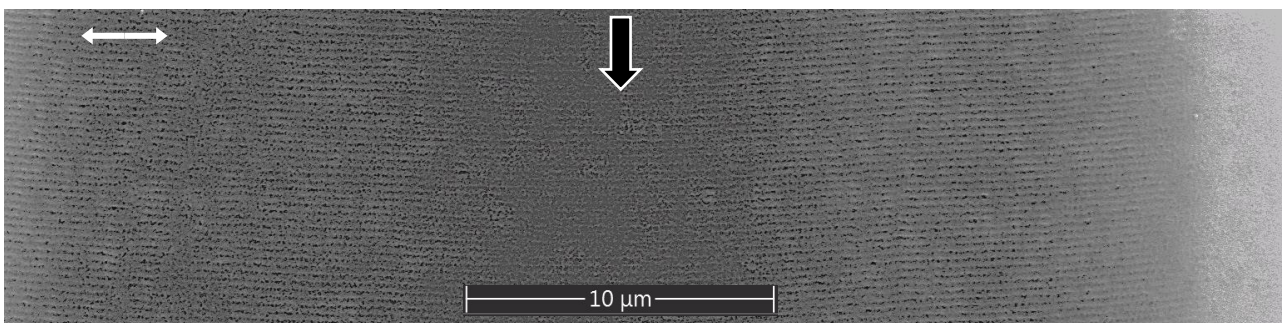


Figure 8 LIPSS produced by expanding the beam spot during laser scanning. The laser scanning direction is indicated by the white outline arrow, while the solid white double arrowhead line indicates the polarization of the irradiating beam.

2.3.3 AFM surface topography investigation

The AFM topography map, which is presented in Figure 9, shows a 200 nm elevation at the center of the laser irradiated track, which reduces with the distance away from the center and eventually reaches the level of the non exposed crystal outside the track. The LIPSS features, which have heights between 4 and 20 nm, are superimposed onto the swollen surface, as shown in the AFM topography map.

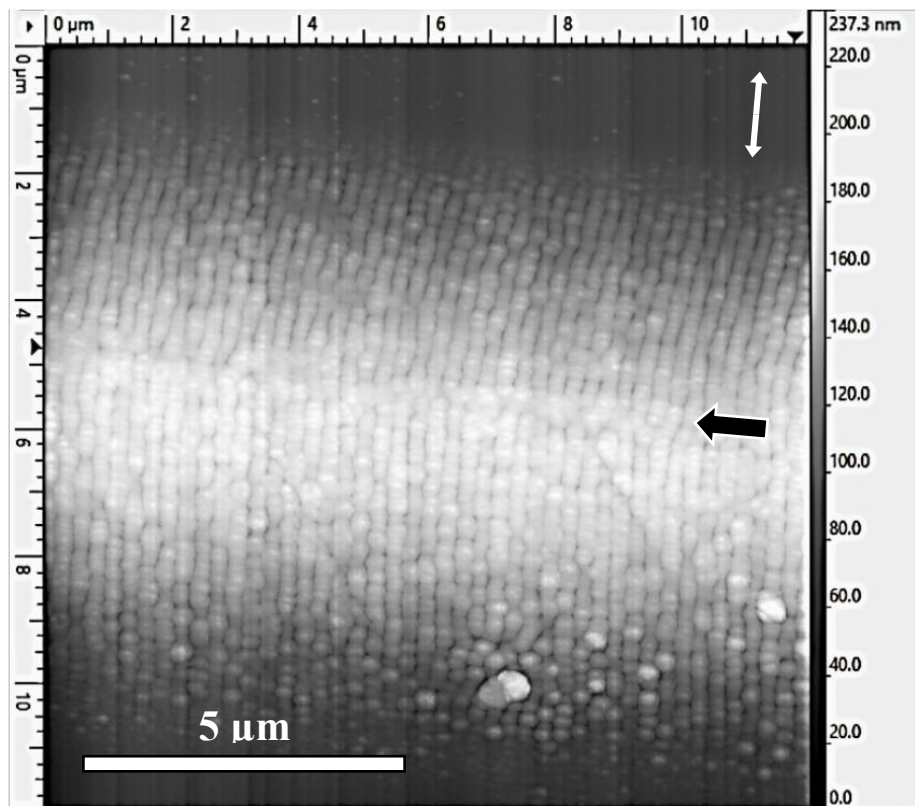


Figure 9 AFM topography map of a single track section with LIPSS. The peak laser intensity used for the UV laser irradiation was 12 kW/cm^2 and the scanning speed was 6 μm/s .

The elevation of the irradiated crystal surface suggests that laser irradiation causes some structural/chemical change in the material which leads to volume change. It will be shown later that the UV laser irradiation leads to the formation of a porous oxide layer. The thickness of this porous oxide layers is associated with the laser beam intensity distribution. This was confirmed by the FIB-SEM investigation, which is presented below.

2.3.4 FIB-SEM and EDX examination of internal composition of deep porous oxide layers

A larger irradiated square-shaped area with a size of approximately $1 \times 1 \text{ mm}^2$ was required to facilitate composition analysis of the lased processed region. This was achieved by raster scanning of the surface, using $\sim 90\%$ overlap between adjacent tracks. An SEM image of this region is shown in Figure 10a.

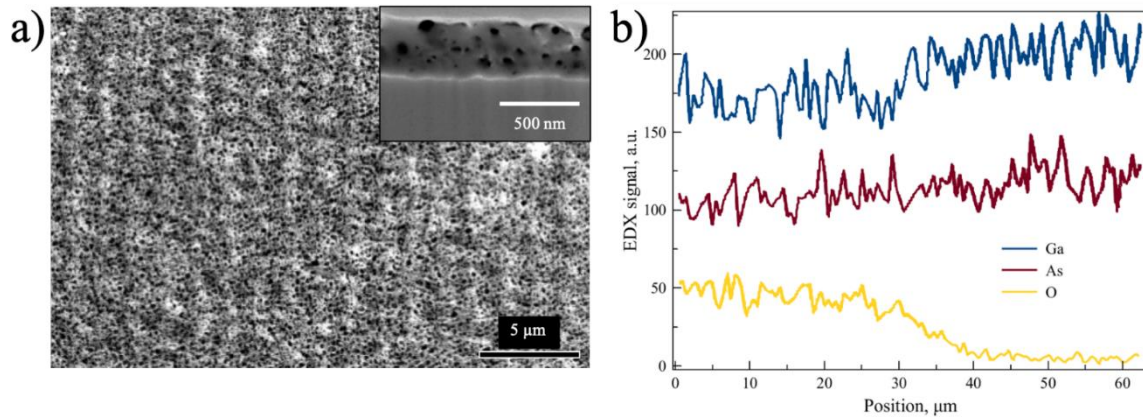


Figure 10 a) SEM image of the uniform porous layer obtained by overlapping adjacent laser tracks. Inset: Cross section of the porous GaAs layer viewed at an angle of 52° . The cross section was produced using FIB etching. The unaffected GaAs crystal can be seen

under the porous layer. b) Plot of oxygen, gallium and arsenic levels, as a function of position, acquired along a line that is parallel to the surface. That line begins on the irradiated area and crosses the border between the irradiated area and virgin surface at the 35 μm mark. The corresponding sections on the plot are: irradiated 0 - 35 μm , non-irradiated 35 - 65 μm .

The surface appears to be mostly uniform; however, a shallow modulation in the topography can be observed due to the raster scanned origin of the pattern. A cross section was produced on a central location of this area using focused ion beam milling (FIB), to investigate the extent of the laser affected zone. The SEM image of the cross section, shown in the inset of Figure 10a, reveals the presence of a porous layer with a thickness of ~ 380 nm, which contains voids with sizes of order 50 - 100 nm. This layer appears to form a sharp interface with the underlying GaAs crystal. EDX provides composition data with a depth selectivity of ~ 1 μm ; however, the exact depth selectivity might vary in our case due to the unknown density of the porous oxide layer. EDX data was collected along a path that traverses the boundary between the raster scanned area and the virgin (non-irradiated) crystal surface, for comparison. Figure 10b shows a plot of oxygen, gallium and arsenic levels, as a function of position, along a path with a length of 65 μm . The plot indicates a clear increase of the oxygen level at positions between 0 and 35 μm , which corresponds to the laser irradiated section, thus indicating the formation of oxide. A slight decrease of Ga and As levels that can also be observed in the same region is probably associated with the porous nature of the oxide that is formed.

Spatially selective growth of porous oxide can be used as a thermal, acoustic and electrical barrier and as optical diffuser, while the increased surface area, due to porosity, may be beneficial for sensing applications. The creation of porous oxide by UV irradiation of GaAs crystalline wafers may offer a simpler alternative to the anodic etching and oxidation of GaAs [195].

2.3.5 XPS examination of elementary content

Composition profiles of the GaAs specimen were obtained from both the virgin and laser irradiated areas using Ar⁺ ions sputtering and XPS analysis. The survey spectra for an untreated area of GaAs used as reference and the UV laser raster scanned area are provided on Figure 11, Figure 12 and Figure 13. After initial purification, the evaluation of elemental concentration by XPS showed complete removal of surface adsorbed hydrocarbons, while oxygen remained on the surface. The composition profile that corresponds to the virgin area is presented in the plot of Figure 14a.

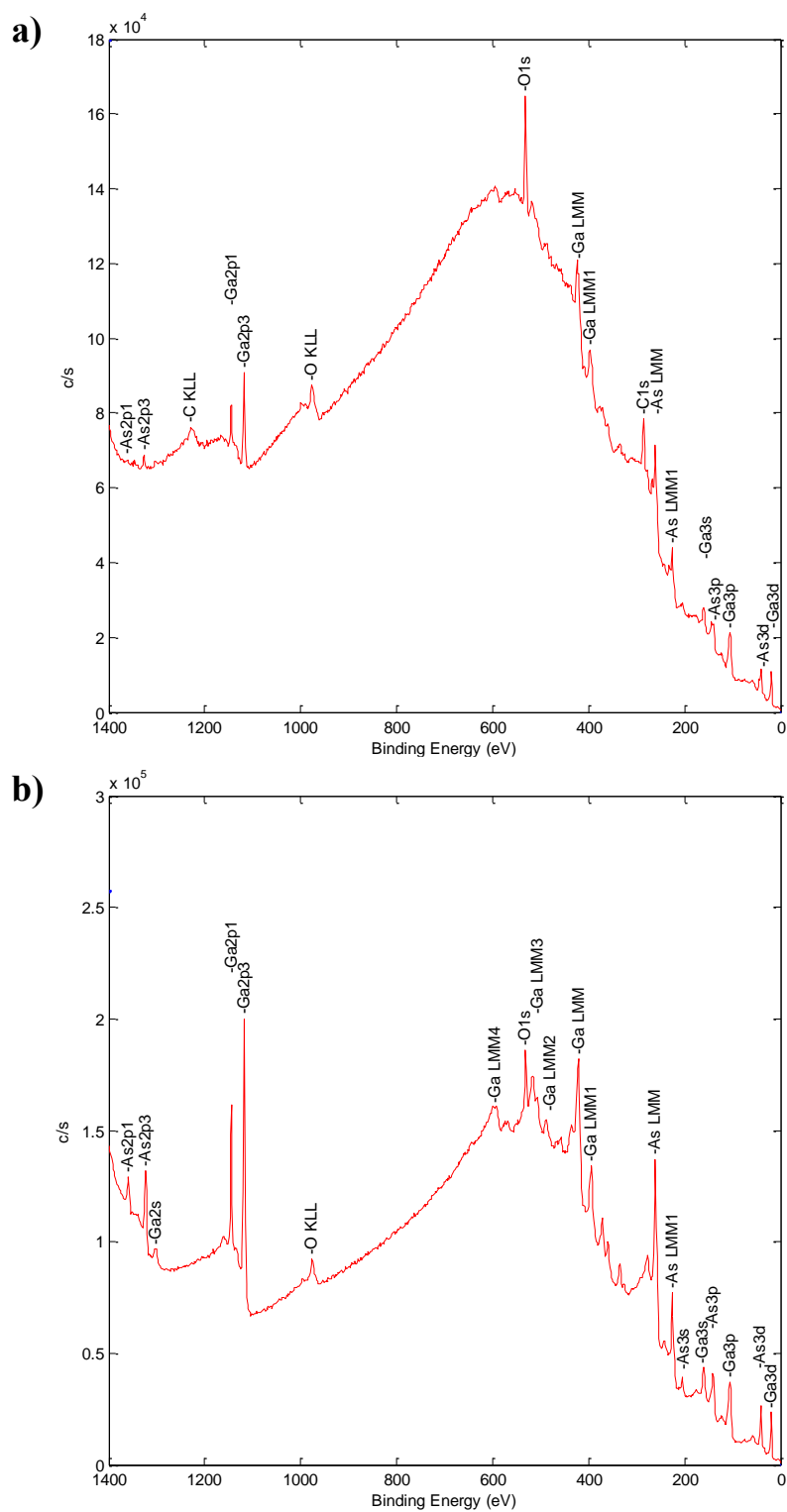


Figure 11 Survey spectra of a non-irradiated area a) before and b) after purification.

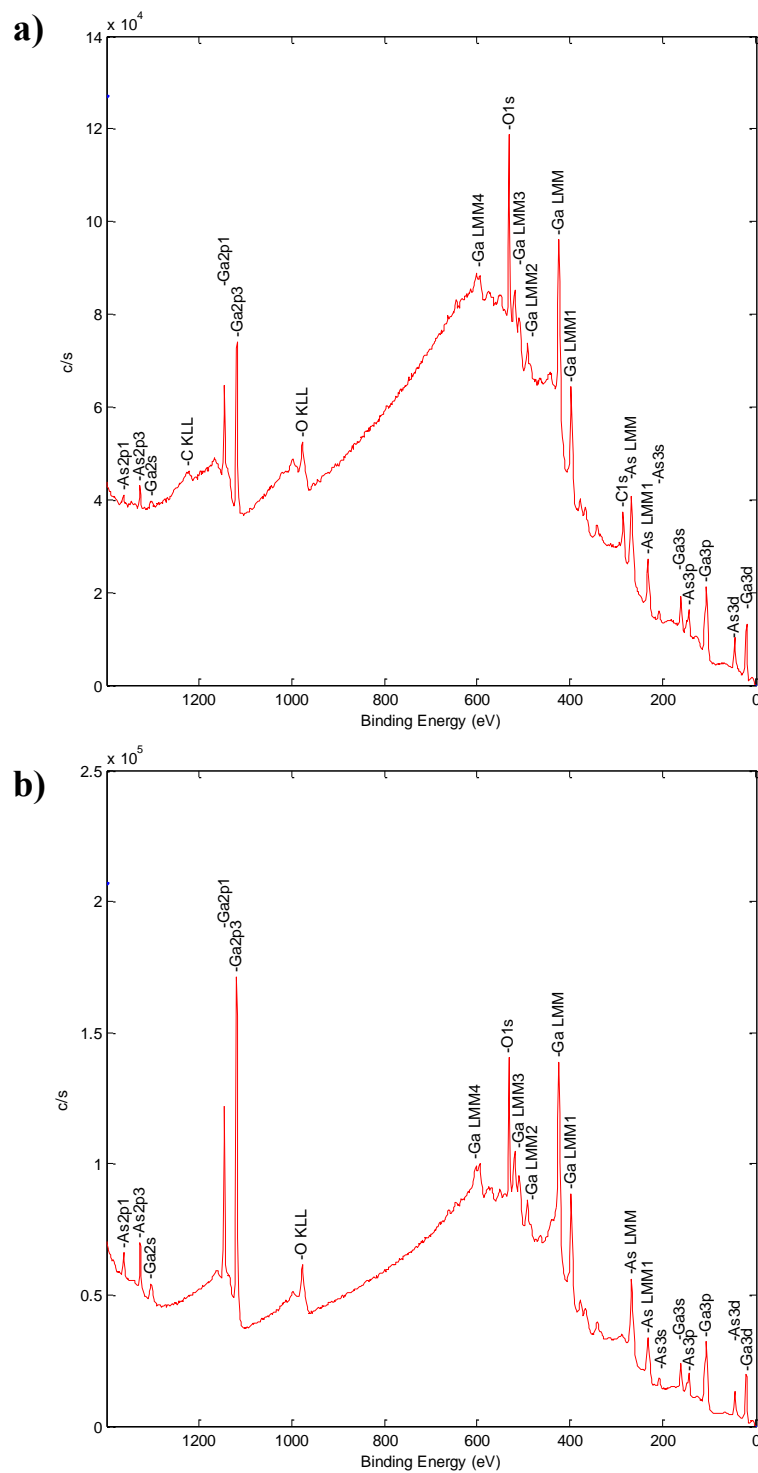


Figure 12 Survey spectra of the laser-irradiated area a) before and b) after purification.

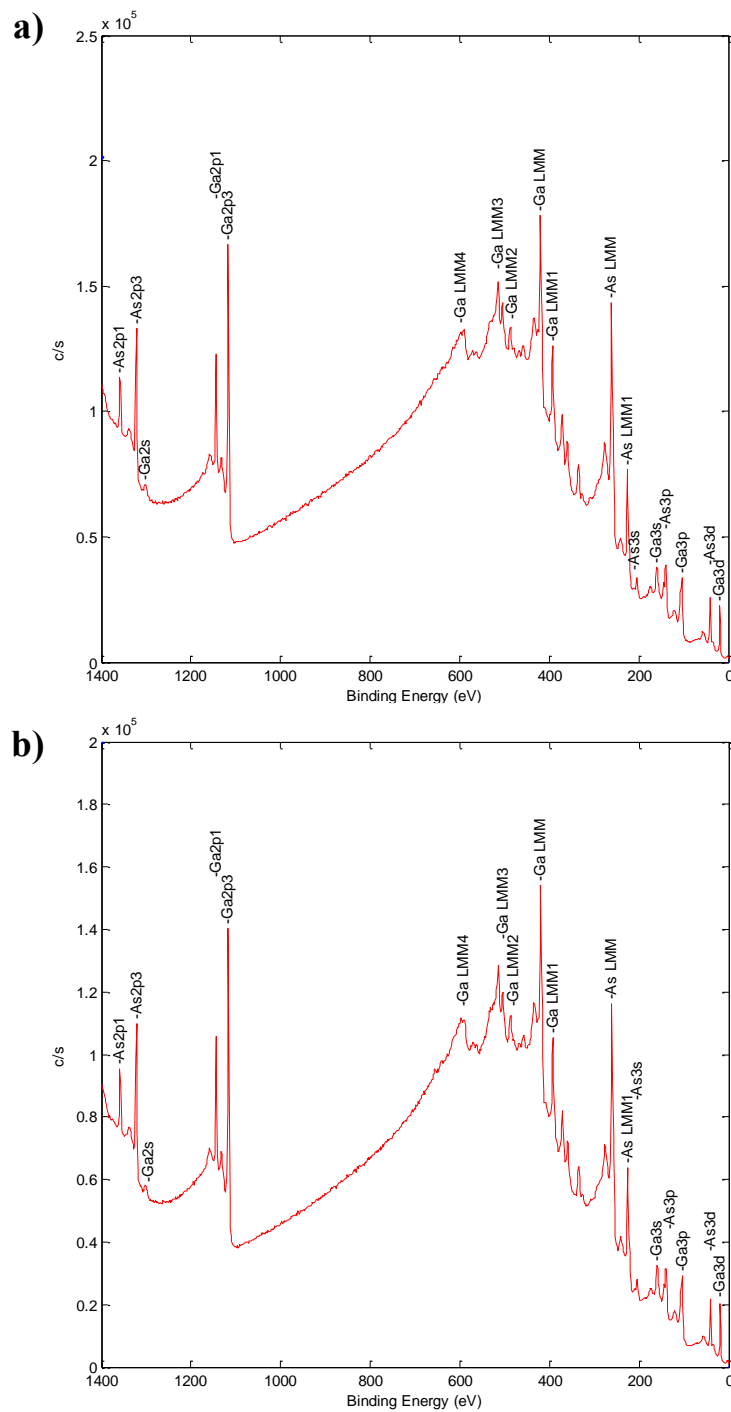


Figure 13 Survey spectra of a) a non-irradiated area after 4.2 min of Ar^+ 1 keV ion etching and b) the laser-irradiated area after 4.2 min of Ar^+ 1 keV ion etching and 9 min of Ar^+ 2 keV.

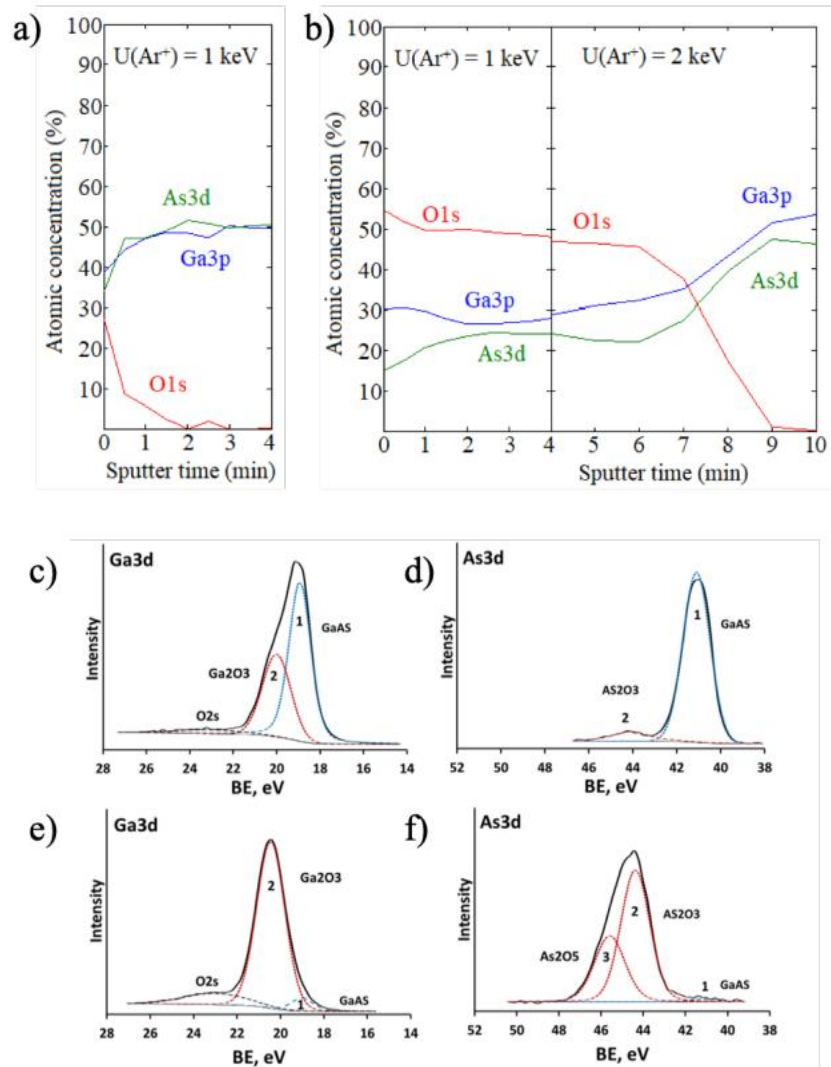


Figure 14 a,b) Concentration profiles, estimated by XPS, for Ga, As and O on: (a) non-irradiated area and (b) UV laser raster scanned area, as a function of etching time. c-f) High resolution XPS spectra of the binding energy (BE) of Ga3d and As3d. Spectra c, d correspond to the non-irradiated crystal surface. Spectra e, f correspond to the laser-irradiated area. Solid black lines correspond to experimental spectra, blue dash lines correspond to fitted GaAs peak, red dash lines correspond to fitted oxide peaks.

This plot shows concentration levels for oxygen, arsenic and gallium as a function of ion etching time. The level of oxygen is shown to drop promptly within 2 mins of Ar⁺ etching (at 1 keV), which is consistent with the removal of natural oxides that are expected to form on the surface of GaAs crystals that have been stored in ambient conditions. The composition profile that corresponds to the laser irradiated area is shown in the plot of Figure 14b. The plot is divided into two parts, with the first part corresponding to an initial etching regime of 4 min, at 1 keV, mirroring the analysis of the virgin area of the sample. Here however, the concentration of oxygen remained mostly constant throughout the duration of the etching. The sample was then etched for a further 6 mins at 2 keV energy to ensure that the oxygen level drops to zero. As the etching rate depends on the type of material that is being etched, it is not trivial to estimate the etch depth from the etch time data. However, it is reasonable to assume that the constant level of oxygen throughout the first 6 mins of etching is associated with the porous layer. Beyond that point the oxygen level drops while the partial concentrations of Ga and As equal 50% indicating that the GaAs substrate has been reached.

High resolution (HR) XPS spectra for Ga and As are shown in Figure 14(c-f). The spectra were recorded using a pass energy of 23.5 eV at a 0.2 eV/step and were fitted by nonlinear least-squares method using mixed Gaussian–Lorentzian peak shape with data sourced from [196].

Spectra corresponding to the non-irradiated area (c,d) display significant presence of Ga and As peaks, which are associated with bonds in the GaAs crystal. These peaks are shown in blue dash line and are indicated by "1" in the spectra. Oxide peaks

associated with Ga_2O_3 and As_2O_3 are also present, but are in general of lower intensity. The oxide peaks are shown in red dash curves indicated by "2" in the spectra. The situation is reversed on the laser irradiated area, where the corresponding spectra (e,f) are dominated by oxide peaks, though weak GaAs peaks are still present. By analyzing the relative intensities of the peaks, it is possible to estimate the portion of non-oxidized GaAs in the treated area as $4 \pm 0.2\%$. A peak related to strongly oxidized As⁵⁺ (red dash line indicated by "3") was observed. This peak was more prominent closer to the surface of the investigated area.

Previous studies on the UV oxidation of GaAs identified the importance of photocarriers and molecular photodesorption, as GaAs absorbs UV light very strongly [82] (absorption depth of order $\sim 50 \text{ \AA}$, at 244 nm). Irradiation of the surface of the material with light at wavelengths shorter than 300 nm (photon energies higher than 4.1 eV) has been shown to increase the rate of oxidation significantly and allow this oxidation process to reach several monolayers by enabling mass-transport of oxidant species to the bulk GaAs/oxide layer interface [82]. Moreover, light with a wavelength of 242 nm (5.1 eV) and shorter can dissociate the ambient molecular oxygen, further facilitating oxidation. In this work, intensities of several tens of kW/cm^2 were used, which is many orders of magnitude higher than previously reported in the literature [82] ($50 \text{ mW}/\text{cm}^2$) but still below the threshold for melting or ablation of the GaAs crystal: for the range of beam intensities presented, no melting of GaAs was observed. As the wavelength of 244 nm that was used does not create O_3 efficiently [197], it can be

concluded that it is the local heating and the transport of O_2^- ions [82], caused by the highly absorbed UV irradiation, that expedites oxidation of the surface.

We anticipate that the oxidation process is dependent on the doping of GaAs in a way similar to anodic electrochemical oxidation [198] or liquid phase chemical enhanced oxidation [119], where the process depends on the hole concentration. In liquid phase chemical enhanced oxidation without illumination, the oxidation rate is highest for p^+ doping due to the availability of holes. However, under illumination the oxidation rate grows, and it grows much more for n^+ doped GaAs, since the photogenerated holes are drawn to the interface, while for p^+ doping photogenerated holes are repelled from the interface [119]. However, we could also point out that the amount of photogenerated carriers should be much greater compared to illumination with a lamp [119], possibly leading to different and likely lower doping dependence.

A probable reason for porosity of the oxidized layer could be sublimation of oxides of Ga and As. It is known that at temperatures above 440 °C the Ga_2O suboxide becomes volatile, with its sublimation forming pits up to 11 nm deep, thermally inducing substantial mass transport [199]. Growth of larger pores could be promoted by additional mass transport induced by UV irradiation [82].

2.3.6 Concluding remarks

A range of intensities higher than those reported previously was investigated in UV oxidation of GaAs. Overall, it was shown that irradiation of GaAs single crystals with c.w. UV laser radiation leads to the formation of a localized porous oxide layer that extends to a depth of $\sim 0.4 \mu\text{m}$ below the surface. The internal structure of the porous

oxide was revealed by FIB-SEM cross-section examination and found to be uniform, with voids up to ~100 nm in diameter. The composition profile of the oxidized layer has been confirmed by XPS investigation to retain a high degree of stoichiometry. UV treatment offers a simpler alternative way to obtain porous oxide of GaAs, which is currently obtained through electrochemical processes.

There exists a range of irradiation conditions in which low spatial frequency LIPSS were induced by c.w. irradiation. This phenomenon offers diverse applications including modification of optical properties. These LIPSS are formed parallel to the laser beam polarization, fitting the description of LSFL-II. The observed LIPSS are not ablative, but rather thermochemical [76] and photo-chemical in nature; they consist of periodically oxidized sections. These features may uniformly cover large areas.

2.4 Surface modification of aluminum alloy by femtosecond pulsed laser scanning

Here, observations on ultrafast laser processing of the D16T alloy are presented. This Russian designation describes an alloy that is fully equivalent to the alloy AA2024-T4 according to the International Alloy Designation system. This type of artificially aged Al-Cu alloy is used in aviation because of its attractive mechanical properties (e.g., strength-to-weight ratio) and resistance to mechanical damage.

In this work, an FIB-SEM investigation has revealed the inhomogeneous internal contents of the conical microstructures with tips formed by re-deposition of ablated material. Such inhomogeneous surface layers formed by re-deposition were not reported

in the previous works that did contain FIB dissections of conical microstructures formed by femtosecond pulse laser ablation. The EDX study of the lamella cut from the tips of such a microstructure confirmed that the layer of re-deposited material of the alloy substrate is non-uniform in elemental content and contains voids. The re-deposition of the ablated material is shown to be significantly dependent from the parameters of repetitive scanning.

For the aluminum alloys in particular, there is interest in studying the corrosion mechanism to improve resistance to corrosion, including the use of laser-based methods such as laser surface melting (LSM). The introduced elemental inhomogeneity of the alloy's surface has an effect on its corrosive properties, which may be positive or negative (for AA2014-T6, LSM was shown to cause significant reduction of pitting potential, while for AA2024-T351 the treatment caused less significant increase of the pitting potential) [128]. This emphasizes the relevance of an in-depth FIB-SEM investigation of the conical microstructures obtained through ablation.

2.4.1 Femtosecond laser irradiation of D16T sample

The flat surface of a mechanically polished cylinder (diameter 20 mm, height 5 mm) of D16T alloy (Table 1) was irradiated using laser pulses with energy fluence varying over the range of 5 to 33 J/cm² (Figure 15a and Table 2). Roman numerals in the figure correspond to the energy fluence of the laser pulses; “I” corresponding to 5 J/cm² through to “VII” that corresponds to 33 J/cm².

Table 1. D16T elementary composition.

Element	Weight %
Al	Balance
Cu	4.239 ± 0.073
Mg	1.754 ± 0.037
Mn	0.532 ± 0.0044
Fe	0.346 ± 0.011
Si	0.223 ± 0.0057
Zn	0.152 ± 0.00071
Ti	0.047 ± 0.001
Cr	0.016 ± 0.001

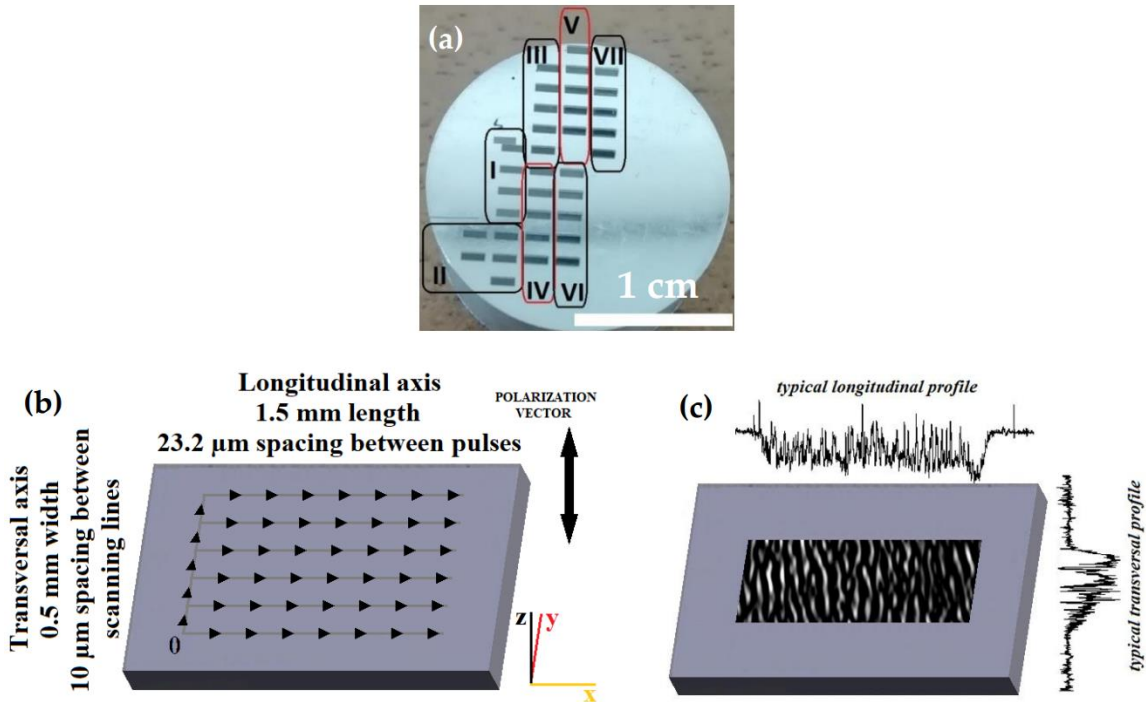


Figure 15 Layout and principal geometry characteristics of laser treatment: (a) photograph of the top surface of the cylindrical D16T sample, with the various irradiated areas marked; (b) laser scan schematic diagram, with space coordinate system shown and scanning (long arrows) and scan progression (short arrows) directions indicated; (c) typical treated area schematic, with typical profiles shown.

Table 2. Laser beam spot parameters for different treatment series.

Scanning series	Pulse energy, μJ	Energy fluence, J/cm^2
I	60	5
II	110	9
III	160	13

IV	210	17
V	260	21
VI	310	25
VII	400	33

An MLP1-2106 (Lasers & Apparatus Ltd., Zelenograd, Russia) device in a customized commercial setup was used. Scanning of each individual area was achieved by redirecting the beam with a scan head (HurryScan 14, SCANLAB, Puchheim, Germany), whereas switching between different areas was done by moving the stage.

The incident laser beam was linearly polarized along the y-axis direction (Figure 15b). The laser source used was Yb:YAG (TETA-10, Avesta, Troitsk, Russia) emitting at a wavelength of 1033 ± 3 nm. The laser beam (with a diameter of 12 mm) was focused using an F-theta lens with a 70 mm focus distance. Rectangular areas with dimensions: 1.5×0.5 mm² were laser-scanned longitudinally in the x-axis direction for all laser beam tracks (Figure 15b). The focused beam radius was evaluated to be 35 μ m by observing the area affected by a single pulse. The repetition rate was 25 kHz, and the scanning speeds was 580 mm/s, which results in a 23.2 μ m distance between traversed by the beam between sequential pulses. That was calculated to produce a 34% overlap along the scanning track. To ensure that each point of treated areas was exposed to intensity values that are close to the peak of the Gaussian beam, a distance of 10 μ m was chosen between scanning tracks, resulting in a 71% overlap between adjacent tracks.

For each value of energy, the scan repetition (SR) number (indicating the amount of full scan pattern repetitions) varied from 1 to 5.

2.4.2 Confocal profilometry of ablated areas

Transversal and longitudinal profiles of the ablated areas were investigated by confocal surface profilometry (Figure 16).

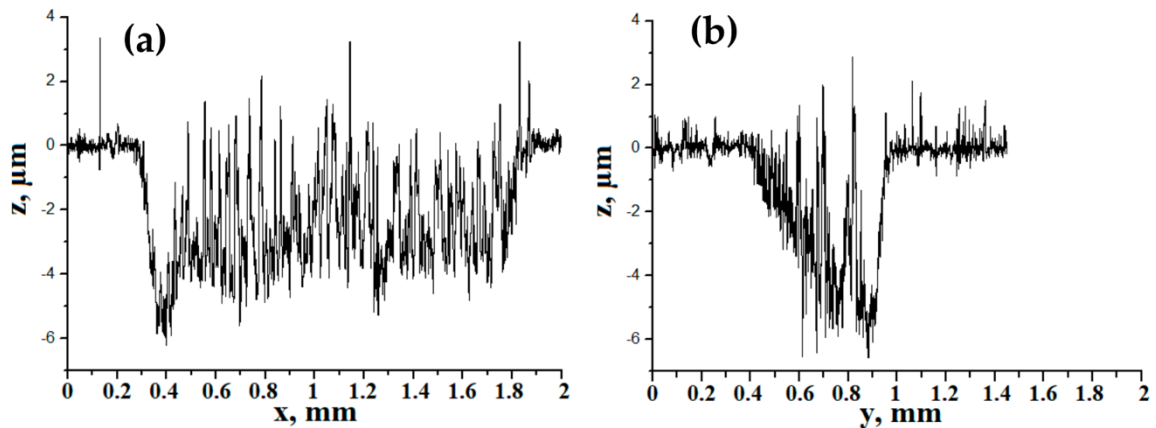


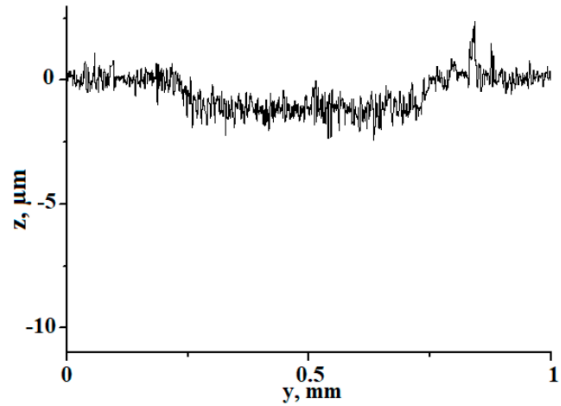
Figure 16 Typical ablation profiles for 21 J/cm^2 . The profiles shown here correspond to an area that was subjected to three scan repetitions (SR): (a) longitudinal profile of treated area; (b) transversal profile of treated area.

A dip is observable at the side where the scanning lines start (Figure 16a, left side of the graph). This is due to the beam not being blocked when it switches between scanning lines and lingers for a brief moment to stabilize the scanning stage before beginning a new scanning track (Figure 15b). The transversal profile is non-uniform, deeper, and rougher on one side than on the other; and the mean depth has a noticeable slope, unlike the longitudinal profile, which is uniform, in comparison, with a constant

mean depth value. The shallower side of the transversal profile corresponds to the side where the laser beam starts the first scanning track. Possible reasons for this effect are discussed later.

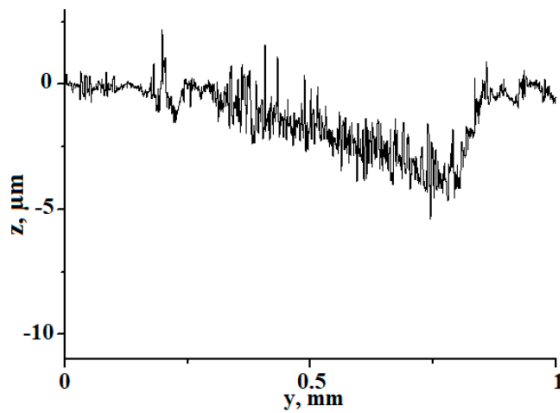
A color-coded chart characterizing the profiles of the treated areas is provided (Figure 17a). The number of scan repetitions was varied from 1 to 5 from left to right; the energy fluence varied from 13 J/cm^2 to 33 J/cm^2 from top to bottom. The profiles corresponding to a lower energy fluence (less than 13 J/cm^2) could not be reliably registered due to low signal-to-noise ratio.

	1 SR	2 SR	3 SR	4 SR	5 SR
13 J/cm ²	Green	Green	Green	Green	Red
17 J/cm ²	Yellow	Yellow	Red	Red	Red
21 J/cm ²	White	Yellow	Red	Red	Red
25 J/cm ²	Yellow	Yellow	Red	Red	Red
33 J/cm ²	Yellow	Red	Red	Red	Red

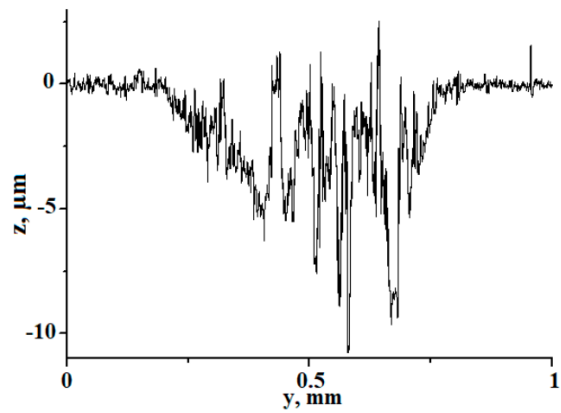


(a)

(b)



(c)



(d)

Figure 17 Profiles of laser-treated areas: (a) color-coded chart; (b) example profile for “green” profiles which are parallel to the initial surface; (c) example profile for “yellow” profiles with an observable slope; (d) example profile for “red” profiles with high roughness. SR: scan repetitions.

Three different trends can be deduced from the diagram. First, for 13 J/cm², the profile mean lines are parallel to the surface and they have relatively low roughness until spiky peaks appear at higher numbers of pulse repetitions; that range is marked in green.

A representative surface profile is provided (Figure 17b). The depth of the profiles increases monotonously with the number of pulses (Figure 18a).

Second, at a higher energy treatment, the spiky peaks are not yet identifiable on the profiles after smaller numbers of pulse repetitions, but the profile mean lines are noticeably sloped; those profiles are marked in yellow. A representative surface profile is provided (Figure 17c). The mean slope angle of the profile increases with both energy and the number of pulse repetitions (Figure 18b). The slope angle is small but always positive. The 21 J/cm² one-repetition treated area is excluded, since it was too close to the edge and was curved due to polishing.

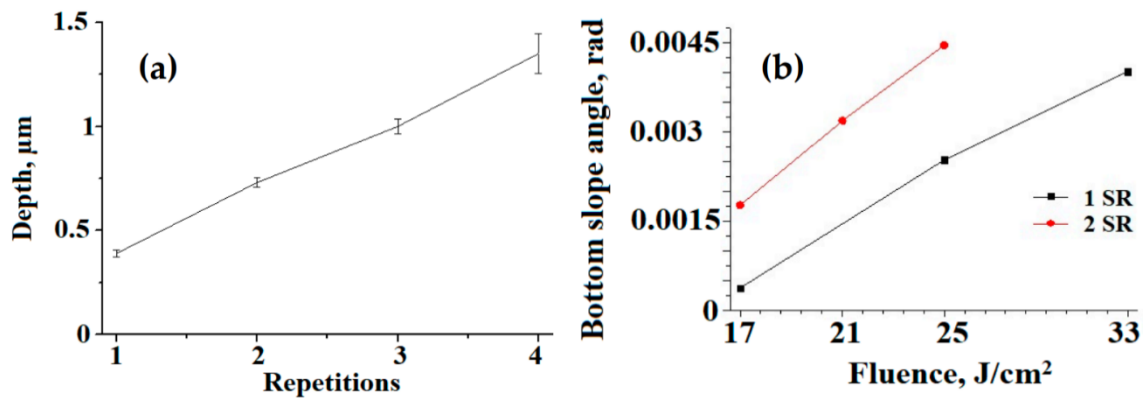


Figure 18 Profile parameters: a) depth of laser-treated areas at 160 μJ; (b) average slope angle of treated area bottom.

Finally, at high values of energy and numbers of pulse repetitions, the profiles reveal abrupt peaks and dips, and their height increases with energy and number of pulse repetitions. Those profiles are marked in red. A representative surface profile is provided (Figure 17d). In general, such transversal profiles show uneven roughness — the peak-

dip pattern is deeper and rougher at the side of the treated area where the laser beam was scanning later.

It should be acknowledged that this method requires that the sample provides sufficient reflectance, as it relies on collecting a reflected signal. The optical properties of the laser treated areas will be explored in more detail below by using an integrating sphere. The method of confocal profilometry provides accurate data for smooth profiles marked in green and yellow. For profiles marked in red corresponding to highly rough surfaces, the qualitative precision of the method may be significantly reduced due to the low reflectivity of the treated area.

2.4.3 SEM surface topography investigation

The collage of SEM images characterizing the appearance of treated areas is given in Figure 19 as a function of laser beam energy and number of scan repetitions.

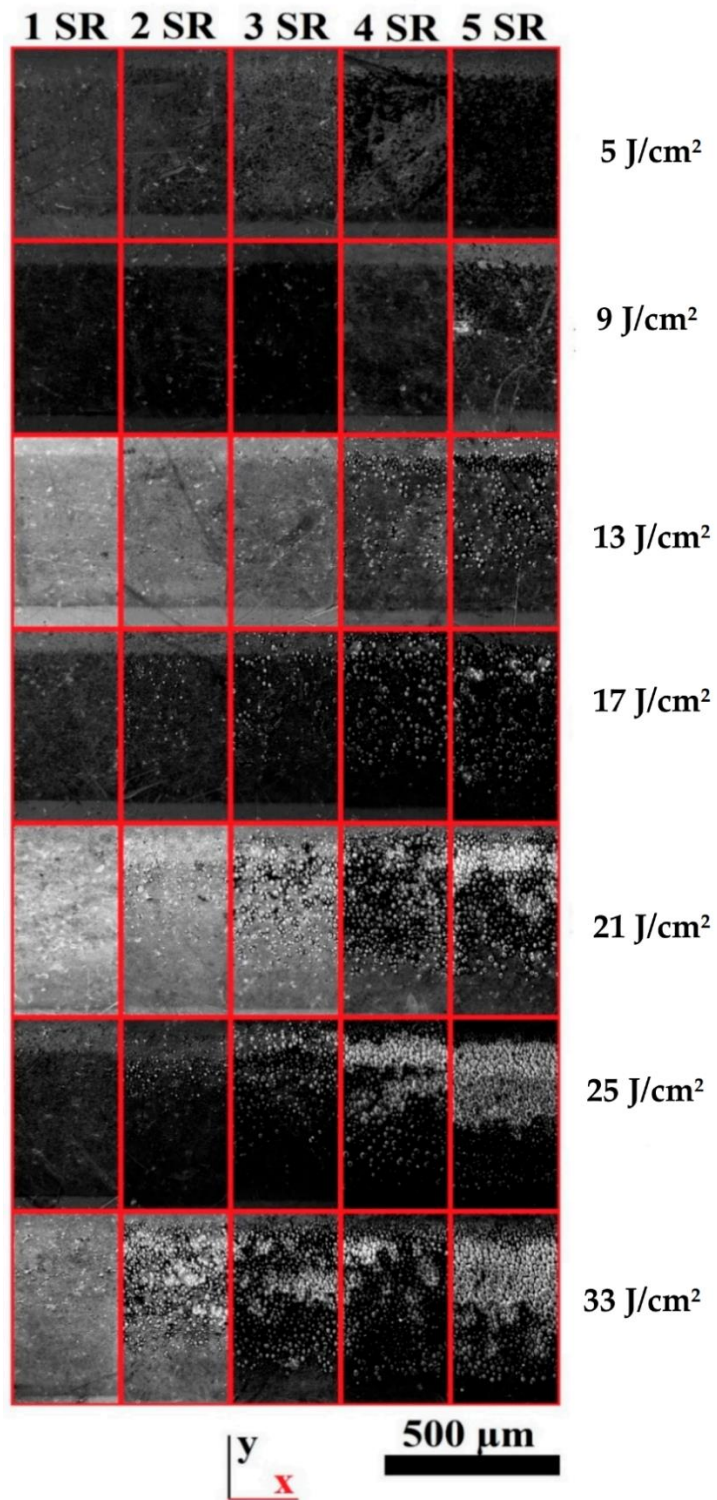


Figure 19 SEM images showing appearance of ablated areas (top view).

Treated areas appear darker than the untreated alloy surface. SEM images reveals two types of surface features formed by femtosecond laser ablation — i) periodic ripples (LIPSS) resolvable at higher magnifications and ii) rough/bright grainy clusters consisting of conical microstructures.

Both types of features may be simultaneously present in the treated area; however, generally the conical microstructures are characteristic of higher beam energy fluence and higher number of scan repetitions. The portion of conical microstructures in the treated area is always greater at higher values of the y coordinate, that is, for the last scan tracks, which strongly correlates with the data for treated area profiles. Individual cones appear relatively randomly over the surface of treated areas at low energy fluence and the smaller number of scan repetitions, but they are more frequent at larger y values. It is also worth noting that any observations of conical microstructures start with at least 2 scan repetitions.

It appears reasonable that in this case the main mechanism triggering the formation of conical microstructures is the re-deposition of ablated debris. Such debris smear the previously clear, and therefore highly reflective, surface and facilitate more efficient absorption of energy. It is plausible that to some extent this additional absorption of energy is promoted by plasmonic effects [59]. In this way, the ablation of material on subsequently irradiated spots is increased due to debris from earlier laser scanning of neighboring areas. This may cause a positive feedback effect takes place when the re-deposition of material from previous tracks enhances the ablation at the current track, and then re-deposition onto the next track.

As would be expected for ultrashort pulse treatment of this metal alloy, at low energy fluence LIPSS (Figure 20a,b) were observed. The LIPSS period for this area is equal to $0.78 \pm 0.13 \mu\text{m}$, showing no observable dependence on energy fluence and scan repetitions within the range of parameters that was considered. A granular structure of the ripples is visible at high magnification (Figure 20b). It is possible that these granules are a result of the re-deposition process. Some of them may play a role as precursors for growth of conical microstructures during later repetitions of the scanning pattern in the ongoing laser treatment.

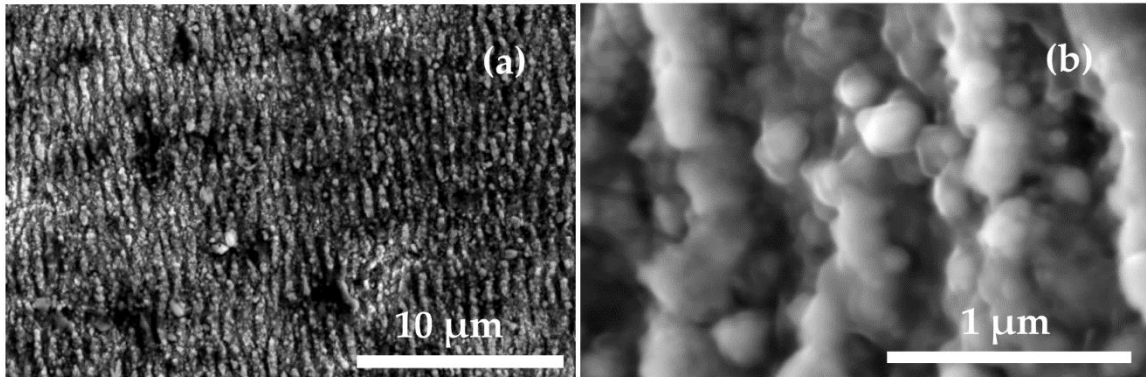


Figure 20 SEM images corresponding to an energy fluence of 9 J/cm^2 and five scan repetitions. (a) SEM image demonstrating semi regular LIPSS; (b) SEM close-up on LIPSS features, revealing a granular structure (observed at a 52° sample tilt).

2.4.4 FIB-SEM and EDX examination of internal composition of conical microstructures

Higher energy fluence and number of pulses leads to the emergence and growth of conical microstructure clusters, which overshadow LIPSS features in the irradiated area. With the increase of pulse energies and numbers of repetitions, the conical microstructures cover an larger portion of the treated area. Moreover, SEM imaging of

the conical microstructures indicates that the increase of energy fluence and number of pulses tends to enhance the aspect ratio of a single cone. For example, for the twice-repeated 21 J/cm^2 energy fluence laser treatment, the conical microstructures are represented by $2.5\text{--}3 \text{ }\mu\text{m}$ high and less than $10 \text{ }\mu\text{m}$ wide cones, whereas for the 33 J/cm^2 energy fluence and five repetitions, cones reach a height of $30 \text{ }\mu\text{m}$ and a width of $20\text{--}25 \text{ }\mu\text{m}$ (Figure 21a). A pattern of periodic features is observable on the slopes of some conical structures (Figure 21b), possibly associated with LIPSS.

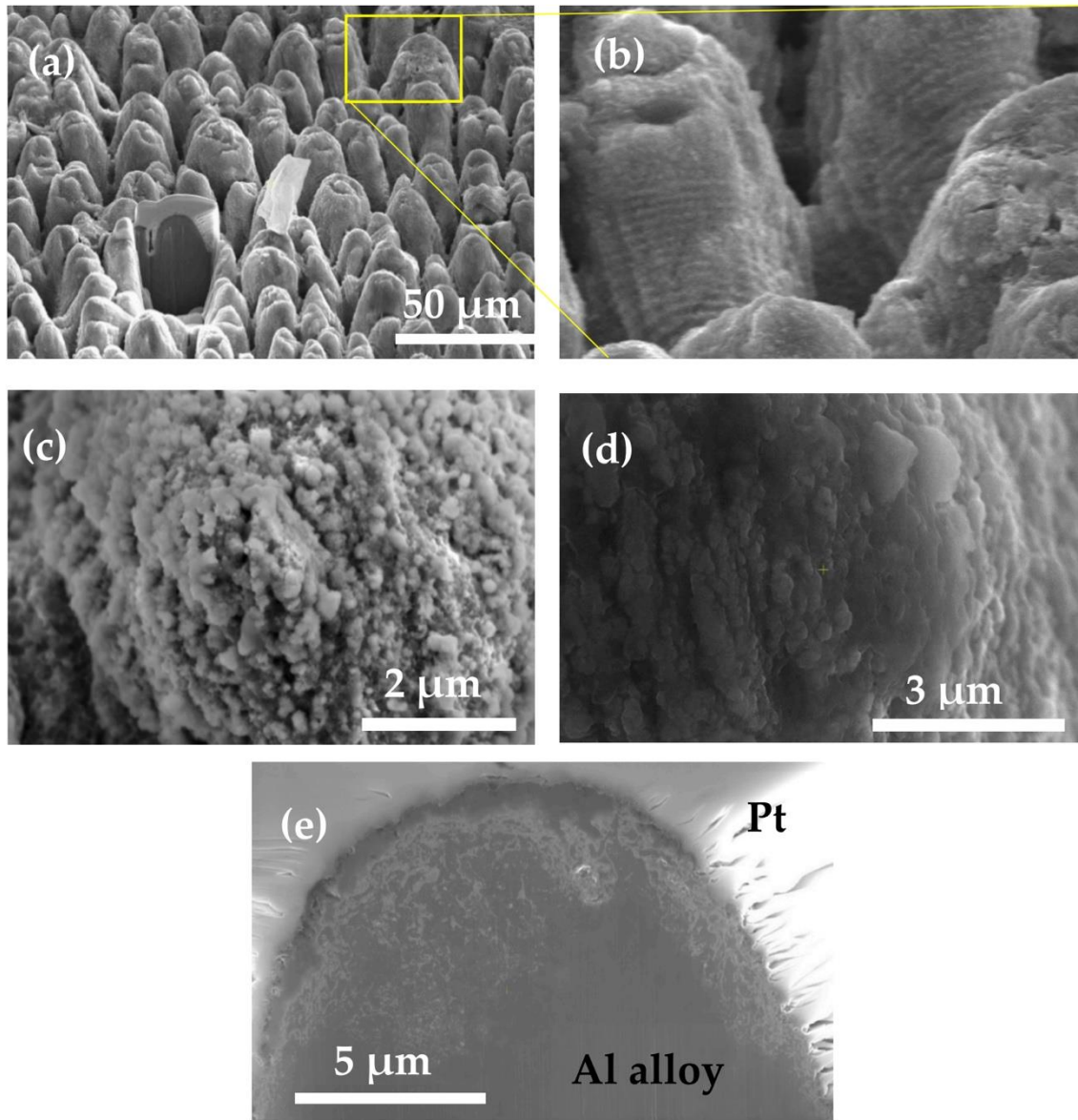


Figure 21 SEM images of conical microstructures corresponding to an energy fluence of 33 J/cm^2 and five scan repetitions: (a) conical microstructures (observed at a 52° sample tilt) with an impurity particle and the site of FIB milling; (b) close-up of the conical structures' slopes with the contrast enhanced, ripples are observable (observed with 52° sample tilt); (c) tip of a conical microstructure before cleaning in acetone; (d) slope of a

conical microstructure after cleaning in acetone; (e) internal content of a conical structure sectioned in half by FIB (observed with 52° sample tilt), a protective layer of platinum is deposited on top.

A cross section of a cone, which was observed using an energy fluence of 33 J/cm² and five scan repetitions was obtained using focused ion beam (FIB). The cross section reveals that the elemental composition and uniformity of the cone tip is different from that of the bulk of the alloy (Figure 21e). A comparison between SEM images acquired before and after cleaning in an ultrasonic bath in acetone and isopropanol is shown in Figure 21c,d. Sonication removed some of the loose nanoparticles that were lodged on the slopes; however, the surface of the conical structures is still very rough even after the cleaning. It seems possible that small ablated particles which have been redeposited during the initial repetitions of the scanning pattern, have been incorporated within the conical structure, while others that were produced at a later stage remained loose enough to be removed by ultrasonic cleaning.

Similar observations on the formation of conical microstructures were reported by Zuhlke et al. [94] in detail. Ablated nanoparticles redeposit outside the irradiated spot, and later, when the scanning beam reaches them again, a portion of the nanoparticles melts. This forms a structure with alternating layers of melted and non-melted particles [94]. A further investigation using EDX was undertaken on the dissected conical microstructures to examine how the re-deposition of ablated particles disrupts a uniform elemental content.

The internal structure of the cone, formed using the conditions that were indicated earlier, was investigated by FIB cross sectional cutting.

A protective Pt layer was applied to avoid curtaining defects. The section (Figure 22a) was analyzed by EDX (Figure 22b–d), then a thin lamella was cut out for higher resolution SEM (Figure 22e) and EDX (Figure 22f–h) imaging.

Several notable anomalies highlighting possible elemental segregation can be observed within the cut.

A distinct area of stronger oxidation is marked with a red oval (Figure 22a–c) with a brighter SEM signal and a reduced Al EDX signal has been observed in the cross section.

Other remarkable features can be seen in the thin lamella imaged using SEM and EDX (Figure 22e–h), such as internal voids (marked with yellow and white ovals) and a Cu-rich area (marked with a black oval) The voids appear to produce a strong aluminum signal due to the aluminum background inherent in the setup used for this investigation.

The fact that a thick layer on the tips of the conical structures is significantly oxidized and contains areas that are Cu-rich or Cu-poor could be significant for the understanding of the laser-treatment's effect on corrosion resistance. The conical surface topography by itself may result in a more hydrophobic surface that reduces the material's exposure to moisture [96] (and therefore reduces corrosion), confining it to the tips of the conical structures. Here, the inhomogeneity of the elemental content of the surface layer of the conical microstructures may play a significant role on the propagation of corrosive pits [200].

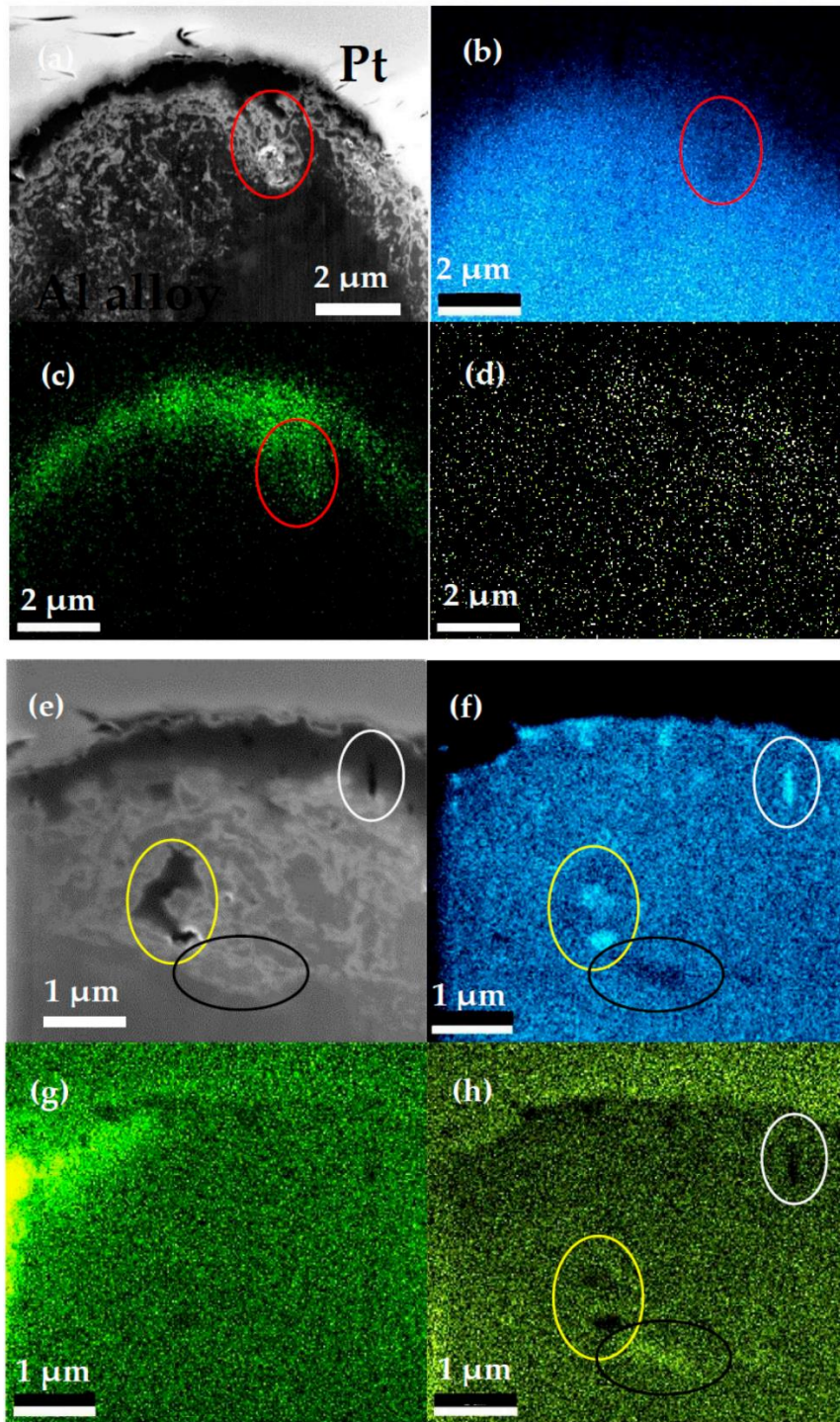


Figure 22 FIB sectioning of a cone formed by laser ablation treatment at 33 J/cm^2 with five scan repetitions: (a) SEM image of FIB-cut conical structure; (b) EDX showing Al

concentration inside the FIB-cut conical structure; (c) EDX showing O concentration inside the FIB-cut conical structure; (d) EDX showing Cu concentration inside the FIB-cut conical structure; (e) SEM image of lamella cut from the conical structure; (f) EDX showing Al concentration inside the lamella cut from the conical structure; (g) EDX showing O concentration inside the lamella cut from the conical structure; (h) EDX showing Cu concentration inside the lamella cut from the conical structure. Contrast is enhanced for all images.

2.4.5 Study of optical properties of ablated areas

D16T that is ablated to the point of conical structure growth has been demonstrated to be a broadband absorber [126]. The low reflectivity of the laser irradiated area can be indeed readily observed with the naked eye, (Figure 15a). The reduction of reflectivity was evaluated by an integrating sphere measurement. The sphere PVE300 Photovoltaic Device Characterization System (Bentham Instruments, Reading, UK) was used to estimate the reflectivity of the laser treated surface in a spectral range of 300–900 nm.

Signal was collected from a spot of 1 mm diameter that was obviously bigger than the width of the treated area; therefore, the signal was collected from both the treated area and the surrounding untreated surface. Due to technical constraints, a wider area could not be treated with femtosecond pulse irradiation; therefore, the reflectivity was qualitatively estimated by applying the linear rule of mixture to the contributions of treated and untreated areas. The untreated alloy's surface showed a reflectivity of $79 \pm$

5% in the visible light (300–900 nm) wavelength range, whereas the spot that was positioned in the center of the laser-treated area illuminating both the laser-treated area and the untreated surrounding alloy had an integral reflectivity of $42 \pm 2\%$ within the same wavelength range. The rough estimate of the reflectivity of the treated area was measured to be $21 \pm 2\%$.

2.4.6 Concluding remarks

A slope of the ablated pit and uneven roughness of the laser irradiated areas were observed and attributed re-deposition of ablated material. The re-deposited material causes an increase of absorption of the laser radiation, thus modifying the ablation rate locally. Moreover, this effect increases the probability of forming conical microstructures, since the redeposited nanoparticles instigate non-uniform ablation resulting in a positive feedback for the growth of conical structures in a self-enhancing process. Thus, conical structures starting to grow earlier at the edge of the treated area will have a higher aspect ratio, leading to non-uniform roughness.

An investigation of the internal structure of the tip of such a conical microstructure, grown by re-deposition of ablated material of the alloy, was conducted using FIB milling. EDX data reveals oxidation of irradiated areas as deep as $3 \mu\text{m}$ inside the conical microstructures (Figure 22c). Areas of increased content of O and Cu are observed along with the respective depletion of Al concentration (Figure 22b,f), and vice versa. The inhomogeneous distribution of O, Cu, and Al and the stain-like patterns observed inside the tip can be explained by melting (and incorporation) of redeposited nanoparticles occurring during each scanning repetition.

The distribution of impurities in surfaces of metals such Al has been observed to affect the propagation of corrosive pits [200]. Such investigation is therefore relevant in the study of corrosive properties of Al alloys surfaces modified by femtosecond pulse ablation.

Chapter 3. Laser-assisted production of nanostructured 2D-TMDCs

3.1 Individual contributions

The current chapter is based predominantly on the published article [201] which is dedicated to submicron structuring of MoS₂ occurring simultaneously with laser synthesis, where Salimon I. A. is the primary author. This paper contains references to related article [165].

Salimon I. A. undertook to investigate the phenomenon of LIPSS in the synthesis of MoS₂, performing a parametric study of the laser synthesis. This entailed the preparation of spincoated films, operation of laser writing setup and the majority of characterization of obtained samples, all performed by Salimon I. A.

The device fabrication and characterization was performed by Zharkova E. V with assistance from Salimon I. on various imaging tasks. Salimon I performed data analysis with assistance from Zharkova E. V. and Omara A.A. Averchenko A. V. provided valuable support in operating the laser writing setup. Some SEM images (Figure 24 a,b, Figure 26) were produced by Somov P. under instructions by Salimon I. A.

3.2 Chapter summary

In this chapter, we present direct laser synthesis of periodically nanostructured 2D transition metal dichalcogenide (TMDC) films (mainly MoS₂), from a single source precursor film, deposited on Si/SiO₂ substrate. Synthesis of TMDC films (MoS₂ and WS₂) occurs within the laser irradiated tracks by local thermal dissociation of ammonium tetrathiomolybdate or tetrathiotungstate ((NH₄)₂MoS₄ or (NH₄)₂WS₄), which is caused

by the absorption of continuous wave (c.w.) visible laser radiation. LIPSS nanopatterning has been observed in the synthesis of both MoS₂ and WS₂, which is not surprise given the universal nature of the effect. Here we will be presenting primarily results that correspond to MoS₂, which was studied in more detail. LIPSS production on WS₂ was more restricted and in general exhibited lower levels of topography modulation, probably due to a lower absorption of the laser radiation that was used in our experiments by the precursor film.

We have observed occurrence of 1D and 2D spontaneous periodic modulation in the thickness of the laser-synthesized TMDC films, which in some cases is so extreme that it results in the formation of isolated nanoribbons with a width of ~ 200 nm or less and a length of several micrometers. These nanostructures fit the description attributed to the effect known as LIPSS which is frequently observed in laser-matter interaction experiments [52].

Finally, we have fabricated two terminal photoconductive detectors based on both nanostructured and continuous films for comparison purposes. The nanostructured TMDC films exhibit enhanced photo-response, with photocurrent yield three orders of magnitude higher as compared to their continuous counterparts.

3.3 Laser irradiation parameters

In the experiments that are presented here, the laser intensity (defined as average intensity in the beam spot) was within the range of 0.51 – 1.21 MW/cm² while the

scanning speed (the linear velocity of the translation stage) was within the range of 1–20 mm/s. The laser irradiation process took place in ambient conditions. The parameters of laser synthesis for the samples used in the figures are given in Table 3.

Table 3. Laser scanning parameters used for TMDC precursor film irradiation.

Figure	Liquid precursor concentration, mM	Laser intensity, MW/cm²	Scanning speed, mm/s	Comments
Figure 23	24	0.83	2	
Figure 24a	24	0.89	9	
Figure 24b	24	0.89	10	
Figure 24c	24	0.89	10	Scanning performed with parallel beam polarization
Figure 24d	48	0.89	19.5	
Figure 25a	100	0.64	9	
Figure 26	24	0.89	10	
Figure 27	24	0.89	16	
Figure 28	24	varies	19.5	Intensity is provided on Figure 28
Figure 29	24	varies	19.5	Intensity is provided on Figure 29
Figure 30a	48	0.51	19.5	

Figure 30b	48	0.64	19.5	
Figure 30c	48	0.76	19.5	
Figure 30d	48	0.89	19.5	
Figure 32	40	0.95	10	
Figure 33	48	varies	19.5	Different substrates were used
Figure 34	no precursor film	5.73	19.5	
Figure 35	24	0.95	4	
Figure 36	24	0.95	16	

3.4 Parametric study of LIPSS formation

3.4.1 Laser-irradiated track morphology

Direct laser synthesis of MoS₂ produces thin film tracks with a topography that is associated with the irradiating laser beam intensity profile at focus. This is due to the variable temperature profile, which is in turn caused by the laser intensity variation within the beam spot. In the experiments described here, the laser beam ($\lambda = 532$ nm) had a Gaussian intensity profile. This resulted in films with a profile of varying thickness in the direction perpendicular to scanning direction. The profile of a laser-irradiated track after developing had an “M” letter shape, shown in Figure 23, an AFM image of a single MoS₂ track. The thinnest part of the film at the center of the track was confirmed by Raman spectroscopy to consist of MoS₂

The reason behind the tracks having that particular profile is due to how the laser irradiation affects the precursor film.

In the center of the track, the local laser intensity is at maximum. This leads to a loss of volume due to the decomposition of the $(\text{NH}_4)_2\text{MoS}_4$, in which nitrogen, hydrogen and excess sulfur evaporate. Additionally, the already synthesized MoS_2 is further laser thinned via sublimation [202] to a thickness that depends on the parameters of the laser scanning process. At intensities of 1 MW/cm^2 and higher, the film in the center of the track is removed entirely.

When moving away from the center of the track, the thickness of the film first increases, then goes down and is reduced to zero (absence of film on the exposed substrate). The thickest parts of the laser-irradiated and then developed track are the elevated “wings” on both sides. These parts are not entirely converted to MoS_2 , but are still made significantly more resistant to developing in organic solvents. It is probable that $(\text{NH}_4)_2\text{MoS}_4$ here is converted to MoS_3 , which is another result of thermochemical decomposition of the same precursor at lower temperatures [203]. Finally, far away from the center of the track the laser irradiation has a low intensity that has a low impact on the $(\text{NH}_4)_2\text{MoS}_4$ film, and after developing $(\text{NH}_4)_2\text{MoS}_4$ is dissolved.

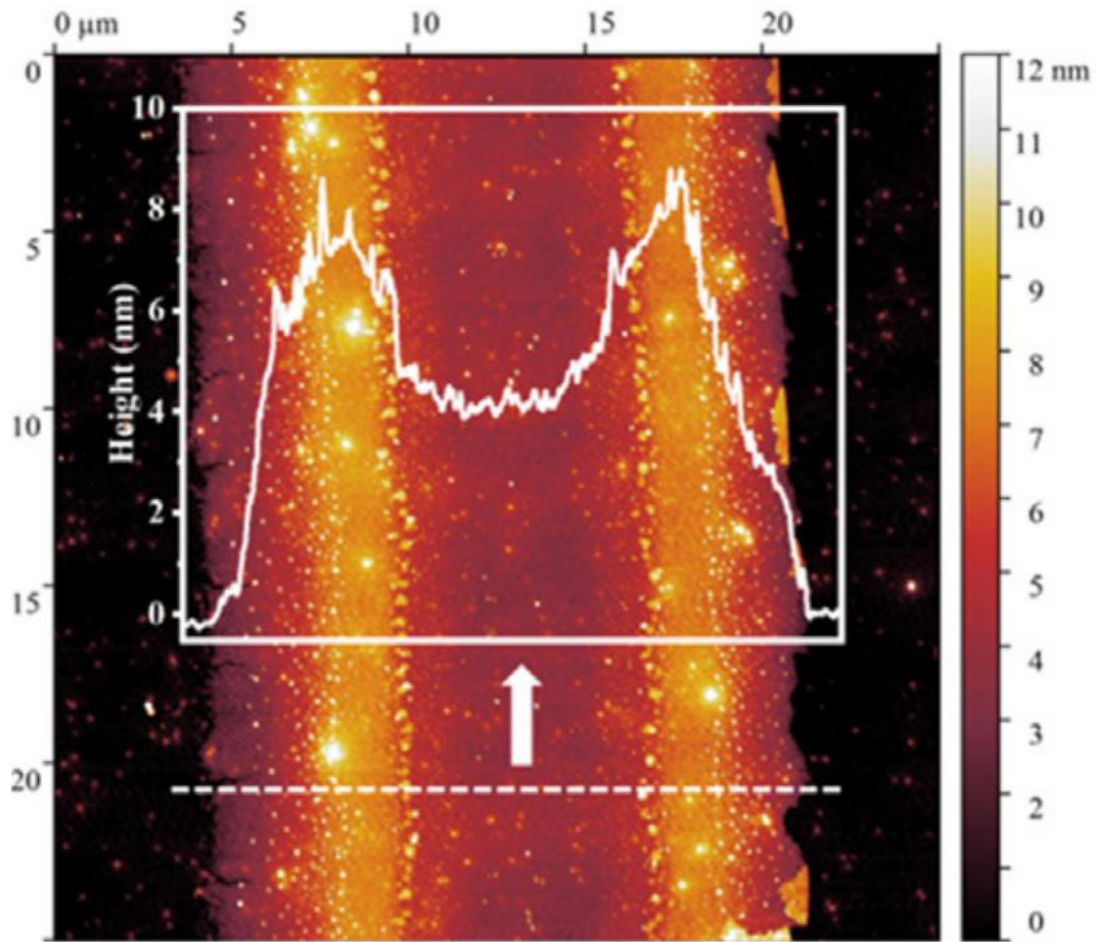


Figure 23 AFM image corresponding to a section of a single laser-irradiated track, the overlay shows the thickness profile of the track along the dash line [165] .

We have observed the 1D LIPSS features to be exclusively associated with the central region of the track (that corresponds to the peak of the laser beam intensity), while 2D LIPSS could escape this center region and propagate along the whole width of the track. Figure 24 shows scanning electron microscopy images of a continuous MoS_2 track (Figure 24a) and one with periodically modulated thickness (Figure 24b). Both tracks

were produced on the same sample using the same precursor film by merely varying the laser scanning speed. The polarization of the beam was the same in both cases, as indicated by the white arrows.

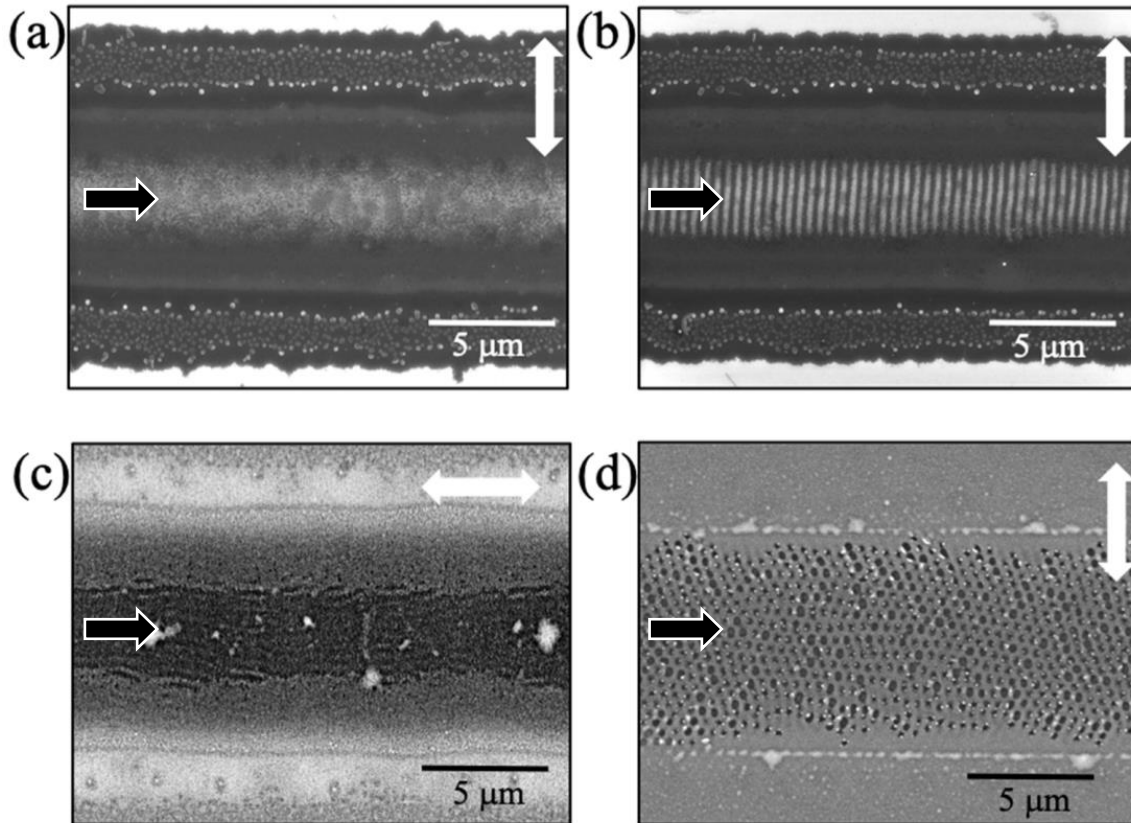


Figure 24 SEM images showing (a) continuous MoS_2 film; (b) film with periodically modulated thickness (1D LIPSS); (c) 1D LIPSS formed with beam polarization oriented along the direction of scanning; and (d) 2D LIPSS. The laser scanning direction is indicated by the white outline arrow, while the solid white double arrowhead lines indicate the polarization of the irradiating beam. The track runs along the horizontal direction corresponding to a section of a single laser-irradiated track, the overlay shows the thickness profile of the track along the dash line.

When the beam polarization was rotated by 90 degrees, the LIPSS features followed the direction of the polarization (Figure 24c). Finally, at certain conditions of irradiation, as will be discussed in more detail later, 2D LIPSS features were observed (Figure 24d). The occurrence of 1D and 2D (or both) LIPSS features appears to depend on the thickness of the precursor film, which is determined by the concentration of the precursor in the initial solution. At low concentrations (24 and 32 mM), only 1D LIPSS were observed. At a $(\text{NH}_4)_2\text{MoS}_4$ precursor concentration of 40 mM, it was possible to observe both 1D and 2D patterns. For 48 mM, only 2D LIPSS could be observed. For intermediate precursor solution concentrations, where both 1D and 2D features are possible, it was observed that at lower scanning speeds (between 2 and 6 mm/s) only 1D LIPSSs were formed, while for speeds above 16 mm/s only 2D LIPSSs were formed. For the speeds in between, fluctuations in the film could cause random switching between the 1D and 2D patterns.

Besides MoS_2 , a similar effect was also observed on WS_2 . However, the periodic modulation observed on WS_2 was less severe, making formation of separate nanoribbons on WS_2 a less appealing route for further study of periodic modulation. Tracks of WS_2 containing LIPSS can be observed on Figure 25a.

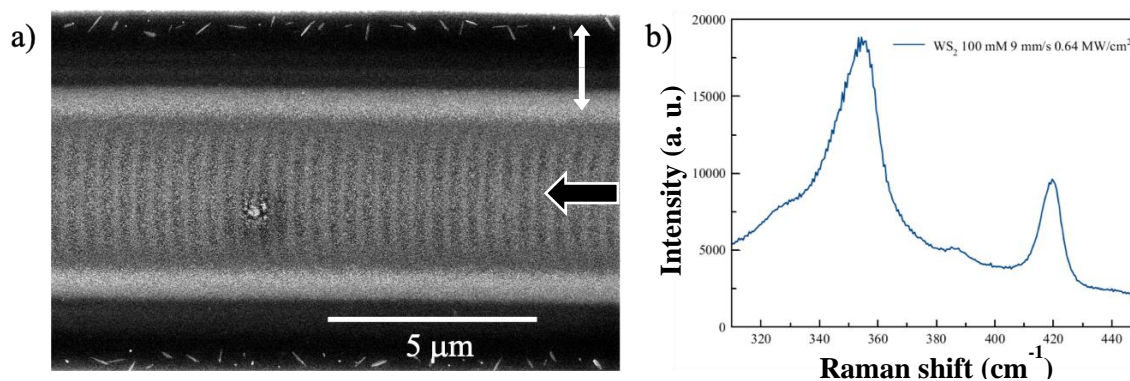


Figure 25 a) SEM image of LIPSS formation in a laser synthesized WS₂ track, b) corresponding Raman spectrum showing the in- and out- of plane vibrational modes, typical for WS₂. The laser scanning direction is indicated by the white outline arrow, while the solid white double arrowhead lines indicate the polarization of the irradiating beam.

3.4.2 Linear 1D LIPSS and formation of nanoribbons

As shown in the SEM image of Figure 24b, the regular patterns that were formed at lower precursor solution concentrations consist of linear gratings with a period of 423 ± 9 nm. AFM scans revealed that the periodic features correspond to a modulation of the film's thickness.

This period corresponds to low spatial frequency LIPSS [52], and the orientation of the periodic features is along with the direction of the polarization of the irradiating laser beam. These features (except the 2D arrays on Figure 24d) fit the description of LSFL-II. This observation is consistent with the observations in 2.3 *Localized laser*

oxidation of GaAs crystals. In both cases c.w. irradiation was used and feedback from already induced structures promotes the features that are directed perpendicular to the track.

The polarization was chosen to be perpendicular to the scan direction, except for when stated otherwise (Figure 24c). It can be observed that in the case where the periodic features form perpendicular to the track (as in Figure 24b), the pattern is significantly more regular. In the case where the polarization of the scanning beam was parallel to the track direction, the regularity of the observed 1D linear LIPSS was lower (Figure 24c). Nevertheless, in both cases the period is essentially the same, ~ 422 nm. The qualitative difference is attributed to more efficient optical feedback in the case of scanning perpendicular to polarization.

Previous reports, dedicated to laser writing synthesis of TMDCs [11, 165], remarked that a laser thinning process regulates the final thickness of homogeneous TMDC film. At the higher extreme of beam intensities, which have been used in our experiments, the film at the center of the laser-irradiated track appears to be completely removed.

Spatially selective laser thinning could reasonably lead to the formation of separate ribbons in MoS₂ and milder modulation observed in WS₂, as has been observed in our experiments. A periodic variation in the intensity of the absorbed irradiation, caused by complex optical feedback, could result in a periodic variation of film thickness. However, if the peaks of intensity are sufficient to remove partially or completely areas

of the films via laser thinning, it would result in the formation of isolated TMDC nanoribbons.

Here, the term nanoribbons is used due to the small thickness (less than 20 nm) of the obtained structures that have a ribbon-like shape. The width of these ribbons ranges from ~ 200 to ~ 115 nm. These ribbons are also tightly packed, being repeatedly induced with a ~ 422 nm period, which results in a high proportion of edge length to surface area. This in turn has a significant effect on the properties of the synthesized material, namely photoconductivity, which is demonstrated and discussed in detail below.

It can be confirmed that the nanoribbons are separated by gaps of exposed (Figure 26) or partially exposed (Figure 27) substrate; that is evidenced by observations of laser-irradiated tracks developed in the coarser DMF solvent. When using this solvent for developing instead of the milder NMP solvent, large sections of the laser-irradiated track delaminated from the substrate. For example, on Figure 26 a part of a side-lobe has detached from the substrate. To confirm and illustrate the notion that separate nanoribbons divided by gaps of exposed substrate are formed, the coarser DMF solvent was used, causing large sections of the laser-irradiated tracks to delaminate from the substrate. MoS₂ ribbons detaching and bending.

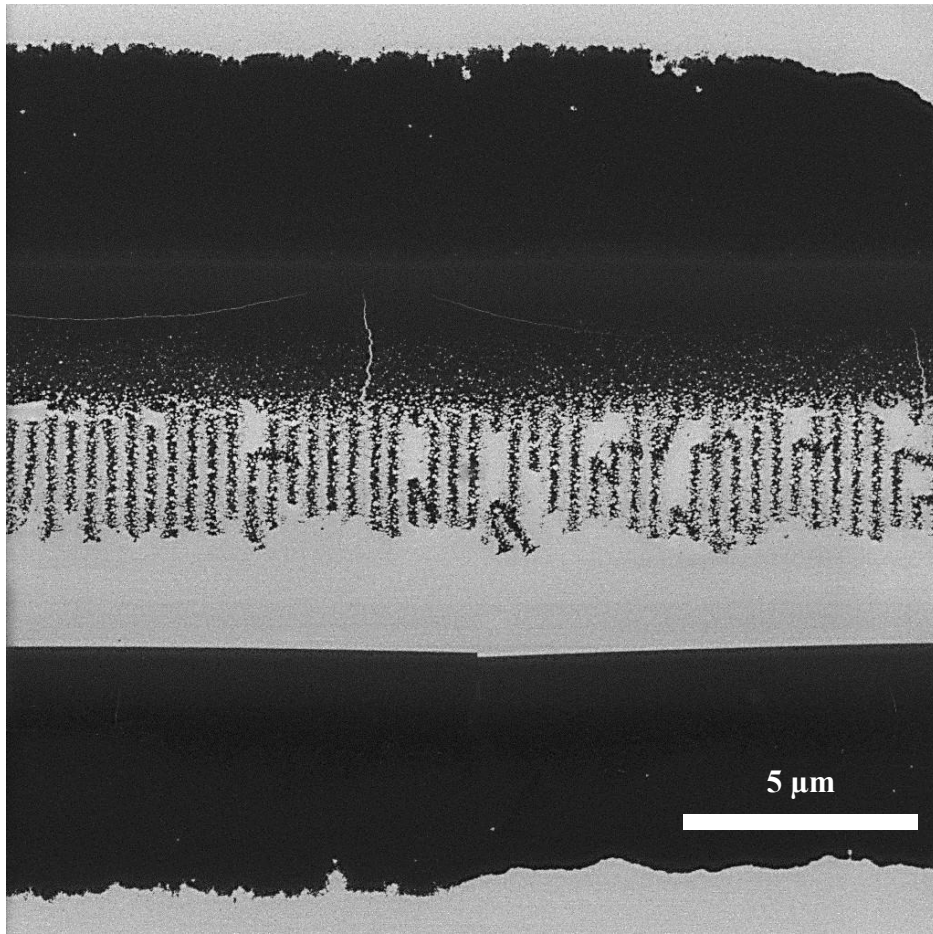


Figure 26 SEM images showing an over-developed track with one side-lobe (bottom part of the image) partially detached from the substrate, leading to detachment and bending of nanoribbons. SEM images produced by Somov P.

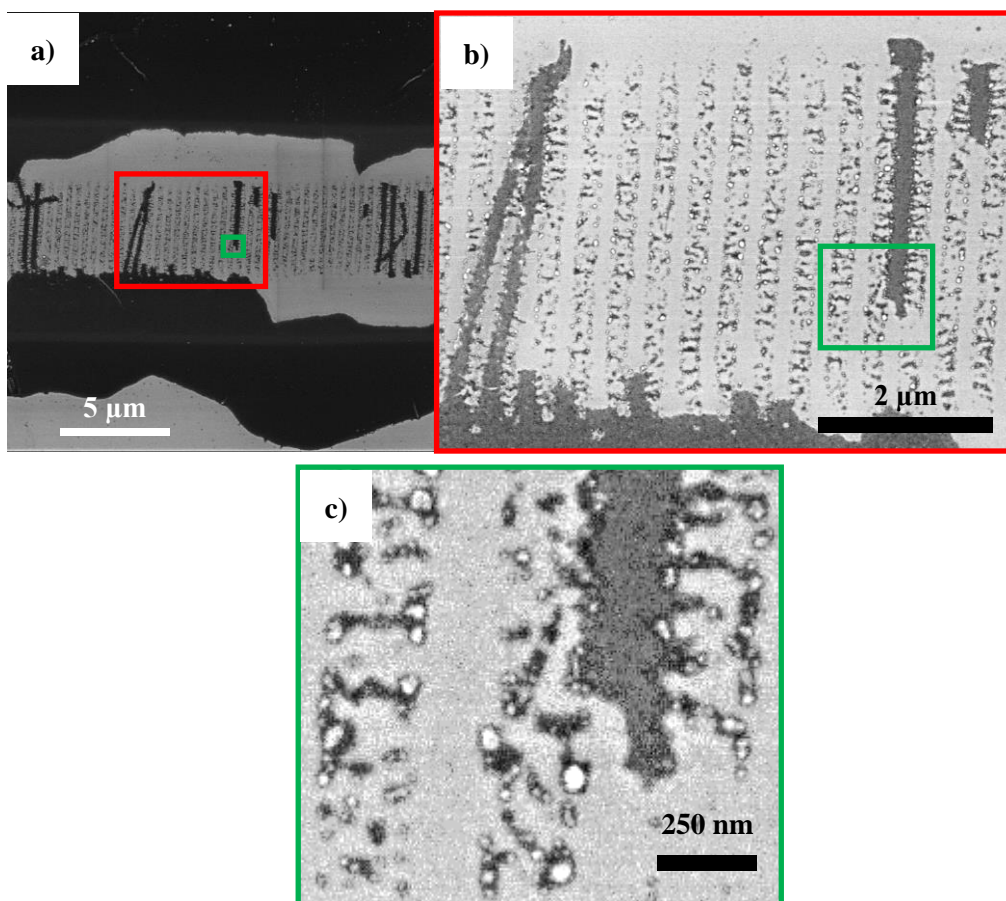


Figure 27 Series of SEM close-ups showing an over-developed track with one side-lobe (bottom part of the image) partially detached from the substrate, leading to detachment of nanoribbons. Smaller irregular structures were observed between the periodic nanoribbons. SEM images produced by Somov P.

For the intensity of 0.89 MW/cm^2 , the ribbons are relatively wide and the gaps between them relatively narrow; for a scanning speed of 16 mm/s , the gaps between nanoribbons appear to contain irregular structures of even smaller dimensions (Figure 27). Some of those are isolated, while others are physically connected to one or both of the larger ribbons. Those smaller structures are typically about $\sim 50 \text{ nm}$ wide. As they

appear to be randomly distributed and do not exhibit well-defined periodicity, we do not associate these smaller features with high spatial frequency LIPSS [204, 205].

It can be observed how the increase of laser power causes the ribbons of remaining MoS₂ film to shrink and gaps between them to grow wider (Figure 28). The width of the observed ribbons ranged between ~ 200 nm and ~ 115 nm (Figure 29). Additionally, with an increase of power the LIPSS ribbons grow longer due to the Gaussian distribution of beam intensity. At a certain intensity, the ribbons break in the middle (Figure 28d).

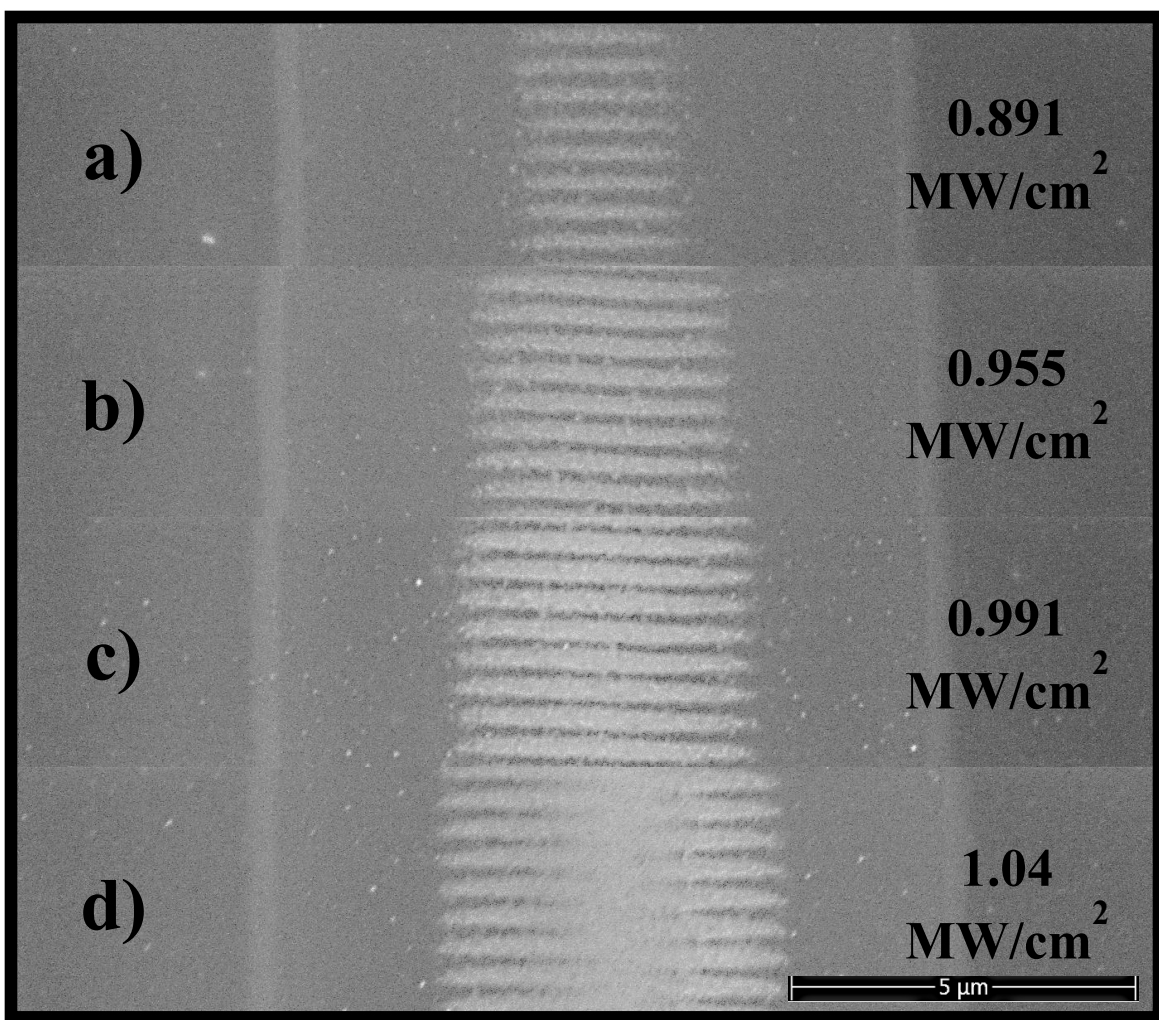


Figure 28 SEM images of laser-irradiated tracks showcasing 1D LIPSS length and width depending on laser beam intensity.

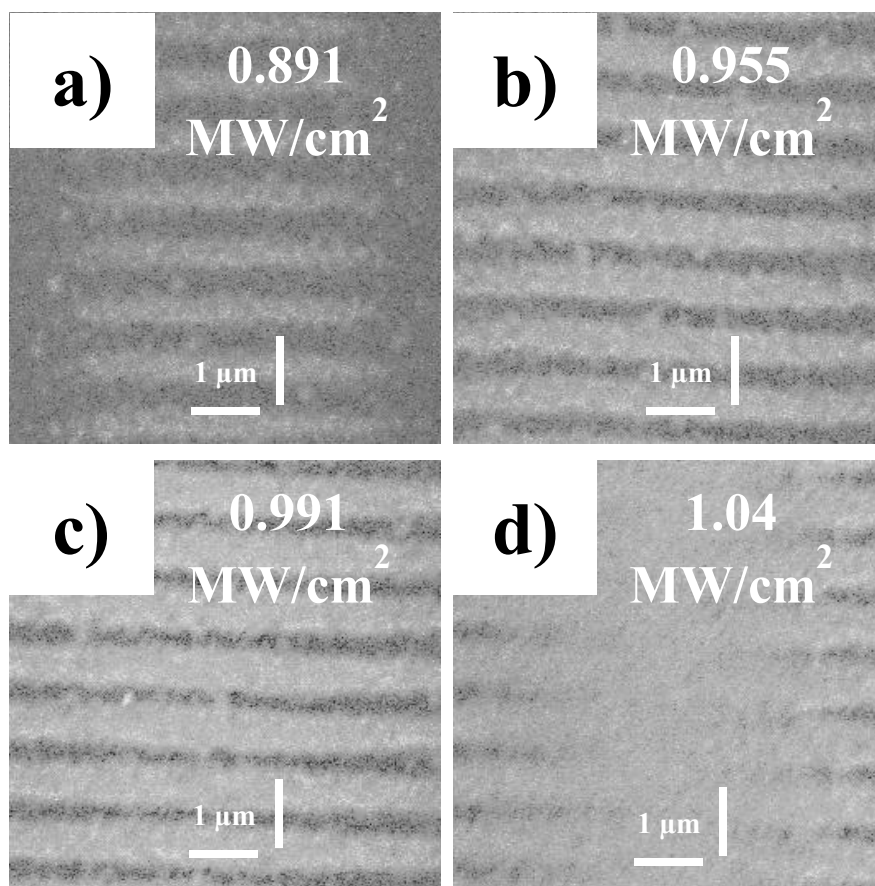


Figure 29 Close-up SEM images of laser-irradiated tracks showcasing 1D LIPSS length and width depending on laser beam intensity

3.4.3 2D LIPSS

As mentioned above, when more concentrated (40 mM and 48 mM) precursor solutions are used, 2D LIPSS features start to emerge. Figure 30 presents an overview of 2D LIPSS patterns that have been produced using the same scanning speed, but different laser peak intensities.

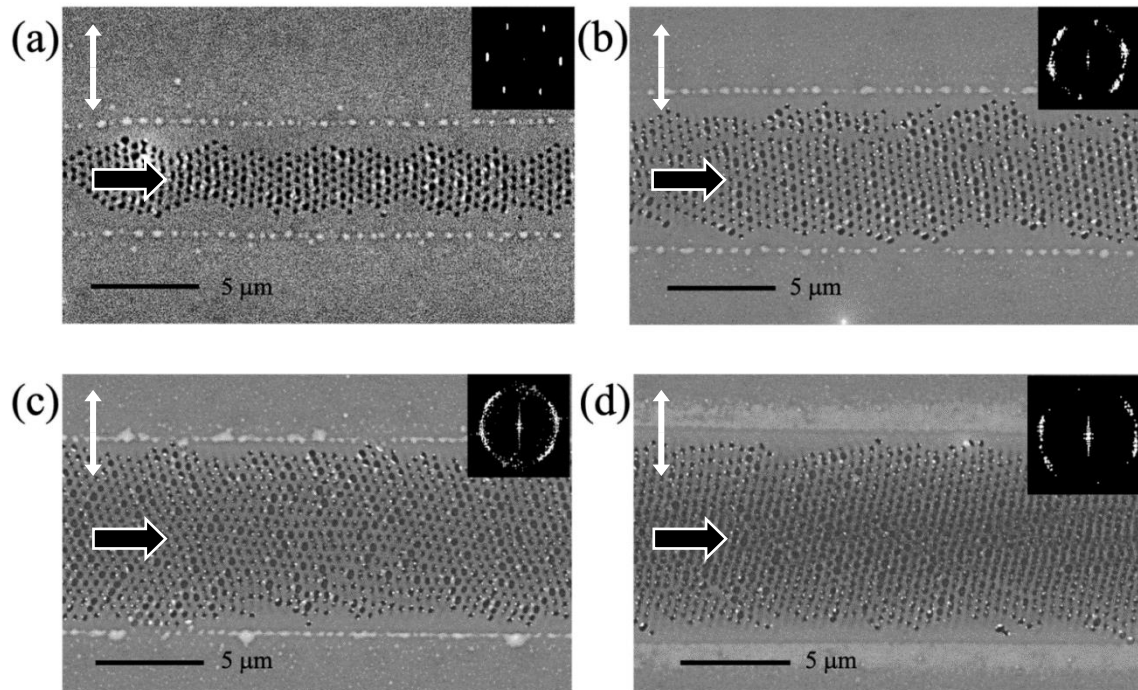


Figure 30 SEM images of 2D LIPSS structures produced using the irradiating laser intensities of (a) 0.51 MW/cm^2 , (b) 0.64 MW/cm^2 , (c) 0.76 MW/cm^2 , and (d) 0.89 MW/cm^2 . The laser scanning direction is indicated by the white outline arrow, while the solid white double arrowhead lines indicate the polarization of the irradiating beam. The insets correspond to a Fourier transform of the 2D LIPSS pattern.

The width of the 2D LIPSS-covered area scales with the peak intensity value. In addition to that, the strict regularity of the 2D pattern seems to deteriorate as the intensity of the laser increases, although the separation between features seems to remain the same. This can be seen clearly in the corresponding Fourier transforms of the 2D patterns that are shown as insets in each SEM image. The distortion of the 2D pattern that occurs at higher intensities could indicate a greater sensitivity to random surface defects. Since the

formation of such LIPSS during continuous scanning is strongly dependent on positive feedback from already formed structures, it could be that wider tracks offer more opportunity for competition between various spots of LIPSS emergence. Additionally, when the film in the middle becomes thin at higher laser intensities, the two side lobes of the M-shaped track become less connected. The 2D LIPSS features on the side lobes may then decouple and instead compete in providing local feedback to the center of the track, thus making the pattern in the center of the track specifically less regular (Figure 30d)

With a narrower track that only supports 5-7 periods of LIPSS, there is less probability of encountering defects in the film that can distort the local distribution of the field. This emphasizes the feedback from the already formed structures and leads to tracks that are, on average, more regular.

3.4.4 Experiments with variable scanning speed

A parametric study was conducted to identify the irradiation conditions under which 1D and 2D LIPSSs are formed for films obtained using various precursor solution concentrations. The main parameters defining the process here were chosen to be as follows: liquid precursor solution concentration, laser beam intensity and laser scanning speed. The concentration of precursor salt in the liquid solution affects the viscosity of the solution, which in turn determines the thickness of the spin-coated films, as mentioned in *1.3.9 Synthesis methods for 2D-TMDCs*.

Formation of LIPSS was extensively reported on thin films of metals [71] and polymers [78]. Most works that mention the production of 1D and 2D LIPSS on thin

films used pulsed irradiation and demonstrated the dependences of the obtained patterns on the number of laser pulses. Two-dimensional patterns were obtained for circular polarization [57] of the incident beam while linear polarization produced 1D patterns [78]. In the present work, c.w. irradiation with a linear polarization was used to form both 2D LIPSS and 1D LIPSS. Here, the selection between the 1D and 2D pattern depends only on the scanning speed and the thickness of the spin-coated precursor film, as defined by the concentration of $(\text{NH}_4)_2\text{MoS}_4$ in the initial solution.

To avoid making a significant multitude of tracks with fixed scanning speeds for each combination of laser intensity and precursor solution concentration, this study was conducted in the following manner: four separate samples covered with precursor films were produced, each with a different precursor solution concentration (24, 32, 40 and 48 mM). For each such sample, the same laser scanning protocol was conducted. The laser scanning produced multiple tracks with various (within the range of 0.51-1.21 MW/cm²) laser intensities; for each track, the laser intensity was fixed but the scanning speed increased linearly with time (going from 0 to 20 mm/s in 1 s). Consequently, each position along the laser-synthesized MoS₂ track (10 mm long) corresponds to a specific instant speed. The areas on the track where different types of LIPSS occur were determined and a map of the parameter space (laser intensity and scanning speed) for the formation of specific structures has been compiled. These parameter maps, corresponding to film obtained from solutions with concentrations of 24, 32, 40, and 48 mM are shown in Figure 31.

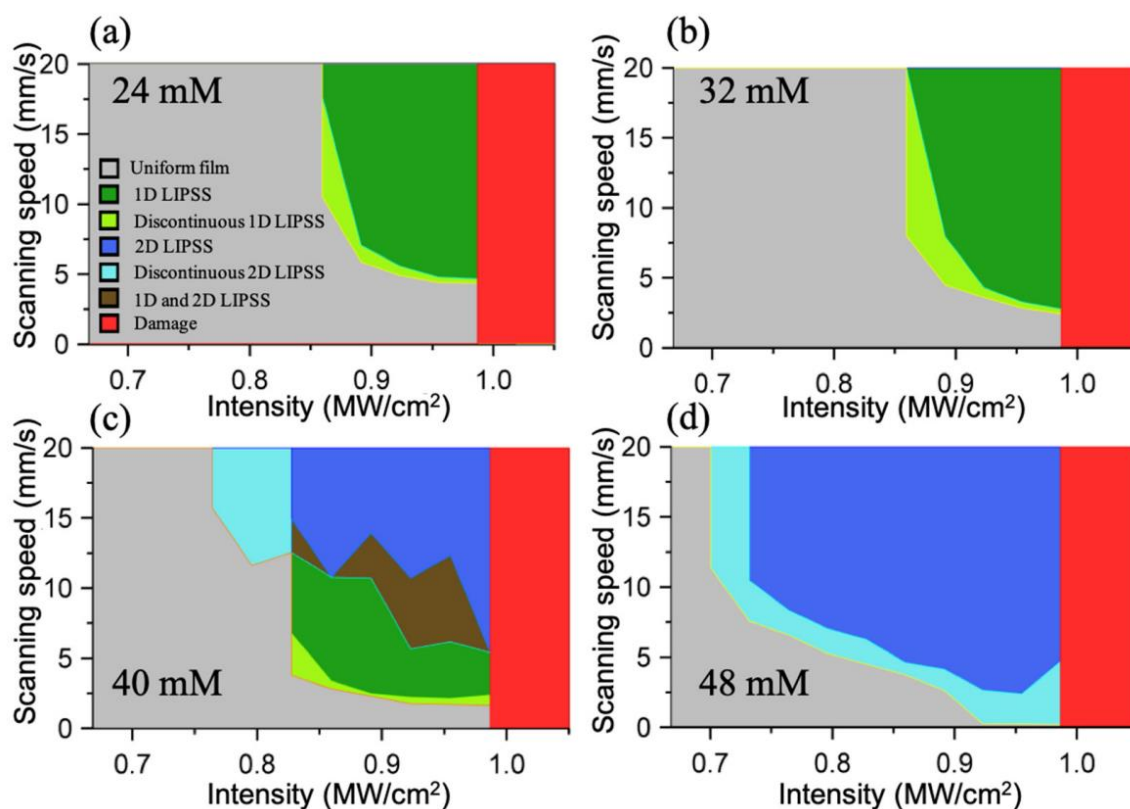


Figure 31 Parameter maps (laser intensity, scanning speed) indicating the regions where various types of LIPSS formation were observed on scanned films prepared with a) 24 mM, b) 32 mM, c) 40 mM, and d) 48 mM precursor solution concentrations. The color key for the various observations is shown as an inset on a).

Various formations are shown, including 1D-LIPSS (green region), 2D-LIPSS (dark blue region), and intermediate ranges of instability, where areas containing LIPSS features interchange with areas covered with uniform film. The parametric study suggests that LIPSS are more likely to form at high speed/high intensity combinations. A higher precursor solution concentration (corresponding to thicker precursor films) shifts the

probability for LIPSS formation to lower intensities and promotes the occurrence of 2D patterns. At the higher end of laser intensities, the film is completely removed in central region of the track (red regions of the color maps). However, periodic features can still be observed in the periphery.

It could be suggested that since in our case the irradiation used is c.w., the slow scanning leads to a slow heating of the film and allows the front of the beam to pre-heat the film, causing a chemical change that is detrimental to the chances of observing LIPSS. Indeed, our observation show that it is not possible to propagate the structuring by scanning over the elevated “wings” of an already irradiated track. When, however, the scanning speed is high, the rapid inhomogeneous heating leads to a structural change, with the self-reinforcing of the LIPSS effect outspeeding the pre-treatment of the film with the approaching beam.

Scanning electron microscopy investigation of the track topography confirmed literature reports that the LIPSS formation is greatly influenced by the features of surface topography that provides optical feedback. For example, we have observed a switch from 1D to 2D LIPSS caused by the beam encountering a defect in the laser beam path, as shown in Figure 32.

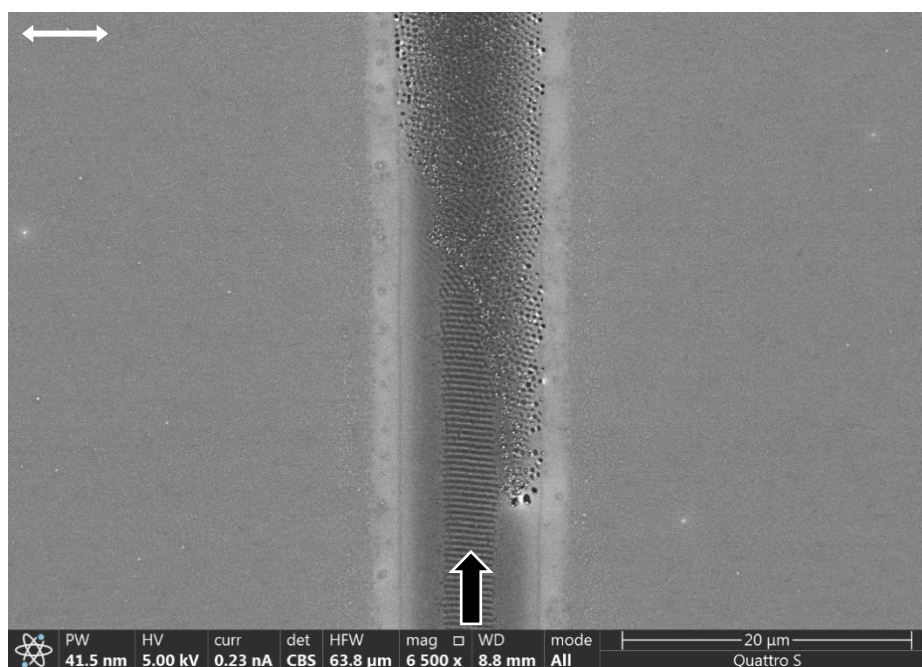


Figure 32 1D to 2D LIPSS transition caused by a defect of the film (scanning direction is from bottom to top). The laser scanning direction is indicated by the white outline arrow, while the solid white double arrowhead lines indicate the polarization of the irradiating beam.

Importantly, 2D LIPSS formations dominate in thicker films (40 and 48 mM), whereas 1D LIPSS dominate in thinner films (24 and 32 mM). Since the precursor film consists of $(\text{NH}_4)_2\text{MoS}_4$ particles, which can act as scattering centers for the incident laser beam, a reason for the selection of a particular type of LIPSS pattern could be the quantitative difference in the scattering induced in precursor films of various thicknesses. Consequently, the amount of scatterers increase with the precursor solution concentration, suggesting that scattering intensity could be a significant factor in the 1D and 2D LIPSS formation selectivity.

3.4.5 Role of SiO₂ layer in LIPSS formation.

As mentioned above, silicon wafers with a 300 nm SiO₂ layer were used throughout this study. Attempts to observe the LIPSS effect on arbitrary bulk substrates were less successful, though it is known that obtaining uniform MoS₂ films by laser writing synthesis is possible on any kind of substrate [165].

A similar parametric study was undertaken for bulk substrates such as crystalline Si wafers with no SiO₂ layer (Figure 33a,b), sapphire wafers (Figure 33c) and glass microscope slides (Figure 33d). The scanning speed was varied in the same range of 1-20 mm/s, while the range of laser intensity was selected in such a manner that it allowed to cover outcomes ranging from seemingly unaffected precursor film to complete removal of precursor film by laser thinning. The 48 mM concentration of the liquid precursor solution was selected.

While under some conditions formation of chaotic patterns was observed in the laser-irradiated tracks, bulk substrates did not exhibit repeatable formation of regular periodic LIPSS features within the range of parameters used.

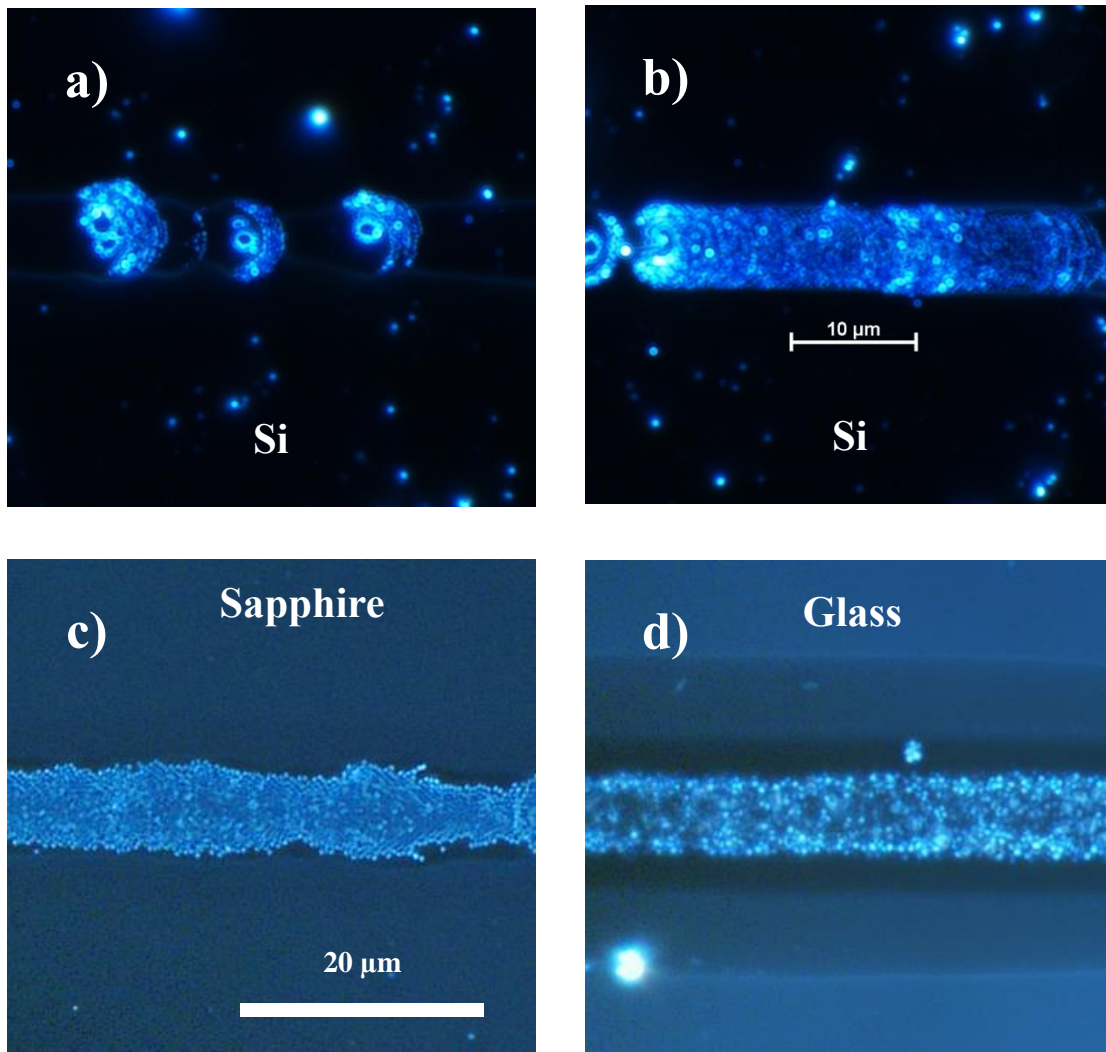


Figure 33 Features obtained on non-layered substrates: a,b) crystalline Si wafers without SiO₂ layer, c) crystalline sapphire wafers, d) glass microscope slides,.

While some hints of some periodic or quasi-periodic structures can be observed, the substrates other than the Si wafers with 300 nm SiO₂ did not exhibit a predisposition towards synthesis of MoS₂ films with well-defined periodic patterns within the range of parameters that was explored.

A possible reason for the role of the SiO₂ layer in the formation of LIPSS could be coupling of laser radiation into leaky waveguide modes that are supported by the SiO₂ layer and which interfere with the incident radiation to produce a modulation of the local laser intensity. This intensity modulation produces the observed modulation in the laser-synthesized TMD film. To verify this hypothesis, we performed scanned irradiation of the substrate (in the absence of the TMD precursor film) at much higher laser intensity levels (5.73 MW/cm²), which is sufficient to produce optical damage to the surface. We have observed a 2D periodic pattern with a period of ~ 440 nm, which is very close to the 2D LIPSS period that has been observed in the laser-synthesised TMD tracks. The 2D periodic pattern that has been directly engraved in the Si/SiO₂ substrate is shown in Figure 34.

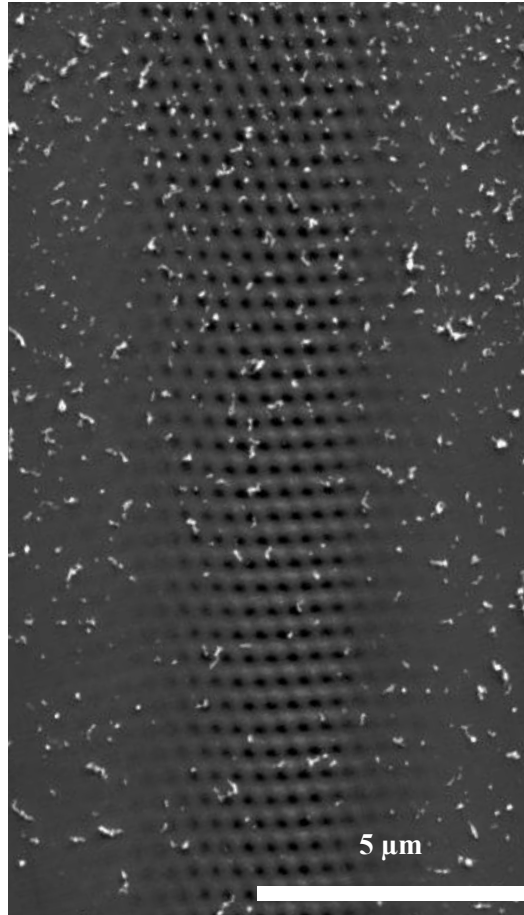


Figure 34 SEM image showing an LIPSS pattern, which is formed directly on the SiO_2 layer under intense irradiation. The surface is covered with debris, indicating the occurrence of direct optical damage, induced by the laser irradiation.

3.5 Properties of MoS₂ 1D LIPSS

3.5.1 AFM scanning

We provide AFM scans from the sample used to measure photoconductive properties of the MoS₂ nanoribbons. Like with the parametric study detailed above, the tracks were produced with a varying speed that increased with a constant acceleration of 20 mm/s². Below are the section corresponding to an area of uniform film formed with a low (~ 8 mm/s) scanning speed (Figure 35) and an area containing nanoribbons formed with a high (~ 16 mm/s) scanning speed (Figure 36).

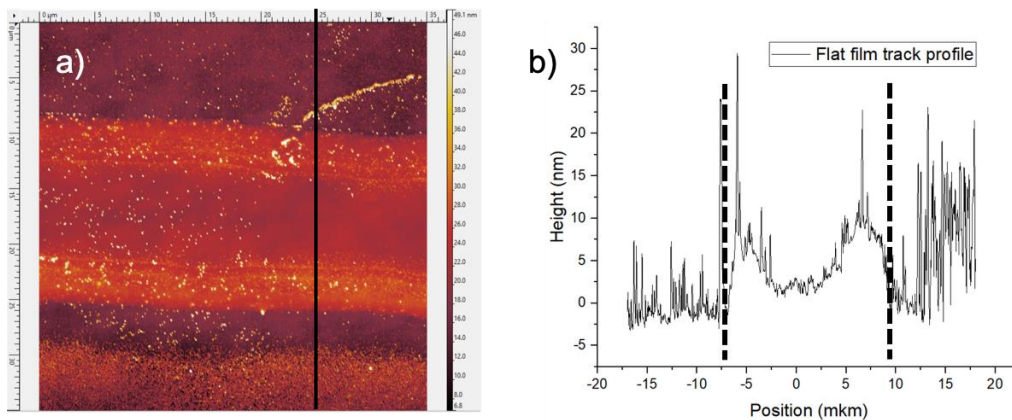


Figure 35 a) AFM scan of a section of laser-irradiated track produced with a scanning speed of ~ 8 mm/s, b) a topography contour extracted from the AFM image (along the black line on a)). The thickness of the uniform film was measured to be 4 nm.

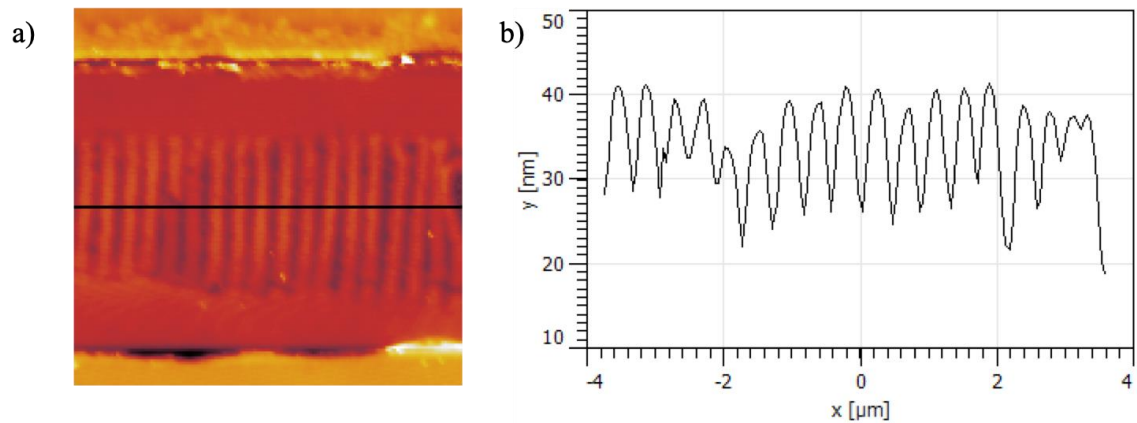


Figure 36 a) AFM scan of a section of a nanostructured photodetector consisting of MoS₂ nanoribbons, b) a topography contour extracted from the AFM image (along the black line on a)). The thickness of the nanoribbons may vary from 10 to 15 nm.

3.5.2 Raman spectroscopy

As mentioned above, Raman spectroscopy is highly important for the study of thin TMDC film. In this work, it was used to confirm that both 1D and 2D LIPSS structures that were produced indeed consisted of MoS₂ (Figure 37). Additionally, the distance between the E_{2g}¹ and A_{1g} peaks confirmed the structures obtained are thicker than 7 monolayers and, judging by the asymmetrical shape of the E_{2g}¹ peak, are not highly crystalline. No peaks showing presence of crystalline MoO₃ were detected [206].

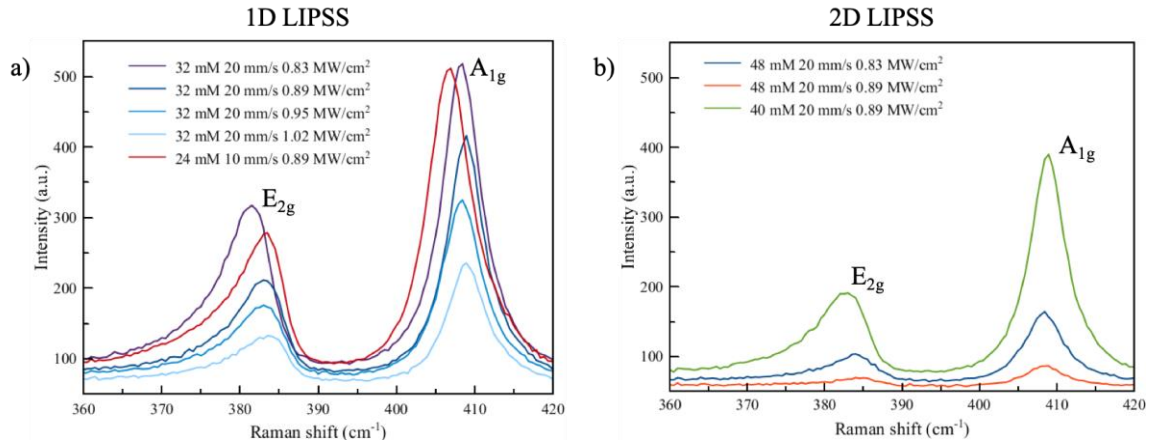


Figure 37 Raman spectra of nanostructured MoS₂ tracks corresponding to a) 1D LIPSS and b) 2D LIPSS obtained for a variety of parameters. The variety of synthesis parameters result in different film characteristics, i.e. thickness, which is reflected in the shifts of the A_{1g} and E_{2g}¹ peaks.

3.5.3 Photoconductivity characterization

Here, we utilized LIPSS-structured MoS₂, which can form linear arrays of nanoribbons, for the creation of a photodetector device to study the impact of nanostructuring on the performance of laser-synthesized photodetectors as compared to their continuous counterparts (Figure 38). For this purpose, several MoS₂ tracks were synthesized from a 24 mM precursor film. By adjusting the laser irradiation parameters, 1D LIPSS nano-structured MoS₂ and continuous film tracks were produced on the same substrate.

Photodetectors were fabricated from single tracks of laser-synthesized MoS₂ with a channel length (distance between contacts) of ~ 5 μm and a width of ~ 200 μm. Gold contacts were deposited on either side of the track where the central region of the MoS₂

track is located in the gap between contacts. The contacts were pre-defined using UV laser photolithography and double layer photoresist (an AZ1505 positive photoresist was deposited on an LOR5B sublayer) to optimize the lift off process, followed by magnetron sputtering deposition of a 40 nm gold film and lift-off.

Electrical measurements were carried out using a B1500A Agilent semiconductor analyzer.

The photodetectors were fabricated by depositing gold contacts on both sides of the MoS₂ tracks while the central area of the films served as the photoconductive channel. The gold-MoS₂ contact is a Schottky contact.

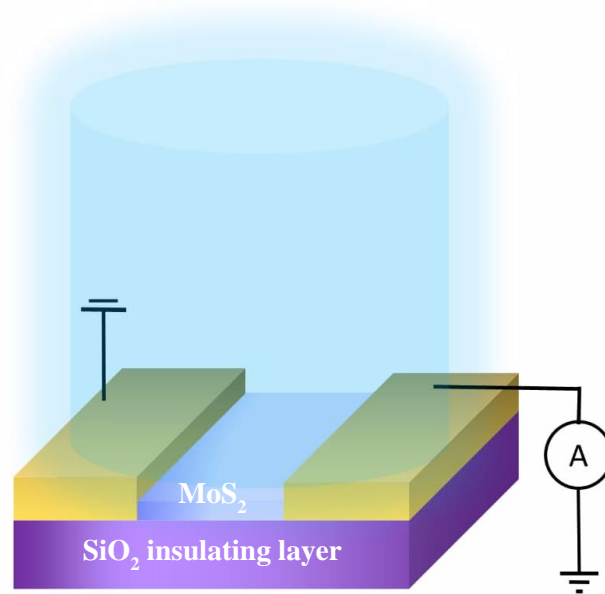


Figure 38 Schematic of a photodetector device.

The device was biased by 5 V and the photocurrent was measured as a function of the optical power at two distinct excitation wavelengths ($\lambda_1 = 650$ nm and $\lambda_2 = 450$ nm).

This was done by irradiating the photo-conducting device with non-focused laser beams at 450 and 650 nm. Due to the beam spot being much larger than the size of the device, the irradiation of the photo-conducting MoS₂ strip and the gold contacts was uniform. Therefore, the irradiation had no effect on the Schottky barrier of the contacts. Figure 39a shows an AFM image of a section of the nanostructured MoS₂ photoconductor that consists of a linear array of isolated MoS₂ nanoribbons that are bridging the gap between the gold contacts.

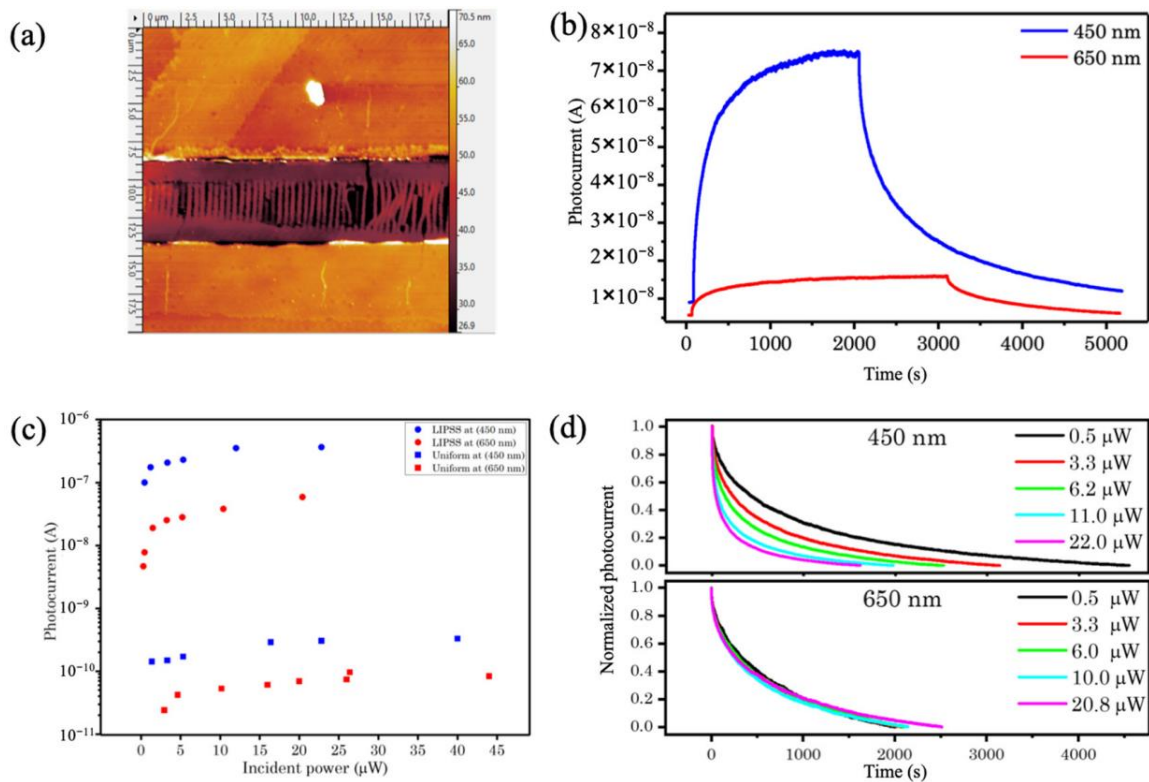


Figure 39 (a) AFM image of the nanostructured device. The central section consists of an array of isolated nanoribbons enveloped by a pair of metal (Au) electrodes (top and bottom); (b) temporal evolution of photocurrent (growth and decay when excitation laser is switched on and off, respectively) for 650 and 450 nm excitation, at the same power

(5.3 μW); (c) saturation values of the photocurrent as a function of incident power for 650 and 450 nm excitation, for nanostructured (LIPSS) and continuous devices; (d) decay curves of the photocurrent corresponding to 450 nm (top graph) and 650 nm (bottom graph) excitation, for various excitation powers.

Figure 39b shows the temporal evolution of the photocurrent for the nanostructured MoS_2 photodetector obtained using 450 and 650 nm excitations, corresponding to the same optical power level. The rise and fall dynamics of the device are rather slow, suggesting that the device exhibits persistent photoconductivity [145, 142, 146, 147]. The saturation value of the photocurrent (at 450 and 650 nm) was measured as a function of illuminating power for both nanostructured and continuous photodetectors and the measurements are summarized in the plot of Figure 39c. Generally, both devices were more responsive to short excitation wavelengths due to higher optical absorption.

Most importantly, the amplitude of the photocurrent corresponding to the nanostructured device is three orders of magnitude higher as compared to that measured in the continuous device for both excitation wavelengths. This is despite the fact that both nanostructured and continuous MoS_2 films were synthesized from the same precursor film using the same laser intensity (even within the same scanning track).

The difference in the film thickness (4 nm for the continuous film and 15-20 nm for the structured film) would certainly not be sufficient to explain this enhancement of

the photocurrent by three orders of magnitude. Instead, two other factors are most likely more significant here. The periodic surface modification acting as a grating could potentially cause a more significant change of the photocurrent by creating diffraction orders that increase the overlap between the excitation light and the photoconductor. And another factor would be the substantial increase in the density of shallow traps, as compared to continuous MoS₂ films, caused by the nano-structuring process [143].

The photocurrent decay dynamics in nanostructured devices are illustrated in Figure 39d, where the normalized decay curves for nanostructured devices corresponding to 450 nm (top) and 650 nm excitation are shown. Further analysis of the photocurrent decay curves has been conducted by fitting the double exponential decay function shown below:

$$I_{PC} = A_1 e^{-\tau_1 t} + A_2 e^{-\tau_2 t},$$

where I_{PC} is the photocurrent and τ_1 and τ_2 are the fast and slow components, respectively.

The fitted values for these decay time constants for 650 and 450 nm are presented in Table 4 and Table 5, respectively.

Table 4. Decay times at 650 nm.

Power (μW)	650 nm excitation	
	τ_1 (s)	τ_2 (s)
0.48	99	1055
3.3	107	1104

4.8	112	1134
6.0	134	1228
10.0	108	936
13.2	135	1148
20.8	101	1082

Table 5. Decay times at 450 nm.

Power (μW)	450 nm excitation	
	τ_1 (s)	τ_2 (s)
0.52	210	1639
1.44	151	1349
3.3	112	1063
5.3	100	931
6.2	95	831
70	50	469
11.0	45	457
13.2	32	343
22.0	40	409

The fitted values for the decay time constants τ_1 and τ_2 appear to become shorter with increasing laser power at the 450 nm excitation wavelength, whereas they seem to be independent of the excitation power at the 650 nm excitation wavelength. This behavior could be explained by the defect model that is given in [142], which provides a description of the photocurrent dynamics in photoconductors. In [142], the photocurrent decay dynamics were associated with the ability to excite preferentially one, or both types of charge carriers, with incident light. In materials that possess a high density of shallow trapping centers in their bandgap, it was argued that in a low intensity excitation regime, free carriers of one sign are primarily excited. In this case, the photocurrent relaxation dynamics is determined by the relaxation of this type of photocarriers. When the irradiation is cut off, the energy states filled with a certain type of carrier will empty, following an exponential decay rate.

However, at a high intensity excitation regime, photocarriers of both signs are excited, causing a significant increase in the free carrier density. In this case, the photocurrent relaxation dynamics will be faster. The higher the intensity of the incident irradiation was, the more the states will be filled with carriers of both types, and the more equal this distribution will be. Therefore, after the irradiation is cut off, the current will decay faster if the irradiation was more intense [142].

Here, we observed that excitation at 450 nm yields an order of magnitude higher photocurrent as compared to 650 nm. We can therefore attribute the observed dynamics to the difference in the photocarrier excitation efficiency of the two wavelengths, as indicated by the difference in the photocurrent. In these terms, excitation at 650 nm, at

the intensity levels that were used in our experiments, corresponds to the low intensity excitation regime and therefore there is no intensity dependence of the photocurrent decay times. On the other hand, 450 nm excitation accesses the high intensity excitation regime and relaxation time decreases with increasing irradiation power, as described in [142].

3.6 Concluding remarks

In this chapter, we have presented the formation of sub-micron 1D and 2D LIPSS patterns in direct laser-synthesized MoS₂ film tracks. This regular sub-micron patterning can, in some cases, result in extreme topographical modifications that lead to the formation of arrays of isolated ribbons with widths of ~ 200 nm or even less and lengths of several micrometers. The resulting nanoribbon arrays exhibit enhanced persistent photoconductivity, and their photocurrent increased by three orders of magnitude compared to their continuous film counterparts. The enhancement in the photocurrent is attributed to the increase of the shallow trapping centers' density in the film, as a result of the nano-structuring process; thus, LIPSS-based nanopatterning could be a promising route to enhance the photoelectrical properties of TMDCs by defect engineering.

Chapter 4. Laser-induced densification of porous silicon

4.1 Individual contributions

In this chapter, the following experimental work was performed by Salimon I.A.:

- All data analysis
- Laser irradiation of porous silicon samples
- Optical microscopy imaging
- Mechanical cleaving and SEM imaging of cross-sections obtained by cleaving
- Stylus profilometry

In this chapter, the following work was performed by colleagues:

- FIB cross-sections and SEM imaging in Helios FIB-SEM (Figure 41, Figure 42) were performed by Lipovskikh S. A.
- FIB etching and ToF-Sims investigation in Tescan Solaris FIB-SEM (Figure 46, Figure 47, Figure 48, Figure 49) were performed by Somov P.
- Assembly of custom laser writing setup was performed by Averchenko A. V.

4.2 Chapter summary

Laser induced structural modifications of porous silicon (PorSi) layers has been studied in this chapter.

Green and UV (532 nm and 244 nm respectively) laser irradiation were used to induce local thermal annealing in layers of porous silicon. The motivation for this investigation is to achieve selectively densified sections, with a higher refractive index as compared to the surrounding porous material. By scanning the laser beam along the

surface of the porous layer, it would thus be possible to fabricate optical waveguide circuits consisting of tracks of densified PorSi.

Using FIB-SEM and time-of-flight secondary ion mass spectroscopy (TOF-SIMS) module attached to this instrument allowed to construct volume maps of elemental content in specific areas of interest. We show that under appropriate parameters of laser irradiation and porous silicon layer density and thickness, it is possible to produce densified sections within volumes of PorSi which are immediately below the free surface of the material. In addition, rapid laser scanning may lead to a segregation of the porous silicon layer. This effect leads to formation of internal cavities and it is most pronounced for scanning speeds of ~ 1 mm/s, while slower scanning speeds at the same laser intensity exhibit significantly lower formation of cavities, despite the larger overall energy fluence in the latter case.

4.3 Details of experiment

Samples of mesoporous PorSi produced from p-doped Si were acquired from an external source. The thickness of the PorSi layer varied from $2 \mu\text{m}$ to $\sim 8 \mu\text{m}$.

In the experiments that are presented here, the scanning speed (the linear velocity of the translation stage) was within the range of $1\text{--}512 \mu\text{m/s}$. The laser irradiation process took place in ambient conditions.

The depth profile of surface recess on the laser irradiated areas was examined by the AlphaStep D-600 profilometer (KLA-Tencor, Milpitas, USA).

4.4 Observations on rapid laser scanning of porous silicon

A parametric study of scanned laser irradiation was undertaken to study the impact of varying the laser scanning on PorSi for laser irradiation at two wavelengths: 532 nm and 244nm. More promising results were obtained using UV radiation, which justifies the main focus of this work on 244 nm laser scanning; however, some effects are common for both visible and UV irradiation and will be discussed here.

4.4.1 Observations of 532 laser scan tracks

In Figure 40, optical images of laser tracks obtained for the same 532 nm laser intensity of 2.16 MW/cm^2 for a variety of scanning speeds are shown. A parametric study was undertaken to explore various speeds ranging from slower speeds that would definitely allow for thermal equilibrium throughout the scanning to faster speeds where the scanning laser beam would propagate faster than the spreading heat due to PorSi being a poor heat conductor. Slow scanning speeds between $7.8 - 31.3 \text{ }\mu\text{m/s}$, the high intensity scanning led to the visible melting of the PorSi layer. For the fastest scanning speed of $512 \text{ }\mu\text{m/s}$, however, there is visible damage of the porous layer, producing a much higher contrast in optical microscopy images, which is observably different from all other intermediate speeds ($62.5 - 256 \text{ }\mu\text{m/s}$) despite the lowest energy fluence that corresponds to the fastest scan. The laser track does not appear to be melted as in $7.8 - 31.3 \text{ }\mu\text{m/s}$ scanning tracks, while the visible damage appears to cover a larger area.

For further examination, cross sections of the laser-irradiated tracks were produced using FIB milling. In Figure 41, cross-sections corresponding to several laser-

irradiated tracks are shown. In these tracks, a lower laser intensity of 0.57 MW/cm^2 , was used to avoid severe laser damage by melting at lower scanning speeds.

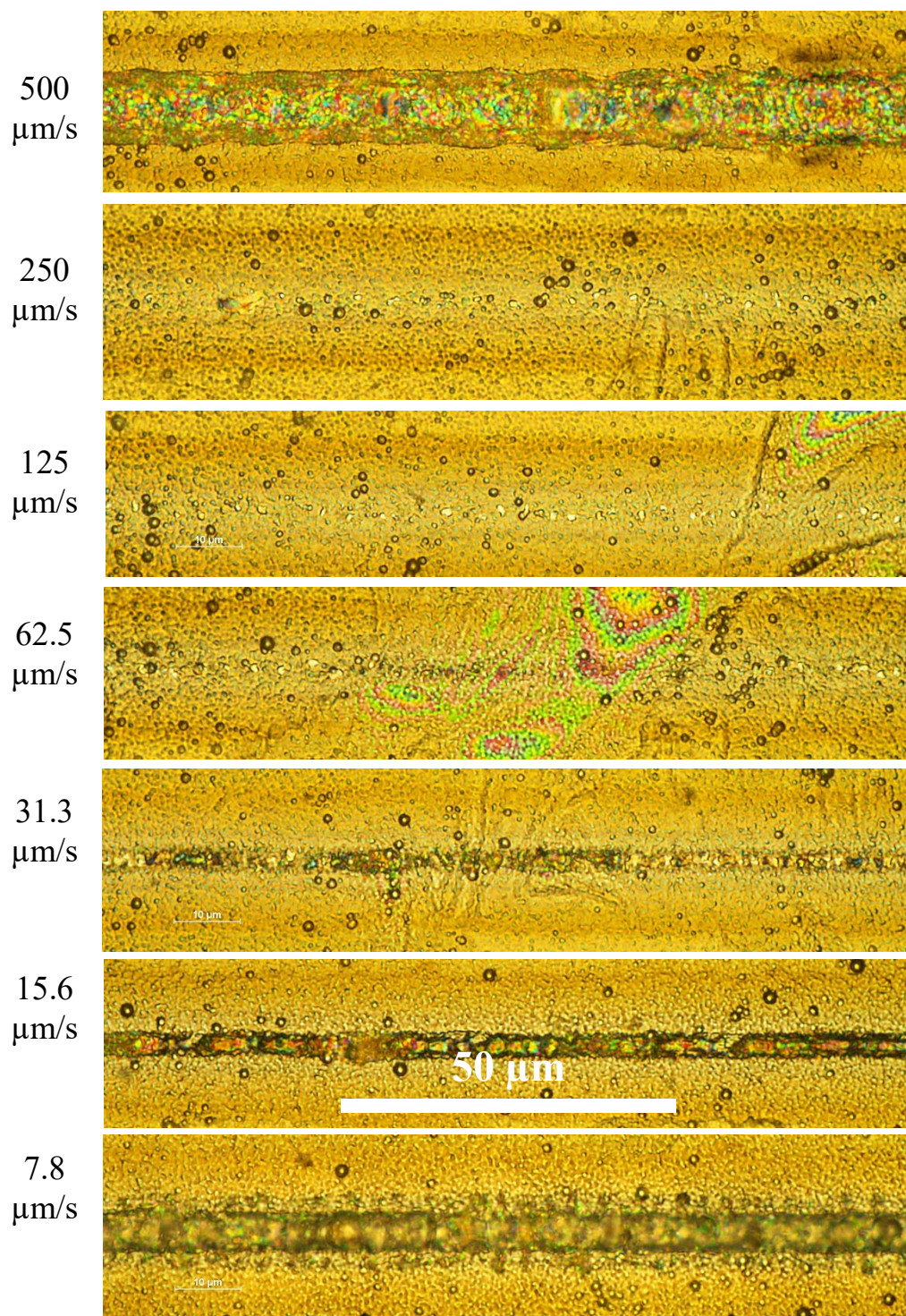


Figure 40 Optical microscope top view of 532 nm laser scan tracks obtained under laser intensity of 2.16 MW/cm^2 for various scanning speeds.

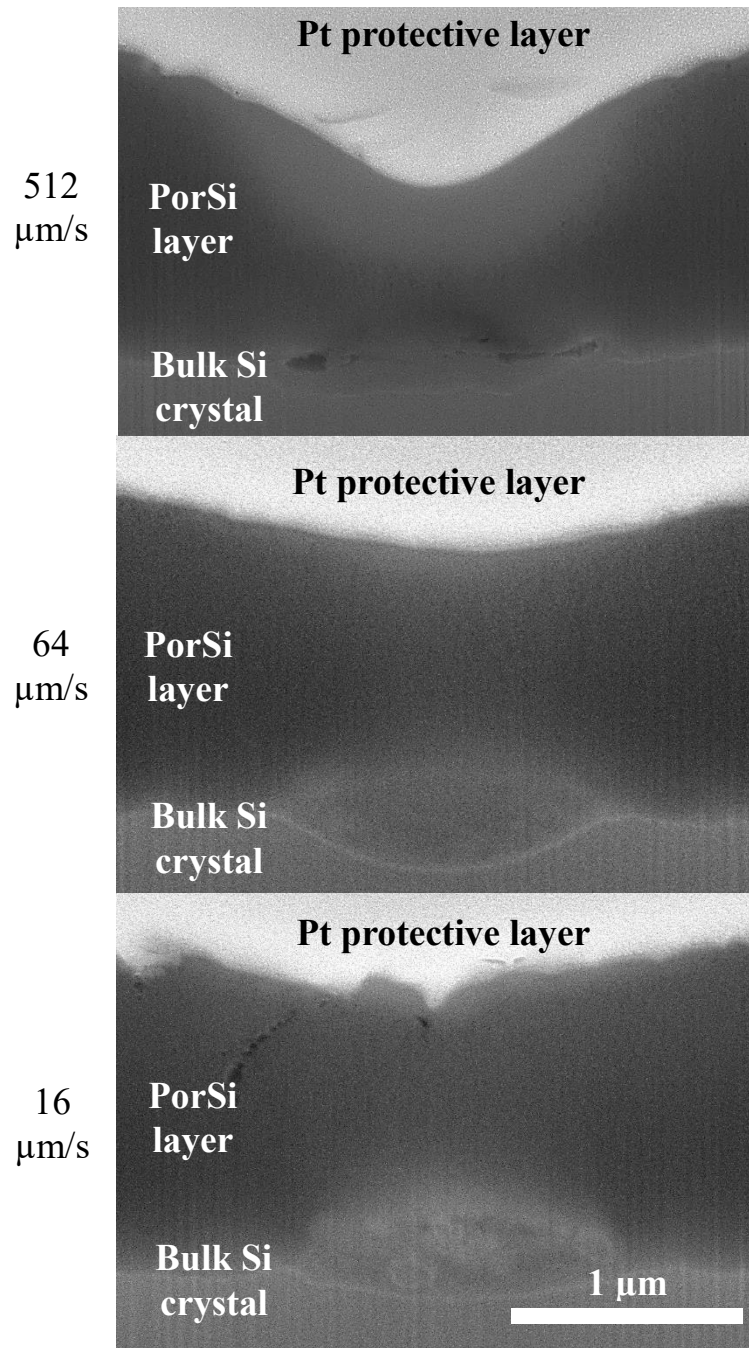


Figure 41 FIB cross-sections of 532 nm laser-irradiated tracks obtained using laser intensity of 0.57 MW/cm^2 for various scanning speeds. As shown in the figure, at the top of the cross-sections is a protective layer of Pt deposited on the surface of the PorSi layer

to facilitate producing a smooth surface of the cross-section. In the middle is the PorSi layer. Lastly, at the bottom of the images is the bulk Si crystal. SEM images were produced by Lipovskikh S. A.

Two significant features can be observed: the recess of the surface of the PorSi layer and damage on the interface between PorSi (the thickness of the PorSi layer here is $\sim 2 \mu\text{m}$) and the bulk Si crystal. The recess is much more pronounced for greater scanning speeds, while for the low scanning speed of $16 \mu\text{m/s}$ it is barely observable. The damage observed on the interface between PorSi and the bulk Si crystal allows to suggest that a significant portion of the laser energy is absorbed on this interface rather than the surface of the PorSi layer. To increase the absorption of energy specifically in the PorSi layer, further investigation was mainly conducted with 244 nm irradiation, and with thicker PorSi layers when possible.

4.4.2 Observations of 244 laser scan tracks

On Figure 42, the FIB cross-sections of two laser-irradiated tracks obtained under various laser intensities are provided for the laser scanning speed of $256 \mu\text{m/s}$. For the higher laser intensity of 49.5 kW/cm^2 a distinct cavity is formed in the porous layer. For a lower laser intensity of 21 kW/cm^2 , several much smaller cavities are observed. Besides the formation of cavities in the PorSi layer, a surface recess is formed similar to the observations of 532 nm laser treatments.

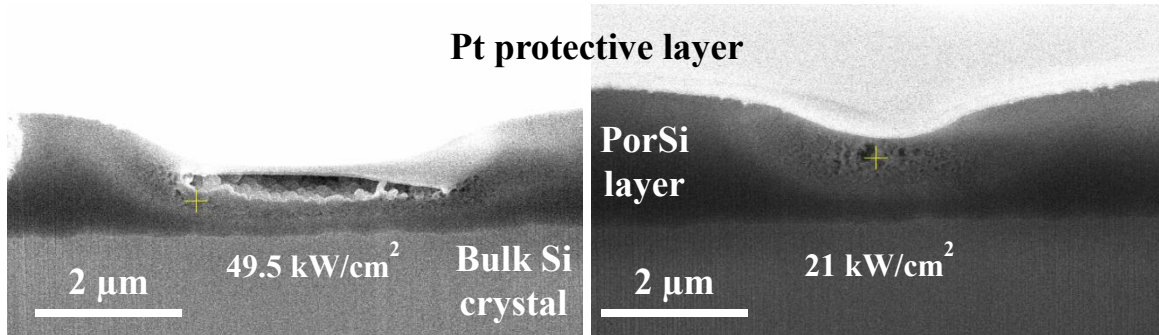


Figure 42 SEM images of FIB-produced cross-sections of 244 nm laser-irradiated tracks obtained using two different laser intensities (as indicated in the figure) for a scanning speed of 256 $\mu\text{m/s}$. SEM images were produced by Lipovskikh S. A.

After these initial observations, thicker layers of PorSi were used in subsequent studies. These samples had a thicknesses of $\sim 8 \mu\text{m}$ and appear in general to have more regular surfaces containing less defects. Nevertheless, the effects of the laser scanning speed in the range of 10-500 $\mu\text{m/s}$ were still consistent throughout all the observations.

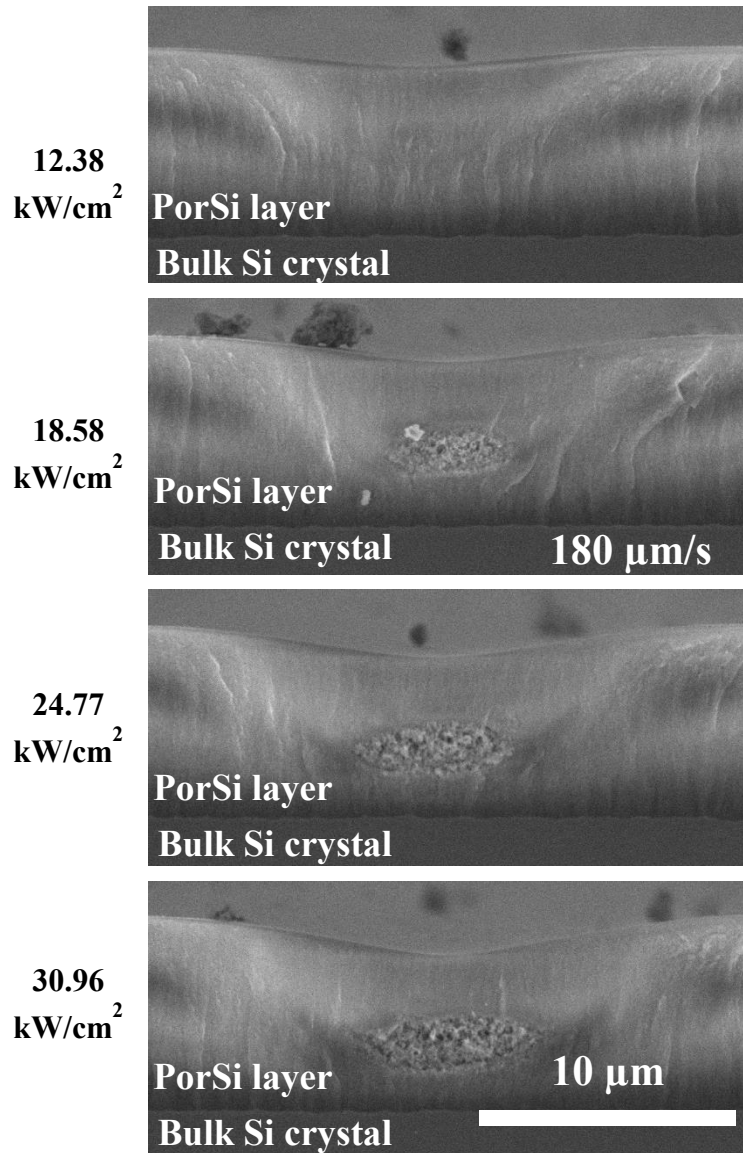


Figure 43 SEM images of cleaved edges showing cross sections of laser-irradiated tracks, indicating the effect of laser intensity (at 244 nm) for a constant scanning speed of 180 μm/s.

The structural stability of the PorSi layers allowed to use mechanical cleaving instead of FIB milling for a simpler and more available procedure. While the cleaving

would not achieve a perfectly flat plane of cross-section, Figure 43 and Figure 44 allow to observe the main features of the laser-irradiated tracks: the recess of the surface of the PorSi layer and the region containing a large cavity or a multitude of small cavities cavity inside the PorSi layer. It is worth noting that the cross-sections obtained by mechanical cleaving do not contain a protective Pt layer, as those obtained by FIB do.

Figure 43 shows how with increasing laser intensity the recess of the surface of the PorSi layer grows deeper. The region in which the modification is evidenced by growth of visible pores inside the PorSi layer appears to grow in volume with increasing laser intensity. For the lowest laser intensity of 12.38 kW/cm^2 the laser-irradiated track exhibits no such clearly observable region at all.

Figure 44 indicates that, in accordance with the observations corresponding to the 532 nm laser treatment, the recess of the surface is more pronounced at faster scanning speeds. The same is true for the volume of the cavity inside the PorSi layer. This appears

somewhat counter-intuitive, as faster scanning leads to a more dramatic structural modification despite the lower energy fluence.

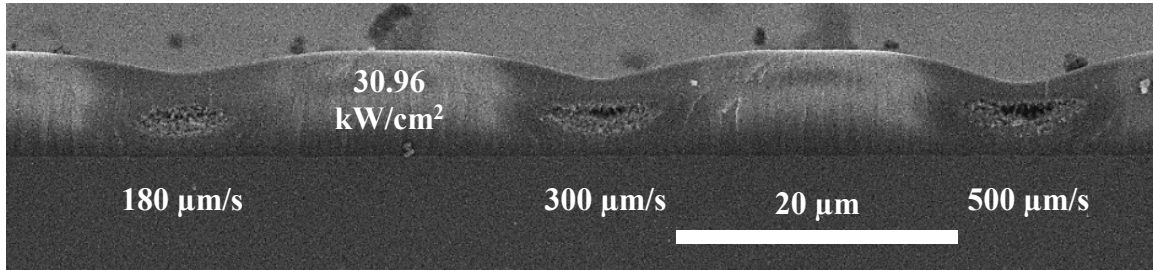


Figure 44 SEM image showing cleaved edges of laser irradiated tracks (at 244 nm) obtained using laser intensity of 30.96 kW/cm^2 and various scanning speeds, as indicated in the figure.

A surface recess appears as a result of laser irradiation, as shown in the SEM images of the track cross sections. Its characteristics (depth and width) were examined using stylus profilometry and the results are summarized in the graphs shown in. Each measured track corresponding to a set of parameters (laser intensity and scanning speed), three measurements were taken, at different locations along the track. As can be observed in Figure 45a, the depth of the surface recess of the PorSi layer increases with the laser scanning speed, which is consistent with the observations of FIB cross-sections and cleaved edges. However, the width of the valleys formed by the recess of the PorSi layers does not. Instead, the valleys formed by laser irradiation are wider for the slower scanning speed (Figure 45b). While the width of the valleys for by the laser irradiation

varied noticeably in different locations, the depth of the resulting recess was quite consistent in comparison.

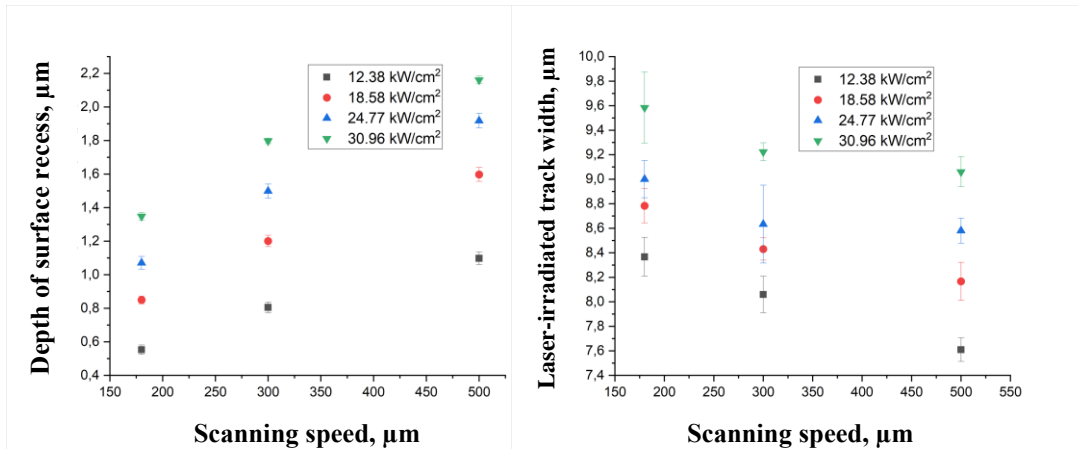


Figure 45 Stylus profilometry data: a) depth of surface recess, b) width of the surface recess at half depth.

Some considerations to explain the observations can be reasoned from a comparison with the known process of silicon layer transfer [207]. This process is used to produce thin membranes of single crystal Si by annealing multilayered PorSi. A thin single crystal layer of Si may be formed near the surface due to it acting as a vacancy sink [207]. In the layer transfer process, annealing of PorSi leads to material transfer through the movement silicon vacancies. In a two-layer system, pores in the less porous layer shrink, while pores in the more porous layer grow, the process being driven by the

reduction of surface energy. The difference in porosity between the layers plays a huge part.

The above considerations do not provide an explanation of why the higher speed laser scanning, which likely involves a rapid non-equilibrium heating of the PorSi layer, leads to more significant material re-deposition than the lower speed laser scanning that is closer to maintaining thermal equilibrium. It can be reasoned, however, that the observed reduction of volume in the PorSi layer is explained by the shrinking of pores near the surface of the PorSi layer, while the observed formation of internal cavities is due to growth of pores in the deeper regions of the layer. Therefore, the areas near the surface should become denser due to the laser-induced annealing as a result of the shrinking of pores.

The following section will provide additional evidence to support this claim by analyzing the observations that were made in FIB etching of laser-irradiated tracks.

4.4.3 FIB etching and ToF-SIMS characterization of laser scan tracks

FIB milling was used to etch $30 \times 30 \mu\text{m}^2$ areas containing three laser-irradiated tracks, which were produced using parameters similar to Figure 44 (scanning speeds of 500 $\mu\text{m/s}$, 300 $\mu\text{m/s}$ and 180 $\mu\text{m/s}$ for a laser intensity of 30.96 kW/cm^2). The accelerating voltage used was 20 kV and the ion current was 4 nA.

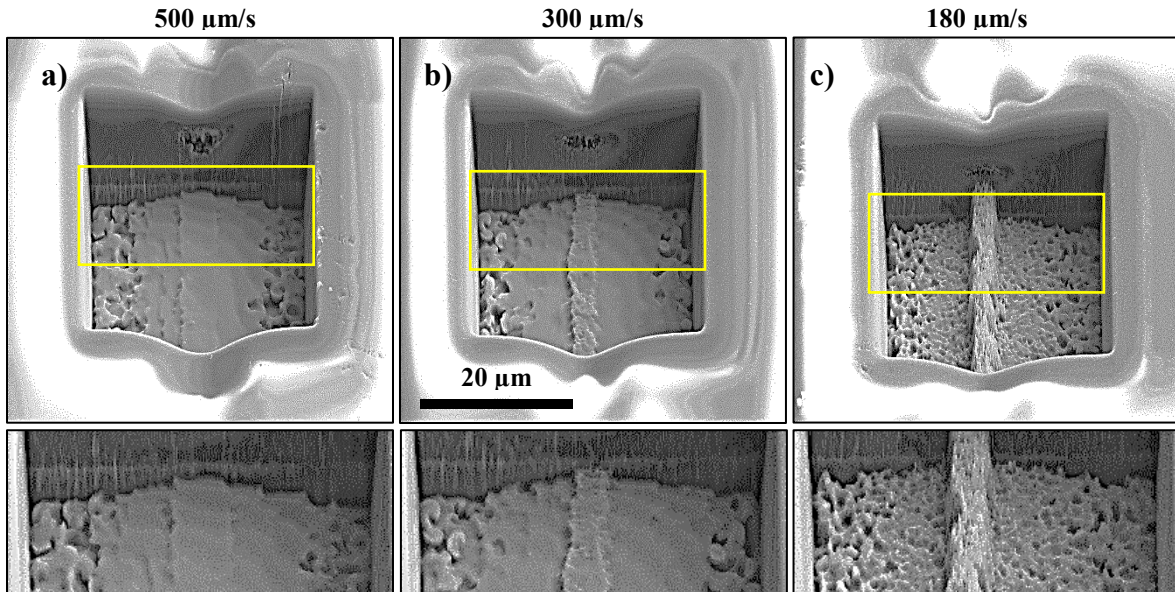


Figure 46 SEM images showing $30 \times 30 \mu\text{m}^2$ areas etched by ion beam milling. Close-ups show the interface between the PorSi layer and the bulk Si crystal underneath. The pits contain sections of laser-irradiated tracks (at 244 nm) obtained using laser intensity of 30.96 kW/cm^2 for various scanning speeds as indicated in the figure. SEM images were produced by Somov P.

The side wall of the etched square pits that corresponds to the cross section of the laser irradiated track, which runs along the vertical direction in the SEM images of Figure 46, shows the surface recess and formation of internal cavities. However, an additional observation can be made by viewing the bottom of the obtained pits. Every point of the etched areas was subjected to the same flux of ions with identical energies; however, the bottom of those areas is neither flat, nor does it follow the profile of the surface of the PorSi layer. Instead, the middle areas of the etched pits that correspond to the centers of the laser-irradiated tracks are elevated. This is especially evident when observing the side

of the bottom of the etched pits for which the close-up is provided. The level of the bottom can be followed by observing the line separating the wall of the etched pit and the bottom: the wall of the etched pit is flat. For the slower laser scanning speed (Figure 46c), the elevation is much more prominent and narrow, but it is still observable even for the faster laser scanning speed (Figure 46a). It can be concluded that the middle of the laser-irradiated track contains PorSi material that is milled at a slower rate than the PorSi outside of the laser-irradiated area.

Several factors could explain this reduction in the speed of the ion etching rate [208]. One possibility is that the material in the slower-milled PorSi in the center of the laser-irradiated tracks is denser. Another explanation could be that the reduction of ion milling is caused by oxidation, since the elements with lighter atomic cores are more resistant to ion sputtering. Some re-deposition of the material etched away by ion irradiation is to be expected; however, since such re-deposition would cover the surface uniformly, it could not be the sole reason behind the observed elevation.

To support the notion that the central areas of the laser-irradiated tracks undergo a degree of densification and to demonstrate that oxidation is unlikely to explain this change in ion etching rate, ToF-SIMS depth profiles of O^- collected signal (Figure 47) and snapshots of the various stages of the etching are provided (Figure 48).

The front projections in Figure 47 are somewhat similar to images of the cleaved edges, since the XZ plane is perpendicular to the direction of the laser-irradiated tracks. An important difference, however, is the fact that the Z axis is represented in frames rather than units of length. A “frame” here is a single full raster scan of the ion beam over

the area of interest, during which each point of the area receives a set dose of ion flux. In the case of prolonged ion etching, material from the surface is gradually removed by collisions with ions from the beam; therefore, each subsequent frame collects information from a deeper layer. Consequently, frames can be considered as a measure of depth; although, the actual depth difference that is achieved with each subsequent frame depends on the local ion etching rate, which in turn depends on the composition and density of the material locally.

While each X position receives the same dose of ion bombardment, the depth reached in every X position after the etching of multiple (370 frames for Figure 46a,b and 307 frames for Figure 46c) is different. Due to the Gaussian profile of the incident laser beam, various X positions across the laser-irradiated track are subjected to a different local laser intensity, with the maximum of laser intensity at the center of the track. The change of the PorSi material resulting from the laser-induced annealing is therefore different, leading to differences in ion etching rate across the X axis.

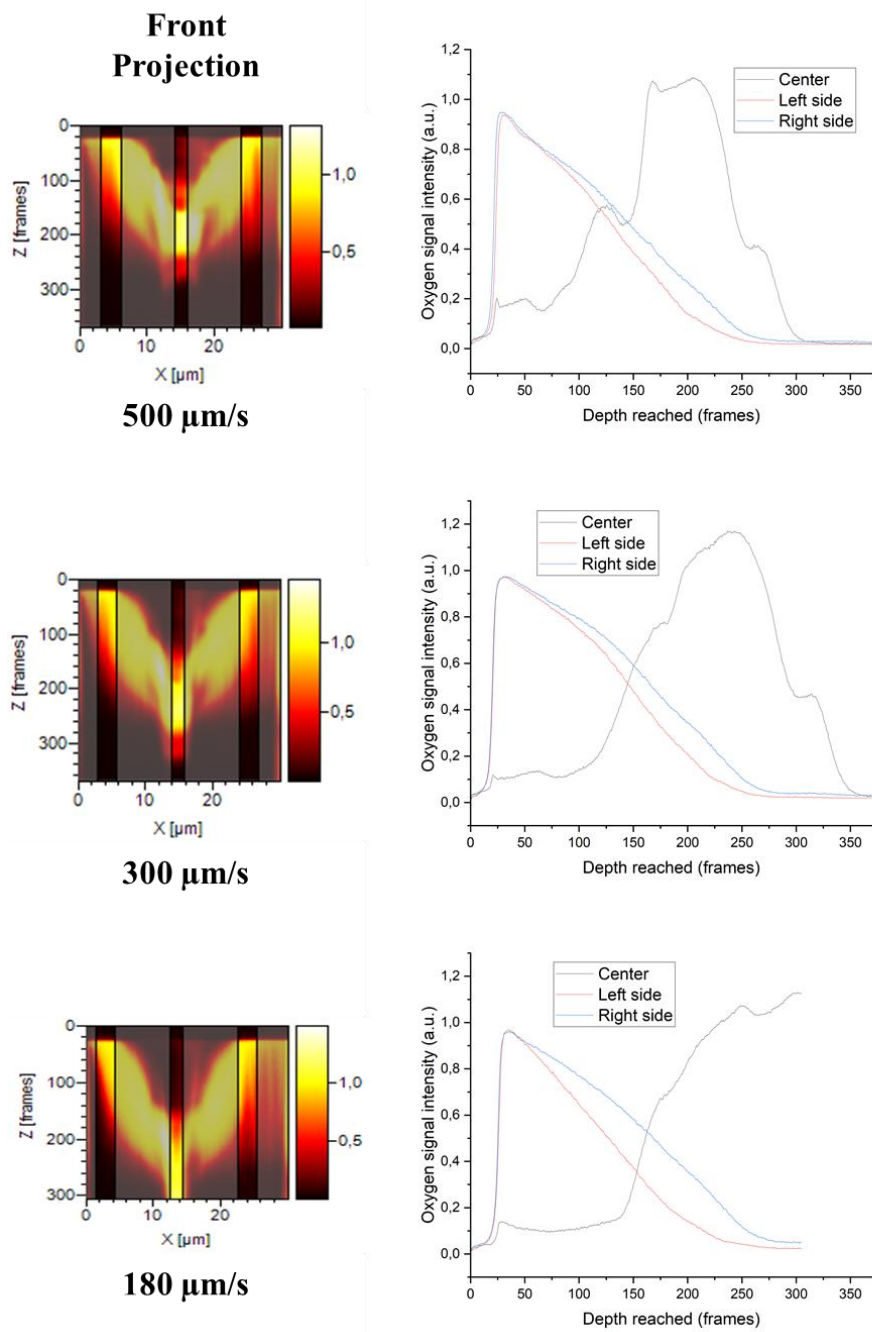


Figure 47 O^- signal collected during etching the pits on Figure 46: front projection with areas (center, left side and right side) selected and depth profiles of oxygen concentration collected in the selected areas.

The front projections and depth profiles on Figure 47 show a 2D map of the signal collected for the charge to mass ratio (m/z) of 16, which corresponds to O^- ions. This oxygen ion signal is characteristic, outlining the boundary for the PorSi layer. When PorSi layers are kept in ambient conditions, it should be expected that air is absorbed by the porous structure. Additionally, after irradiation with 244 nm UV laser, it is reasonable to expect some degree of oxidation. Therefore, registering an oxygen signal means the ion etching currently progressed through the PorSi layer. The bulk Si crystal, however, should not contain oxygen, so the oxygen signal levelling off indicates that the ion etching front reached the underlying bulk Si crystal.

The depth profiles (graphs on the right hand side) in Figure 47 correspond to three different positions across the track width; i) a narrow X window located at the center of the laser-irradiated track and ii) two similar windows either side of the center track, at 7-10 μm away from it, which should correspond to positions outside the laser beam spot. Some asymmetry between the profiles on the left and the right side is present due to the position of the detectors, so both the left and the right side are provided for the sake of comparison.

All the profiles of the side areas that are located away from the center of the track show that the observed oxygen signal peaks at the depth of ~ 35 frames and decays after ~ 250 frames of ion etching, at which point the bulk Si crystal is reached. A possible explanation for why the signal is extremely low for the initial frames could be that the oxygen at such shallow depths is desorbed in the high vacuum environment of the FIB-SEM setup.

For the depth profiles of collected oxygen signal at the central areas, a different situation is observed. The signal sharply rises at ~ 35 frames, but to a much lower level as compared to the sides. Then only after tens of frames of etching it rises, reaches a maximum (much more slowly than the side areas), then goes down until levelling off upon reaching the bulk Si crystal (with the exception of the $180 \mu/s$ laser scanning speed, for which the maximum of oxygen concentration only appears to be reached after ~ 300 frames of ion etching).

Additional insight into this process of ion etching could be obtained from Figure 48, which provides top projections of the oxygen signal collected in specific frames along with corresponding FIB images collected during ion etching.

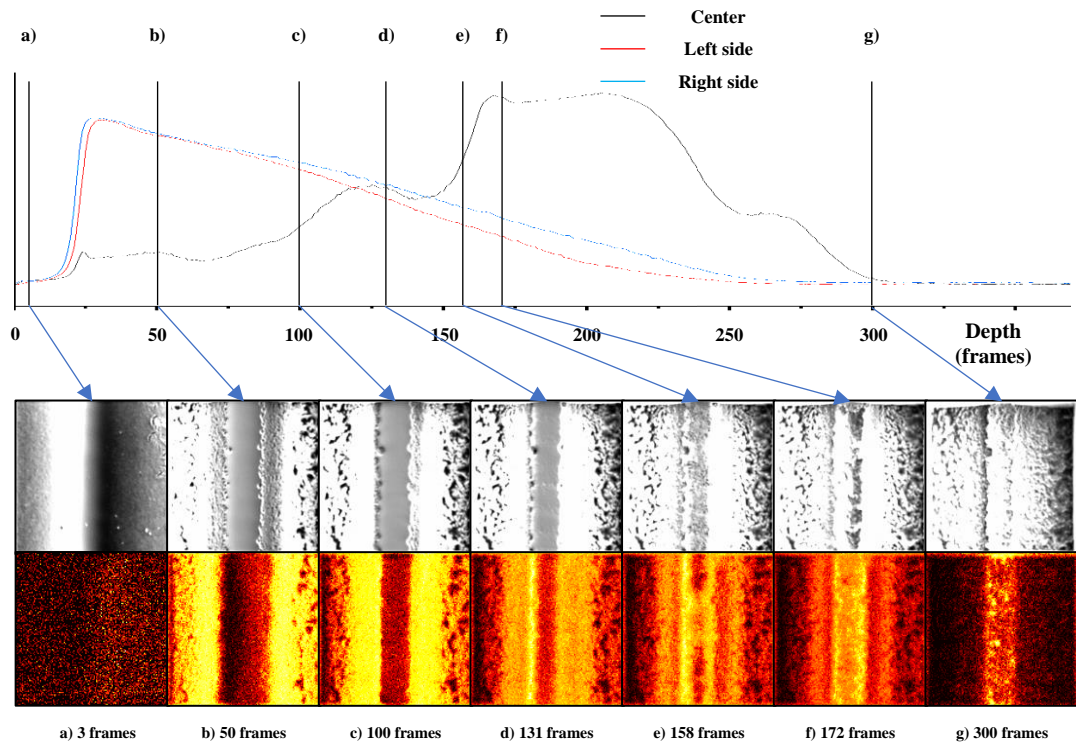


Figure 48 Depth profile of O^- signal collected during etching the pit on Figure 46a corresponding to $500 \mu\text{m/s}$. FIB images (gray) and front projections of O^- signal collected (colored) provided for specific etching frames.

Frame “a” corresponds to the initial stage of ion etching. Due to the position of the FIB imaging detector, the left part of the images tends to be brighter. At that stage, FIB imaging only shows the recess of the surface. The ToF detector, on the other hand, is positioned differently, so the right part of the colored front projection is brighter. Nevertheless, the oxygen signal collected is low across the board.

Frames “b”, “c” show a smooth central part of the laser-irradiated track. To both sides of the track, however, the ion etching leads to a high roughness due to minor

inhomogeneities being exaggerated by the ion etching. The collected oxygen signal in the center of the laser-irradiated track is very low. This supports the hypothesis that the central part of the laser-irradiated track is densified by the shrinking of the pores, and while some oxidation is to be expected, it is likely not the key reason for the decrease in the ion etching rate.

Frames “d”, “e”, “f” show how, as the ion etching progresses, two coincident observations can be made. Firstly, the FIB image shows how the central region of the laser-irradiated track appears to be more and more rough and ununiform. At the same time, the oxygen content in this region also increases. The maxima of collected oxygen signal shift gradually closer to the center of the laser-irradiated track.

Lastly, Frame “g” corresponds to the final stage of the ion etching process. Outside the central region of the laser-irradiated track, the ion etching has reached the bulk Si crystal, and the FIB topography image shows a smoother surface. Only in the central region of the laser-irradiated track, some oxygen signal is still collected and FIB topographical image shows an elevation of the bottom of the pit.

Figure 49 additionally shows a rapid change in the topography of the central region of the laser-irradiated tracks, occurring within a short sequence of 9 frames of etching. The large ion-etched pores visible in the beginning of the sequence expand quickly, giving way to a concave topography. It appears reasonable that such a change should correspond to the ion etching reaching the cavity observed on Figure 46a. This coincides with high levels of oxygen signal collected by ToF-SIMs.

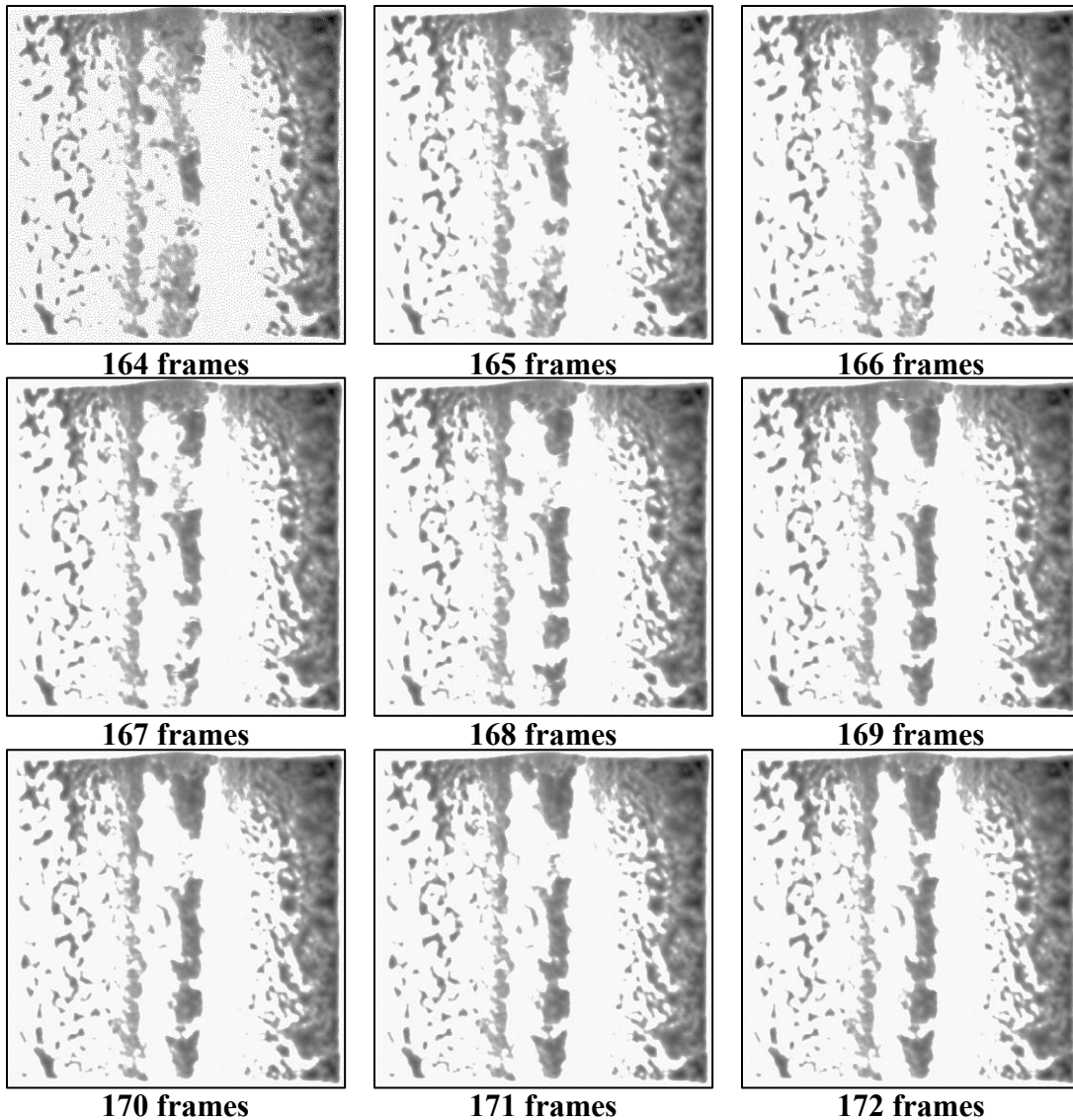


Figure 49 FIB topography images collected during etching the pit on Figure 46a. The frame numbers as indicated in the figure show a sequence of 9 frames of etching.

To summarize the above observations, laser scanning with speeds in the range of 180-500 $\mu\text{m/s}$ leads to rapid laser-induced annealing of the PorSi layer (the laser beam dwell time here varies between 12 and 33 ms). This results in the shrinking of pores in

the shallow regions of the PorSi layer close to surface, which causes a recess of the free surface and the formation of a denser region of PorSi. Underneath this densified region of the PorSi layer, pores grow larger instead, thus forming a multitude of submicron size cavities, or even merging in a single large (up to several microns wide) cavity. The air contained in the PorSi layer either escapes outside the layer or becomes trapped in the forming cavities. The recess and formation of internal cavities are more pronounced for faster laser scanning speeds. Due to the rapid shrinking of the pores in the densified region, it does not appear to be strongly oxidized by the UV irradiation even when the laser scanning is performed in ambient conditions.

A qualitative estimation of the density change in the laser-irradiated tracks can be made by comparing the FIB cross-sections (Figure 46) with the depth profiles of the oxygen signal collected (Figure 47). The number of frames contained in the initial plateau of oxygen signal collected (Figure 48, frame “b”) was divided by the visually identified

thickness of the densified region of the PorSi layer above the region in which the internal cavity is formed, providing an inverse etching rate (Figure 50).

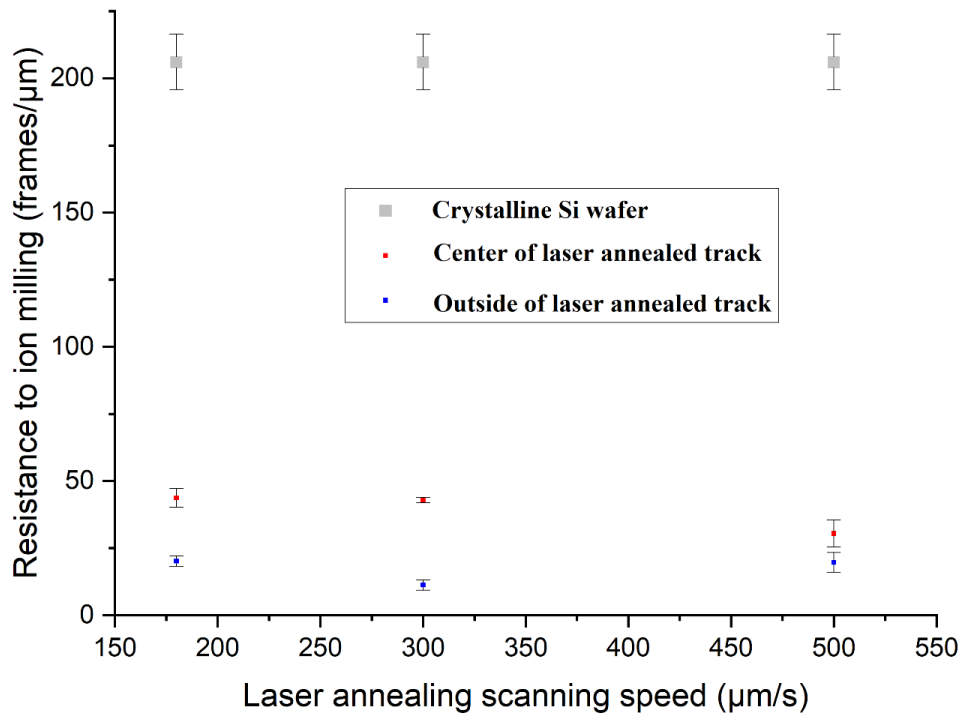


Figure 50 Estimated resistance to ion milling for 244 nm laser scan tracks obtained under laser intensity of 30.96 kW/cm^2 for various scanning speeds.

While density is not the only factor possibly influencing the etching rate, Figure 50 suggests that the change in the density of the densified region compared to the unaffected PorSi may be significant. This would mean that such laser irradiation could be used to form channel waveguides in PorSi layers, since the densified region would have a higher refractive index than all surrounding media, allowing to confine light.

4.5 Concluding remarks

Laser annealing of PorSi using c.w. laser radiation at 244 nm with short (12-33 ms) dwell times was observed to induce significant shrinking in the PorSi layer, as indicated by a recess of the free surface and formation of internal cavities inside the porous material. More severe shrinking is observed for faster laser scanning speeds despite lower dwell times and lower amounts of the energy fluence. There is strong indication, provided by FIB and TOF-SIMS analysis, that a densified region of the PorSi layer is formed, with no significant oxidation despite UV irradiation in ambient conditions.

Such an annealing process could be a route for direct laser writing of channel waveguides in PorSi layers. The simplicity of this single step process could make it promising for low cost production of integrated optical circuits that could target sensing applications. Furthermore, this direct laser writing approach is ideal of rapid prototyping of devices.

Chapter 5. Patterning of precursor films for TMDC synthesis by e-beam scanning

5.1 Individual contributions

In this chapter, the following experimental work was performed by Salimon I.A.:

- Data analysis
- Development of pre-patterned precursor films
- Optical microscopy imaging
- AFM profiling
- Raman spectroscopy
- E-beam pre-patterning of precursor films in Tescan Vega SEM

In this chapter, the following work was performed by colleagues:

- E-beam pre-patterning of precursor films in Tescan Solaris FIB-SEM were performed by Statnik E. S. (Figure 51, Figure 52, Figure 53, Figure 54) and Somov P. (Figure 55, Figure 57, Figure 58)
- Assembly of custom laser writing setup was performed by Averchenko A. V.

5.2 Chapter summary

While aforementioned (in Chapter 3. Laser-assisted production of nanostructured 2D-TMDCs) laser writing methods allow for simultaneous patterning along with synthesis of TMDC thin films from spin-coated precursor films, the size of the laser beam spot limits the resolution of patterning to several μm . Furthermore, simultaneous synthesis and patterning, as demonstrated in published work on laser synthesis of TMDs

[11, 165] is not suitable for the independent optimization of both processes (synthesis, patterning). These constraints could be overcome by using an electron beam to produce a patterned precursor film that can be post processed to transform into TMDC. The process, and some preliminary results, will be presented below.

In this approach of TMDC synthesis we are considering a process, which is based on e-beam pre-patterning, which does not convert the precursor films into the target TMDC materials directly, but allows to locally suppress the solubility of the precursor film by electron bombardment. The exact mechanism that defines this change in solubility of the e-beam treated areas is unclear so far, although we speculate that low level heat induced by the e-beam induces a chemical reaction in the precursor to produce an amorphous form of the TMDC compound. Qualitative comparison to similar effects induced by low intensity of the laser irradiation of the same precursor suggests that the e-beam pre-processing may not be purely thermal in nature. However, films pre-patterned using e-beam scanning may produce features of high resolution, when using appropriate irradiation parameters are used, which can subsequently be post processed to be converted into the target material. Post-processing can be either laser annealing (used in this study) or thermal decomposition in a furnace under inert atmosphere. Importantly, the TMDCs that are considered in this study are MoS₂ and WS₂, which have been successfully produced using direct laser synthesis from single source thiosalt precursors ((NH₄)₂MoS₄, (NH₄)₂WS₄) [11, 165]. The results that are shown here are associated with MoS₂, for the purpose of comparison with prior work.

A Tescan Solaris dual-beam scanning electron microscope was used to facilitate both e-beam irradiation and analysis of the resulting structures. In a future implementation of this patterning method, conventional e-beam lithography equipment could be used. In fact, the method that is proposed here is in its essence e-beam lithography, with the precursor film playing the role of the e-beam resist.

5.3 Patterning of precursor films for TMDC synthesis by e-beam scanning

A parametric study of the e-beam pre-patterning of precursor films consisting of $(\text{NH}_4)_2\text{MoS}_4$ and $(\text{NH}_4)_2\text{WS}_4$ was undertaken using various test patterns such as rectangles, single tracks and single spots produced by non-scanning exposure.

The procedure that has been followed here regarding ammonium tetrathiomolybdate ($(\text{NH}_4)_2\text{MoS}_4$) precursor film preparation was the same as in Chapter 3. Laser-assisted production of nanostructured 2D-TMDCs. The precursor solution concentrations used were 24 mM and 48 mM. However, thinner films with a 12 mM precursor solution concentration were prepared as well, in an effort to improve the patterning resolution. In these experiments e-beam currents in the range of 1 nA and 10 nA were used with an accelerating voltage of 20 kV.

Following the e-beam exposure, which was conducted in the SEM's vacuum chamber, the samples were removed from the vacuum chamber and underwent a developing process, similar to that of laser irradiated precursor films that was described in Chapter 3. Laser-assisted production of nanostructured 2D-TMDCs. The developing process took place within ~ 2-4 hours after removal from the vacuum chamber. The topography of the e-beam irradiated areas was monitored by optical microscopy

observations between successive developing periods (by immersing the samples in the NMP solvent). E.g. for Figure 51, a notation of 30 s + 60 s indicates that the sample was immersed in NMP for 30 s, then dried, observed, and then immersed again for 60 s and observed again. This is to differentiate from a continuous immersion of the sample in the solvent for 90 s.

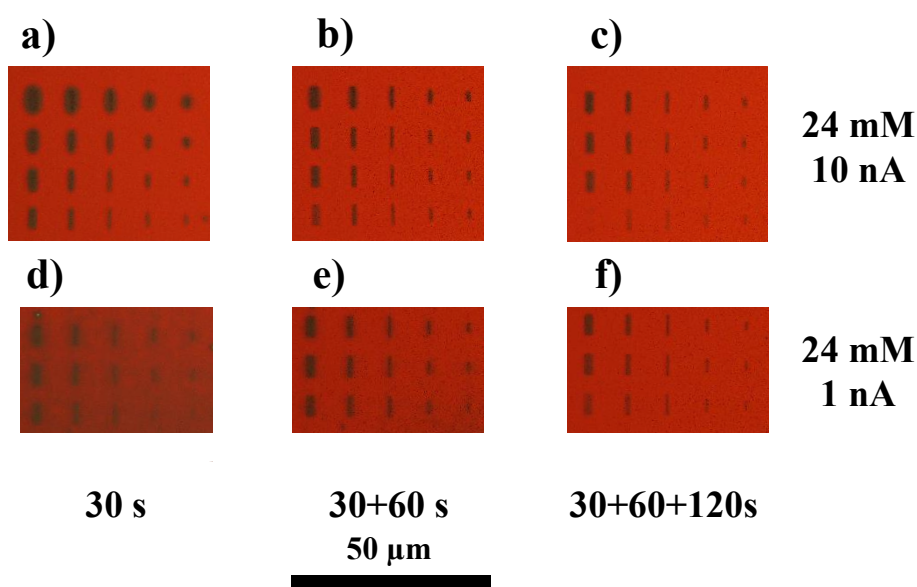


Figure 51 Development process snapshots of e-beam irradiated precursor film (24 mM) corresponding to various development times in NMP solvent as indicated in the figure. Rectangular features with aspect ratios varying from 2:1 to 10:1 were pre-patterned using varying dose of electrons. E-beam irradiation conditions correspond to a) 1 nA and b) 10 nA e-beam currents.

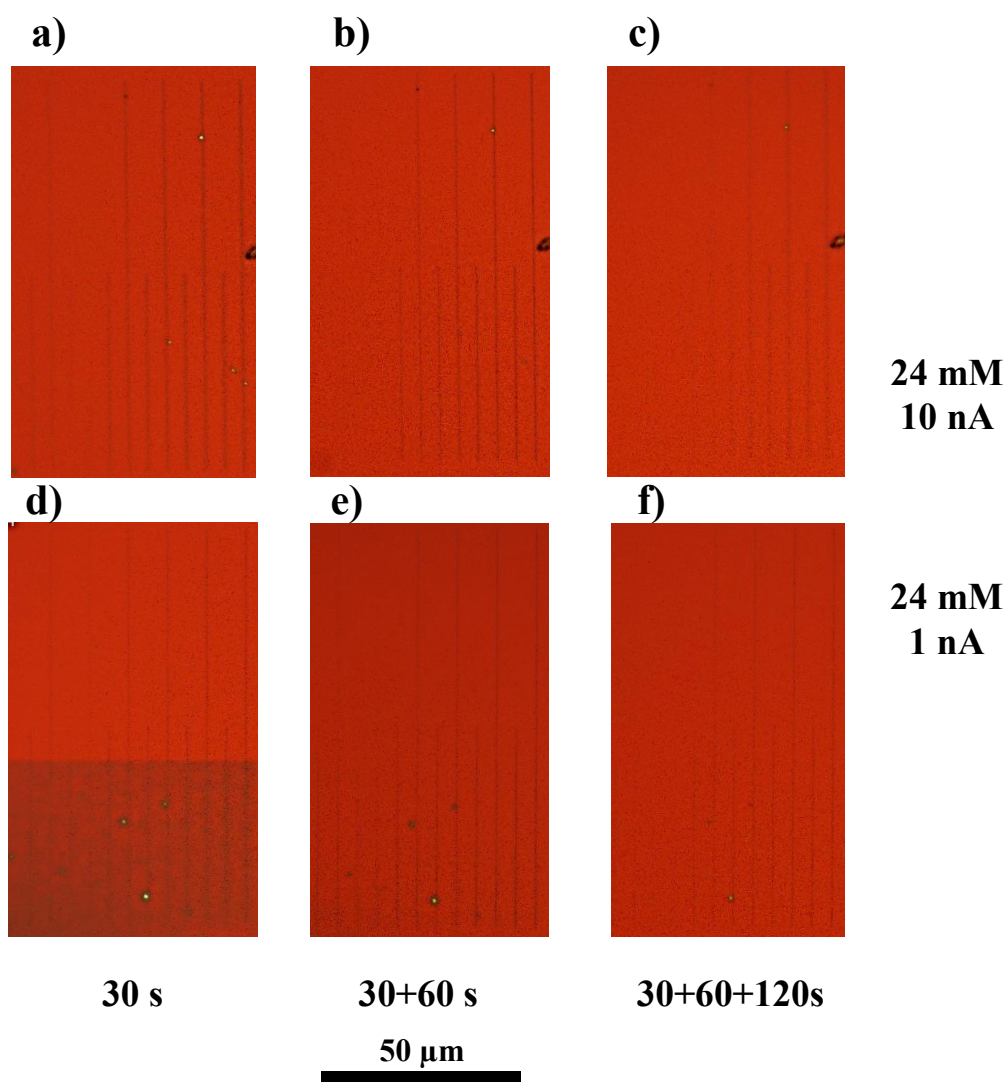


Figure 52 Development process snapshots of e-beam irradiated precursor film (24 mM) corresponding to various development times in NMP solvent as indicated in the figure. Thin line features were pre-patterned using varying dose of electrons. E-beam irradiation conditions correspond to a) 1 nA and b) 10 nA e-beam currents.

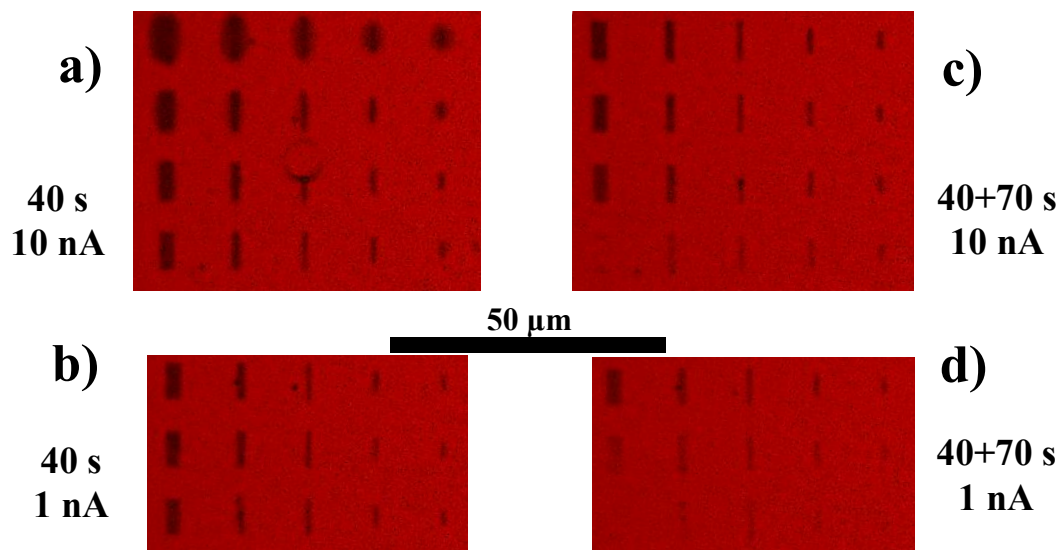


Figure 53 Development process snapshots of e-beam irradiated precursor film (12 mM) corresponding to various development times in NMP solvent as indicated in the figure. Thin line features with aspect ratios varying from 2:1 to 10:1 were pre-patterned using varying dose of electrons. E-beam irradiation conditions correspond to a) 1 nA and b) 10 nA e-beam currents.

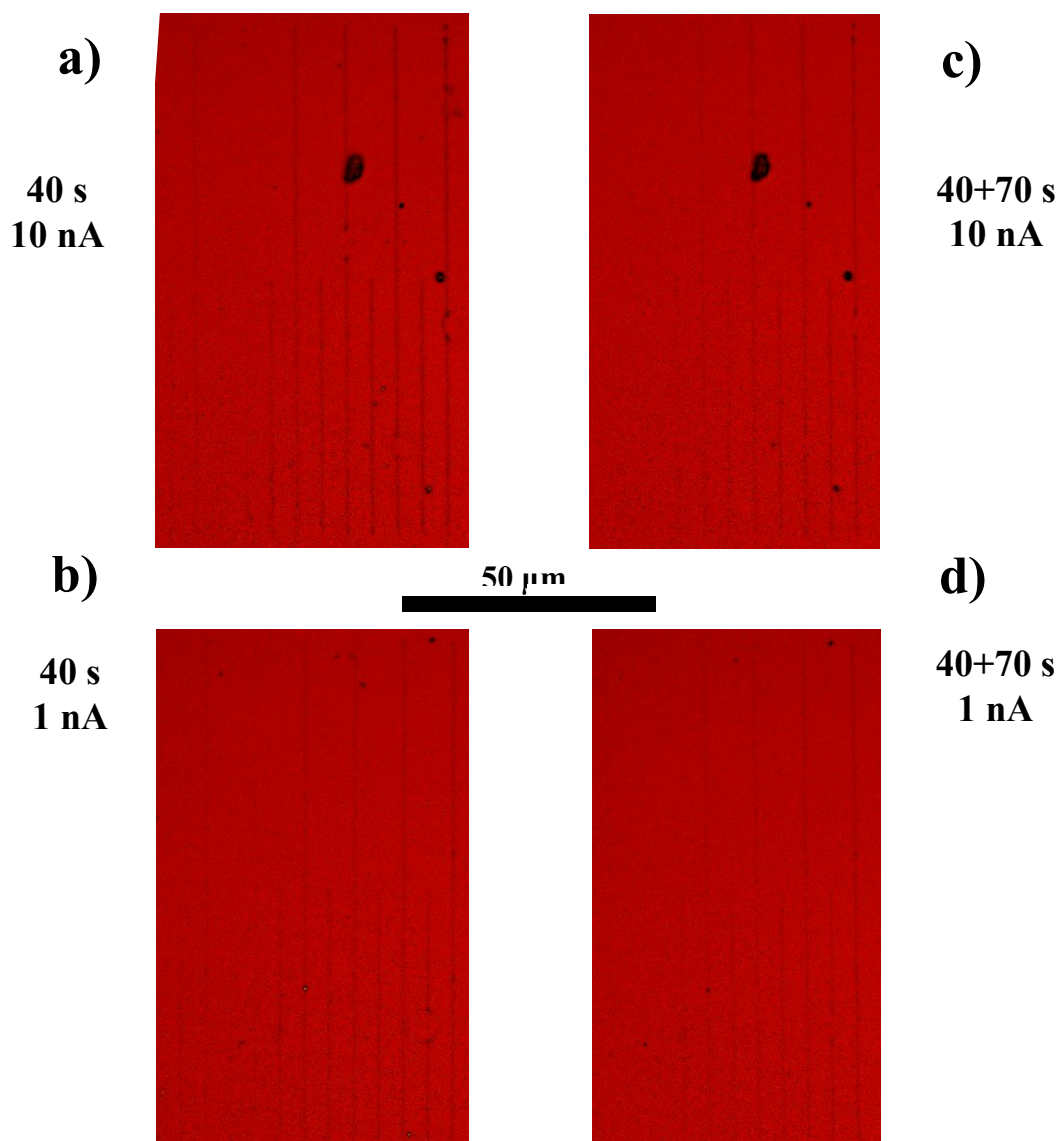


Figure 54 Development process snapshots of e-beam irradiated precursor film (12 mM) corresponding to various development times in NMP solvent as indicated in the figure. Thin line features were pre-patterned using varying dose of electrons. E-beam irradiation conditions correspond to a) 1 nA and b) 10 nA e-beam currents.

We have observed that the initial precursor solution concentration does not seem to affect the development of the pre-patterned films significantly. The duration of development in the NMP solvent used for this patterning method is shorter compared to those used in laser-synthesis experiments presented in Chapter 3. Laser-assisted production of nanostructured 2D-TMDCs. For samples that were immersed for a cumulative duration of 3.5 min (Figure 52), it can be observed that some of the features, such as the thin lines, begin to get damaged or even delaminated, which suggests over-developing.

For developing times as short as 30-40 s (Figure 51, Figure 52), the pre-patterned features are clearly under-developed. A “halo” of remaining film can be seen, surrounding some of the rectangular features. It is unclear whether this “halo” (Figure 55), which consists of thinner film as compared to the intentionally patterned area, is associated with features of the scanning e-beam or it is related with electron diffusion from the e-beam irradiated volume.

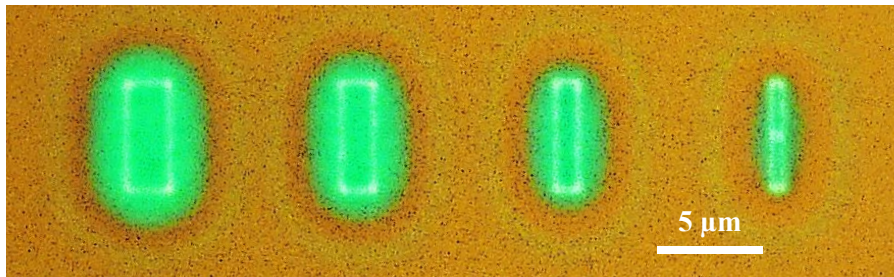


Figure 55 “Halo” features formed around overexposed rectangular features of patterned precursor film.

The measurements were conducted by AFM to determine how the time of exposure to e-beam scanning affects the width of thin lines (Figure 56). For low irradiation durations, the width of the features appear to be independent of the irradiation duration. After an irradiation duration threshold of ~ 30 s the line a “halo” appears as in the overexposed rectangles shown in Figure 55. The width of this “halo” is noticeably increasing with exposure time. Accumulation and diffusion of charge in the thin precursor film that is deposited on a 300 nm thick SiO_2 /p-type Si substrate might be responsible for this behavior by influencing either the precursor film directly or the adsorption of species from the ambient atmosphere, leading to the decrease of its solubility in the NMP solvent.

We have observed that the thinner 24 mM precursor film supports narrower features (Figure 56), allowing to pattern with a higher resolution. Patterned lines and dots

of MoS₂-precursor with a width as narrow as ~ 200 nm were obtained for films with a 24 mM precursor solution concentration. It is worth noting, though, that this width is significantly larger as compared to the size of the electron beam cross section (~ nm). Reducing the e-beam irradiation time further did not appear to allow for higher resolution, but instead reduces the robustness of the pre-patterning and may lead to delamination of the features at the development step.

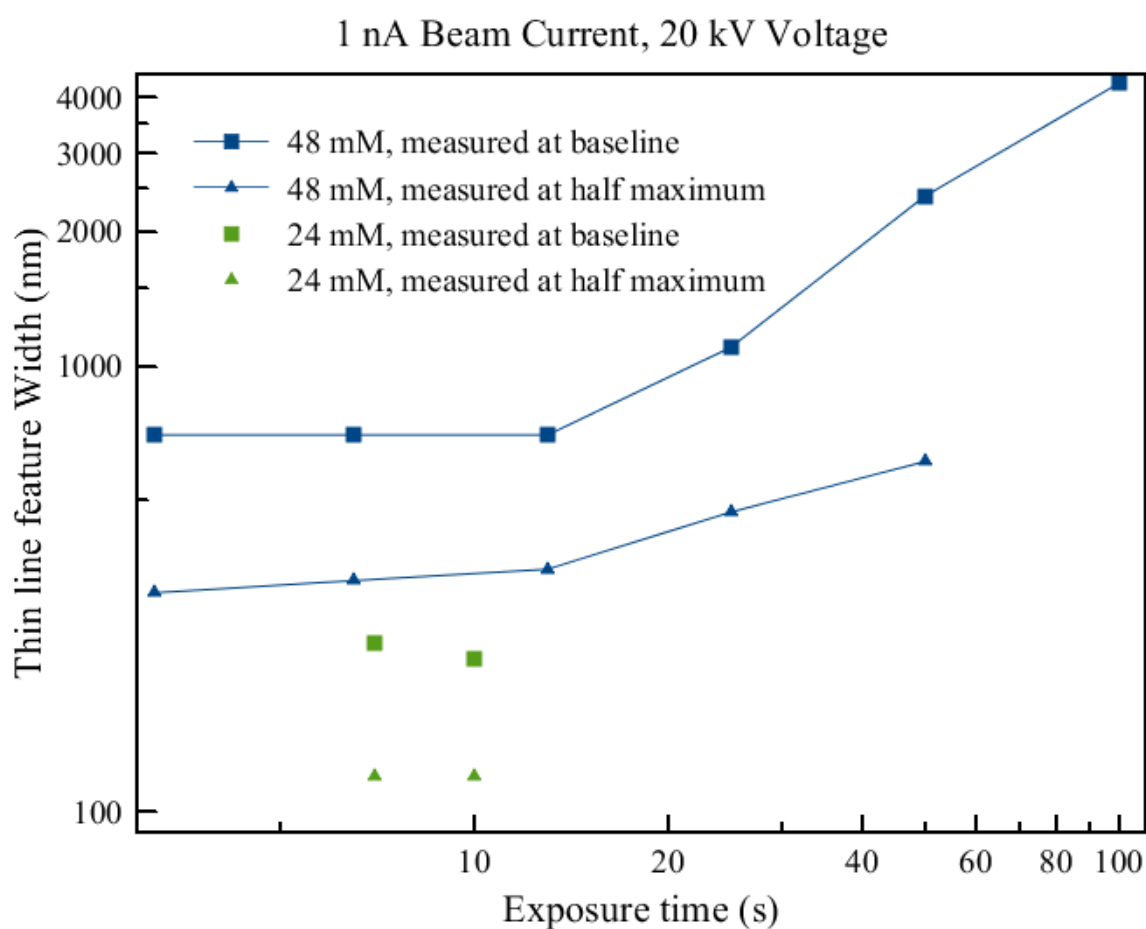


Figure 56 Width as a function of exposure (irradiation) time for thin lines with a 50 μm length, corresponding to precursor films which have been produced with initial precursor solution concentrations of 24mM and 48 mM.

5.4 Laser synthesis of patterned MoS₂ features from patterned precursor films

In a final step of the synthesis process the e-beam irradiated patterned films were converted to MoS₂ by local laser annealing. In this case, the laser intensity that was required for the conversion of the e-beam irradiated features appeared to be higher as compared to these used for direct laser synthesis experiments described in **3.4.2 Linear 1D LIPSS and formation of nanoribbons** [11, 165]. The difference in the thermodynamic behavior of the material's conversion could be attributed to differences in the coupling of energy from the laser beam to the pre-patterned features and the heat dissipation, from the microstructures compared to continuous films. Here we have used a laser beam intensity of 1.65 MW/cm² (the laser wavelength was 532 nm as in the conventional laser-synthesis experiments) to convert the precursor material to MoS₂.

Figure 57 shows areas with sizes of 5 μm × 0.5 μm defined by e-beam scanning and subsequently converted to MoS₂ by laser scanning,

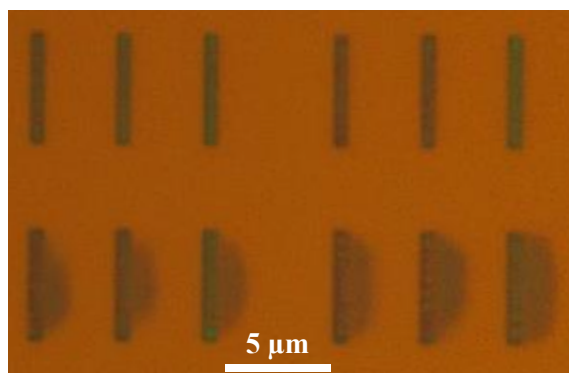


Figure 57 Rectangular features consisting of selectively e-beam irradiated regions of $(\text{NH}_4)_2\text{MoS}_4$ precursor followed by development in NMP. The features have been laser-irradiated along the horizontal direction to locally synthesize MoS_2 .

Each area in the top row was exposed to e-beam scanning for 2 s, while in the bottom row the features were overexposed for 4 s and exhibit a one sided “halo” that probably corresponds to imperfect focus of the electron beam.

The effect of laser annealing can be observed on microtexturing of the line features on the areas where the laser track intersects the microstructured precursor feature. The effect of post laser processing has been investigated using AFM topography mapping. Figure 58 shows the height and width of a single line within and outside a region that was scanned with a laser beam after the initial precursor pre-patterning that was obtained using e-beam irradiation. Here, a precursor film with an initial solution concentration of 48 mM was used.

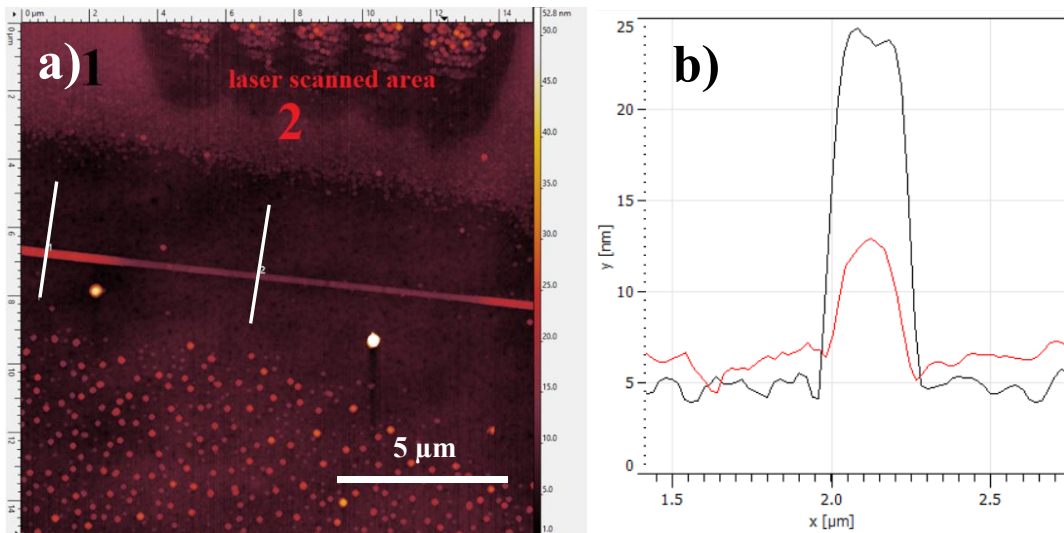


Figure 58 a) AFM image of a thin e-beam patterned line. The line was partially post-irradiated with a laser beam at a direction perpendicular to its length (across the line) with successive overlapping laser tracks to convert the precursor to MoS₂, b) Surface profiles corresponding to locations inside and outside the post-irradiated areas indicate the changes in height and width between the two areas. Red graph corresponds to area post-irradiated with laser, while the black graph, corresponds to the untreated patterned area. The locations of the two profiles are indicated by the two vertical lines 1 and 2.

Laser irradiation obviously induces a reduction of the original thickness of the pre-patterned feature, but it does not appear to reduce the width of the feature significantly.

Raman spectroscopy was used to detect the presence of MoS₂ in the post-irradiated regions. Raman spectra that feature the in and out of plane Raman modes that correspond to MoS₂ are shown in Figure 59 for various e-beam pre-patterning conditions.

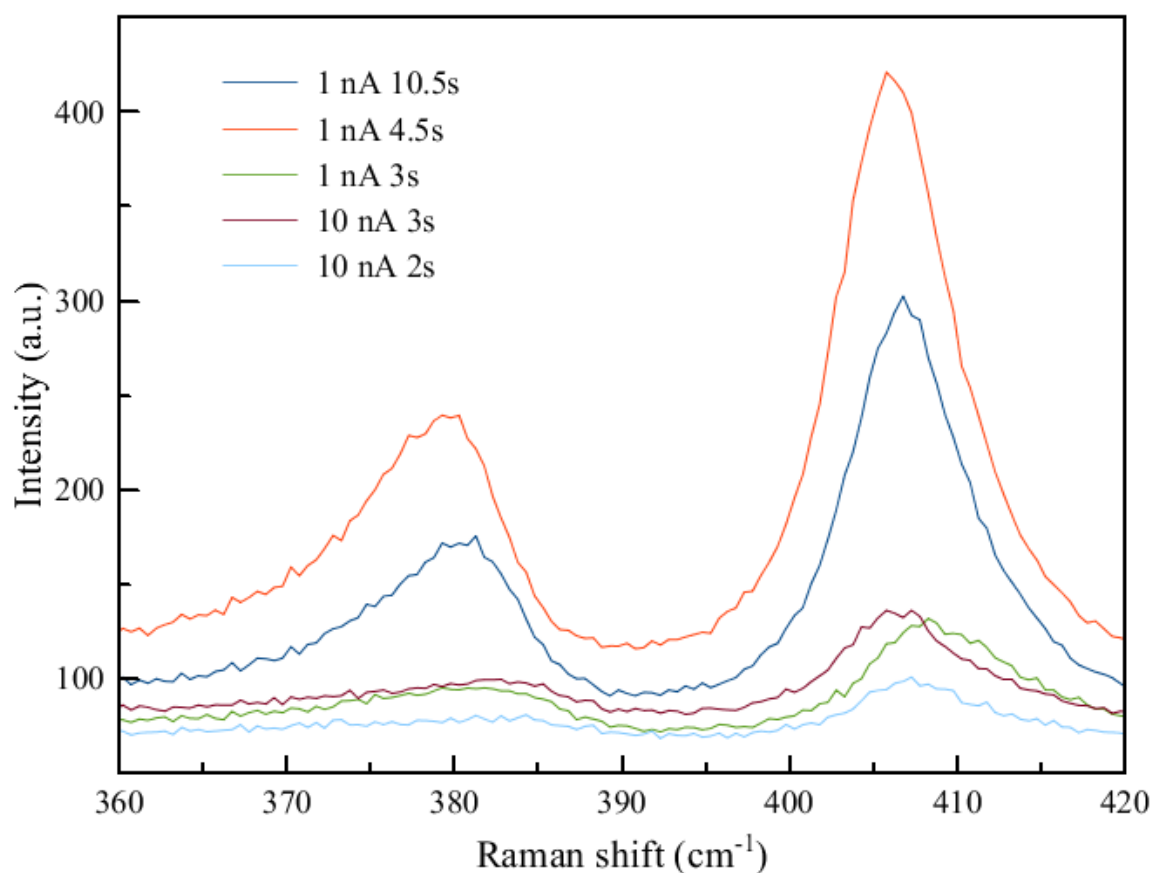


Figure 59 Raman spectra of MoS₂ thin line features converted from patterned precursor thin line features, which have been produced at different e-beam irradiation conditions.

5.5 Concluding remarks

We have presented a method for the pre-patterning of (NH₄)₂MoS₄ precursor films that utilizes e-beam irradiation in a conventional SEM and which allows to obtain patterned features in a manner similar to e-beam lithography. This method does not require specialty resists and requires a single step for its development that produces the patterned material. The e-beam patterned precursor features were shown to be convertible

towards MoS₂ patterned features with a width as narrow as ~ 200 nm by post-processing them with laser irradiation. It is reasonable to assume that this method is compatible with conventional thermal decomposition in a furnace with controlled atmosphere as well, possibly leading to higher quality MoS₂ films. This approach enables the decoupling of patterning and synthesis processes that occur simultaneously during previously demonstrated direct laser-synthesis of TMDs. Decoupling of patterning and synthesis allows for the optimization of each individual process, leading to finer structures consisting of better quality material. The results that have been presented here were obtained using an SEM device and have the potential for improvement by the use of specialty e-beam lithography equipment.

Conclusions

The present study has used a wide array of characterization techniques to revisit laser modification of established technological materials such as GaAs crystals and aluminum alloys and explore laser synthesis novel promising materials such as TMDCs.

The outcomes are listed as following:

- i. We have shown how continuous wave UV laser treatment of GaAs single crystals can induce LIPSS consisting of GaAs oxide due to periodically preferential oxidation. Such periodic sub-micron texturing could potentially act as a diffractive optical element or reduce reflective losses in photonic devices.
- ii. The same treatment conducted under higher laser intensities can locally create porous layers of GaAs oxide several hundred nm deep. Spatially selective growth of porous oxide can be used as an optical diffuser, a thermal, acoustic and electrical barrier or for sensing applications.
- iii. We have investigated the influence of the re-deposition of ablated material for scanning femtosecond pulse laser ablation of the D16T alloy under ambient conditions. When ablated material from the areas exposed to the earlier laser pulses partially redeposits to the areas that are exposed later, ablation is promoted, potentially leading to a non-uniform resulting profile of the ablated area.
- iv. We investigated the internal structure of micro-sized cones self-organized during femtosecond pulsed laser ablation. Due to re-deposition of ablated material on top

- of such conical microstructures, the top layer is non-uniform and oxidation is observed at depths of several μms . This could significantly affect the corrosive resistance, wear resistance and friction performance of the modified surface.
- v. We have presented the formation of sub-micron 1D and 2D LIPSS patterns simultaneous with direct laser synthesis of MoS_2 from spin-coated precursor films. This regular sub-micron patterning can lead to the formation of arrays of isolated ribbons with widths of ~ 200 nm and lengths of several micrometers.
 - vi. We have shown the resulting nanoribbon arrays to exhibit enhanced persistent photoconductivity, and their photocurrent increased by three orders of magnitude compared to their continuous film counterparts. LIPSS-based nanopatterning could be a promising route to enhance the photoelectrical properties of TMDs by defect engineering.

While GaAs is a widely applied material, there is still interest in exploring novel avenues, such as studies of porous GaAs layers obtained by electrochemical etching. Direct laser writing with UV lasers was shown to offer a simple and spatially selective way to obtain porous structures consisting of GaAs oxide; the present work reveals a uniform internal structure of the obtained porous oxide layer and a well-defined interface between the obtained porous oxide layer and the bulk. While some oxidation process lead to the loss of arsenic content, the present work shows a process that retains a high degree of stoichiometry in the obtained oxide layer. Additionally, periodic structures defined by periodically preferential oxidation are a novel development of the well-established LIPSS

phenomenon. The present work shows the quality of such structures induced by c.w. irradiation.

These insights may suggest an avenue for further study, focused on particular practical applications of deep porous layers involving photoluminescence and microfluidics phenomena and practical applications of periodic structures such as creating diffraction gratings for incoupling of IR light into GaAs planar waveguides on a small scale. Additionally, it is worth exploring whether it is possible to locally preserve the quality of the surface by depositing a porous oxide layer and then removing it.

Laser surface modification of aluminum alloys, such as creating conical microstructures, is of interest as a method of creating resistant surfaces for technical applications such as aerodynamics and marine construction. Research is conducted on controllably creating surface structures in this manner achieve control over the surface's wettability. This research works toward establishing a solid understanding of the redeposition of ablated alloy material. The strong effect of redeposition of ablated material on ablation with subsequent pulses is demonstrated; the top layer of ablated structures was shown to become substantially oxidized and contain internal voids and inhomogeneities of elemental composition. This prompts further investigation of corrosive properties obtained structures, which should allow to avoid a negative effect on corrosive resistance or possibly demonstrate a positive effect of the redeposited layer on corrosive properties.

Laser synthesis of TMDCs is a recently proposed method that has several important advantages: spatial selectivity and the ability to conduct synthesis in ambient conditions.

The present research expands on its possibilities by demonstrating synthesis simultaneously with creating arrays of ribbons separated by gaps of exposed substrate with a submicron period. Such structuring was demonstrated to be a promising way to control the population of shallow traps in MoS₂, leading to an increased and more persistent photoconductivity.

Persistent photoconductivity is a phenomenon that has recently attracted interest, promising applications in optical memory, neuromorphic devices and solar cells. The present research suggests a particularly simple way for the spatially selective synthesis of thin layers of a material with the persistent photoconductivity property.

Photoconductivity, however, is not the only possible application for the obtained MoS₂ thin films with a high edge length to surface area ratio. Further studies could explore the potential of the presented method in photocatalysis and humidity sensing.

From a theoretical point view, the present research outlines a very strong dependence of LIPSS forming in a thin film layer from the distribution of incident field in an underlying layer. Such a dependence, while reported and acknowledged in the literature, was not yet fully explained. A further study involving numerical simulations could help understand this phenomenon, potentially allowing to control structuring of arbitrary thin films.

Lastly, the present study presents evidence for direct densification of porous silicon under UV laser scanning. Completing this study with a demonstration of waveguiding would allow to propose practical applications such as rapid prototyping of porous silicon sensors.

Bibliography

- [1] W. M. Steen, *Journal of Optics A: Pure and Applied Optics*, vol. 5, pp. S3-S7, 2003.
- [2] N. K. Jain, et al., *International journal of machine tools and manufacture*, vol. 41, pp. 1573-1635, 2001.
- [3] O. Çakir, *Materials Processing Technology*, vol. 199, pp. 337-340, 2008.
- [4] M. Painuly, et al., *Journal of Solid State Electrochemistry*, pp. 1-68, 2023.
- [5] P. K. Shrivastava, et al., *Proceedings of the Institution of Mechanical Engineers, Part B: Journal of Engineering Manufacture*, vol. 228, pp. 799-825, 2014.
- [6] S. Alamri, et al., *Materials*, vol. 12, p. 1018, 2019.
- [7] M. Malinauskas, et al., *Light: Science & Applications*, vol. 5, pp. e16133-e16133, 2016.
- [8] J. Bonse, *Nanomaterials*, vol. 10, p. 1950, 2020.
- [9] A. Gillner, et al., *Journal of Materials Processing Technology*, vol. 167, pp. 494-498, 2005.
- [10] L. Santo, *International Journal of Surface Science and Engineering*, vol. 2, pp. 327-336, 2008.
- [11] O. A. Abbas, et al., *Scientific Reports*, vol. 11, p. 5211, 2021.
- [12] H. van Wolferen, et al., *Lithography: Principles, Processes and Materials*, pp. 133-148, 2011.
- [13] M. N. Ashfold, et al., *Chemical Society Reviews*, vol. 33, pp. 23-31, 2004.
- [14] C. B. Arnold, et al., *MRS bulletin*, vol. 32, pp. 9-15, 2007.
- [15] C. Sun, et al., *Sensors and Actuators A: Physical*, vol. 101, pp. 364-370, 2002.
- [16] Y. Wang, et al., *Progress in Quantum Electronics*, vol. 31, pp. 131-216, 2007.
- [17] H. A. Haus, *IEEE Journal of Selected Topics in Quantum Electronics*, vol. 6, pp. 1173-1185, 2000.
- [18] J. Bonse, et al., *Applied Physics A*, vol. 74, pp. 19-25, 2002.
- [19] C. Rödel, et al., *Applied Physics B*, vol. 103, pp. 295-302, 2011.
- [20] C. F. Bohren, et al., *Absorption and scattering of light by small particles*, John Wiley & Sons, 2008.
- [21] C. B. Schaffer, et al., *Measurement Science and Technology*, vol. 12, pp. 1784-1794, 2001.
- [22] Y. Siegal, et al., *Annual Review of Materials Science*, vol. 25, pp. 223-247, 1995.
- [23] D. Fisher, et al., *Physical Review E*, vol. 65, p. 016409, 2001.
- [24] R. R. Gattass, et al., *Nature photonics*, vol. 2, pp. 219-225, 2008.
- [25] K. Sugioka, et al., *Lab on a Chip*, vol. 14, pp. 3447-3458, 2014.

- [26] L. Li, et al., *Materials Today*, vol. 10, pp. 30-37, 2007.
- [27] D. Du, et al., *Applied Physics Letters*, vol. 64, p. 3071, 1994.
- [28] A. L. Gaeta, *Physical Review Letters* 84.16 (2000): 3582., vol. 84, p. 3582, 2000.
- [29] H. Dachraoui, et al., *Applied Physics A*, vol. 83, pp. 333-336, 2006.
- [30] H. P. Cheng, et al., *Physical Review B*, vol. 55, p. 2628, 1997.
- [31] H. Hu, et al., *Optics Express*, vol. 23, pp. 628-635, 2015.
- [32] C. Momma, et al., *Optical Communications*, vol. 129, pp. 134-142, 1996.
- [33] S. Link, et al., *Journal of Chemical Physics*, vol. 111, pp. 1255-1264, 1999.
- [34] Z. Nie, et al., *ACS nano*, vol. 8, pp. 10931-10940, 2014.
- [35] J. A. Cash, et al., *Physical Review Letters*, vol. 54, p. 2151, 1985.
- [36] M. Cardona, et al., *Physical Review B*, vol. 35, p. 6182, 1987.
- [37] M. Harb, *The Journal of Physical Chemistry B*, vol. 110, pp. 25308-25313, 2006.
- [38] B. Y. Mueller, et al., *Physical Review B*, vol. 87, p. 035139, 2013.
- [39] C. Voisin, et al., *Physical Review B*, vol. 69, p. 195416, 2004.
- [40] K. Dou, et al., *IEEE Journal on Selected Topics in Quantum Electronics*, vol. 4, pp. 567-578, 2001.
- [41] A. Nakhoul, et al., *Journal of Applied Physics*, vol. 130, p. 015104, 2021.
- [42] Z. Lin, et al., *Physical Review B*, vol. 77, p. 075133, 2008.
- [43] R. le Hazric, et al., *Applied Surface Science*, vol. 249, pp. 322-331, 2005.
- [44] H. O. Jeschke, et al., *Applied Surface Science*, vol. 197, pp. 839-844, 2002.
- [45] S. H. Chung, et al., *J. Biophotonics*, vol. 2, pp. 557-572, 2009.
- [46] S.T. M. Akkanen, et al., *Adv. Mater.*, vol. 34, p. 2110152, 2022.
- [47] M. Birnbaum, *Journal of Applied Physics*, vol. 36, pp. 3688-3689, 1965.
- [48] H. M. van Driel, et al., *Physical Review Letters*, vol. 49, pp. 1955-1958, 1982.
- [49] A. Beltaos, et al., *Journal of Applied Physics*, vol. 116, p. 204306, 2014.
- [50] M. J. M. J. Becher, *Front. Nanotechnol.*, vol. 5, p. 1227025, 2023.
- [51] H. Liu, et al., *Scientific reports*, vol. 5, p. 11756, 2015.
- [52] J. Bonse, et al., *Laser & Photonics Reviews*, vol. 14, p. 2000215, 2020.
- [53] J. E. Sipe, et al., *Phys. Rev. B*, vol. 27, p. 1141, 1983.
- [54] J. Bonse, et al., *Applied Physics*, vol. 106, p. 104910, 2009.
- [55] J. Bonse, et al., *J. Appl. Phys.*, vol. 97, p. 013538, 2005.
- [56] Z. Li, et al., *Appl. Surf. Sci.*, vol. 580, p. 152107, 2022.
- [57] F. Fragellakis, et al., *Applied Surface Science*, vol. 470, pp. 677-686, 2019.
- [58] J.-M. Romano, et al., *Appl. Surf. Sci.*, vol. 440, pp. 162-169, 2018.
- [59] I. Pavlov, et al., *arXiv preprint*, p. 1710.11405, 2017.

- [60] J. Bonse, et al., *IEEE Journal of selected topics in quantum electronics*, vol. 23, 2016.
- [61] J. Bonse, et al., *Laser-based Micro-and Nanoprocessing XI*, vol. 10092, pp. 114-122, 2017.
- [62] J. Z. P. Skolski, et al., *Physical Review B*, vol. 85, p. 075320, 2012.
- [63] M.Djouder, et al., *Applied Surface Science*, vol. 258, p. 2580, 2012.
- [64] K. Yee, *IEEE Transactions on Antennas and Propagation*, vol. 14, p. 302, 1966.
- [65] F. N. Harlow, "Los Alamos Scientific Laboratory Report LAMS-1956," 1955.
- [66] M. Huang, et al., *ACS Nano*, vol. 3, p. 4062, 2009.
- [67] K. Sokolowski-Tinten, et al., *Physical Review B*, vol. 61, p. 2643, 2000.
- [68] M. J. Abere, et al., *MRS Bulletin*, vol. 41, p. 969, 2016.
- [69] H. M. van Driel, et al., *Physical Review Letter*, vol. 49, p. 1955, 1982.
- [70] A. E. Siegman. et al., *IEEE Journal of Quantum Electronics*, vol. 22, p. 1384, 1986.
- [71] A. V. Dostovalov, et al., *Applied Surface Science*, vol. 491, pp. 650-658, 2019.
- [72] M. V. Shugaev, et al., *Physical Review B*, vol. 96, p. 205429, 2017.
- [73] A. Rudenko, et al., *Scientific Reports*, vol. 7, p. 12306, 2017.
- [74] T. T. D. Huyhn, et al., *Appl. Phys. A*, vol. 116, pp. 1429-1435, 2014.
- [75] T. R. Anthony, et al., *J. Appl. Phys.*, vol. 48, p. 3888, 1977.
- [76] A. V. Dostovalov, et al., *Optics Express*, vol. 26, pp. 7712-7723, 2018.
- [77] M. Mastellone, et al., *Materials*, vol. 15, p. 1378, 2022.
- [78] J. Cui, et al., *Applied Surface Science*, vol. 394, pp. 125-131, 2017.
- [79] S. Durbach, et al., *Applied Surface Science*, vol. 622, p. 156927, 2023.
- [80] S. Murarka, *Applied Physics Letters*, vol. 26, pp. 180-181, 1975.
- [81] D. Aspnes, et al., *Journal of The Electrochemical Society*, vol. 128, p. 590, 1981.
- [82] Z. Lu, et al., *The Journal of chemical physics*, vol. 93, pp. 7951-7961, 1990.
- [83] C. P. Gonschior, et al., *J. Non Cryst. Solids*, vol. 361, pp. 106-110, 2013.
- [84] Z. Wang, et al., *Micromachines*, vol. 6, pp. 1606-1616, 2015.
- [85] L. Romoli, et al., *CIRP Annals - Manufacturing Technology*, vol. 63, pp. 229-232, 2014.
- [86] J.-M. Guay, et al., *ArXiv preprint 1609.02874v1*, p. 1609.02874v1, 2016.
- [87] A. Y. Vorobyev, et al., *Physical Review Letters*, vol. 102, p. 234301, 2009.
- [88] T. Knüttel, et al., *Journal of Laser Micro Nanoengineering*, vol. 8, pp. 222-229, 2013.
- [89] A. Y. Vorobyev, et al., *Laser Photonics Reviews*, vol. 7, pp. 385-407, 2012.
- [90] E. Rebollar, et al., *Biomaterials*, vol. 29, pp. 1796-1806, 2008.
- [91] N. Epperlein, et al., *Applied Surface Science*, vol. 418, pp. 420-424, 2017.

- [92] S. Rung, et al., *Lubricants*, vol. 7, p. 43, 2019.
- [93] J. Schille, et al., *Lubricants*, vol. 8, p. 33, 2020.
- [94] C. A. Zuhlke, et al., *Applied surface Science*, vol. 283, pp. 648-653, 2013.
- [95] Y. Li, et al., *Applied Surface Science*, vol. 324, pp. 775-783, 2013.
- [96] D. H. Kam, et al., *Journal of micromechanics and microengineering*, vol. 22, p. 105019, 2012.
- [97] G. Yakovlev, et al., *Semiconductors*, vol. 52, pp. 1004-1011, 2018.
- [98] X. Sheng, et al., *Laser & Photonics Reviews*, vol. 9, pp. L17-L22, 2015.
- [99] T. P. Chow, et al., *IEEE Transactions on Electron Devices*, vol. 64, pp. 856-873, 2017.
- [100] F. Nandjou, et al., *Journal of Physics D: Applied Physics*, vol. 50, p. 124002, 2017.
- [101] N. M. Burford, et al., *Optical Engineering*, vol. 56, p. 010901, 2017.
- [102] H. Fukui, *IEEE Transactions on Electron Devices*, vol. 26, pp. 1032-1037, 1979.
- [103] V. Umansky, et al., *Journal of Crystal Growth*, vol. 311, pp. 1658-1661, 2009.
- [104] J. S. Blackmore, *Journal of Applied Physics*, vol. 53, pp. R123-R181, 1982.
- [105] G. E. Jellison Jr, et al., *Optical Materials*, vol. 1, pp. 151-160, 1992.
- [106] T. Ishii, et al., *Journal of the Electrochemical Society*, vol. 124, pp. 1784-1794, 1977.
- [107] V. L. Berkovits, et al., *Surface Science*, vol. 444, pp. 26-32, 1999.
- [108] E. Higham, in *28th International Conference on Compound Semiconductor Manufacturing Technology, CS Mantech Conference*, 2013.
- [109] P. D. Ye, et al., *IEEE Electron Device Letters*, vol. 24, pp. 209-211, 2003.
- [110] S. M. Spitzer, et al., *Journal of the Electrochemical Society*, vol. 122, pp. 397-402, 1975.
- [111] T. Grabnic, et al., *Surface Science*, vol. 692, p. 121516, 2020.
- [112] R. Tominov, et al., *Journal of Physics: Conference Series*, vol. 1410, p. 012233, 2019.
- [113] R. Korbutowicz, et al., *Semiconductor technologies (2010) 105–132.*, pp. 105-132, 2010.
- [114] A. A. Ismail, et al., *Journal of hazardous materials*, vol. 342, pp. 519-526, 2018.
- [115] T. Miyata, et al., *Journal of Luminescence*, vol. 87, pp. 1183-1185, 2000.
- [116] V. B. Kumar, et al., *Energy & Fuels*, vol. 30, p. 7419–7427, 2016.
- [117] S. Pearton, et al., *Applied Physics Reviews*, vol. 5, p. 011301, 2018.
- [118] S. Stepanov, et al., *Reviews on Advanced Materials Science*, vol. 44, pp. 63-86, 2016.
- [119] H. H. Wang, et al., *Journal of Applied Physics*, vol. 87, pp. 2629-2633, 2000.
- [120] I. S. Han, et al., *Applied Physics Letters*, vol. 118, p. 142101, 2021.

- [121] Y. R. Wang, et al., *Optics Express*, vol. 28, pp. 32529-32539, 2020.
- [122] A. A. Ionin, et al., *Applied Physics B*, vol. 111, pp. 419-423, 2013.
- [123] N. Ali, et al., *Optics & Laser Technology*, vol. 108, pp. 107-115, 2018.
- [124] B. K. Nayak, et al., *Optics and Lasers in Engineering*, vol. 48, pp. 940-949, 2010.
- [125] K. M. T. Ahmmed, et al., *Optics and Lasers in Engineering*, vol. 66, pp. 258-268, 2015.
- [126] N. Singh, et al., *Journal of Laser Applications*, vol. 18, pp. 242-244, 2006.
- [127] A. T. Tsubaki, et al., *Applied Surface Science*, vol. 419, pp. 778-787, 2017.
- [128] Z. Liu, et al., *Applied Surface Science*, vol. 247, pp. 294-299, 2005.
- [129] A. K. Geim, et al., *Nature materials*, vol. 6, pp. 183-191, 2007.
- [130] S. Manzeli, et al., *Nature Review Materials*, vol. 2, pp. 1-15, 2017.
- [131] X. Wen, et al., *InfoMat*, vol. 1, pp. 317-337, 2019.
- [132] B. Scharf, et al., *Physical review letters*, vol. 119, p. 127403, 2017.
- [133] Y.-T. Hsu, et al., *Nature communications*, vol. 8, p. 14985, 2017.
- [134] C. Cong, et al., *Advanced Optical Materials*, vol. 6, p. 1700767, 2018.
- [135] A. Taffelli, et al., *Sensors*, vol. 21, p. 2758, 2021.
- [136] S. A. Han, et al., *Nano Convergence*, vol. 2, pp. 1-14, 2015.
- [137] S. Rahman, et al., *Nanoscale Horizons*, vol. 7, pp. 849-872, 2022.
- [138] A. Daus, et al., *Nature Electronics*, vol. 4, pp. 495-501, 2021.
- [139] K. S. Kim, et al., *Nature Communications*, vol. 10, p. 4701, 2019.
- [140] Q. Zhao, et al., *Mater. Horiz.*, vol. 7, pp. 252-262, 2020.
- [141] H. Shang, et al., *Chem. Eng. Sci.*, vol. 195, pp. 208-217, 2019.
- [142] A. Rose, *Proceedings of the IRE*, vol. 43, pp. 1850-1869, 1955.
- [143] H. Park, et al., *Communications Materials*, vol. 2, p. 94, 2021.
- [144] H. Hayat, et al., *Sensors*, vol. 19, p. 3648, 2019.
- [145] A. George, et al., *npj 2D Materials and Applications*, vol. 5, p. 15, 2021.
- [146] A. Di Bartolomeo, et al., *Nanotechnology*, vol. 28, p. 214002, 2017.
- [147] C. Chandan, et al., *Applied Physics Letters*, vol. 18, 2021.
- [148] A. Sumanth, et al., *Journal of Physics D: Applied Physics*, vol. 55, p. 393001, 2022.
- [149] V. M. Poole, et al., *Scientific Reports*, vol. 7, pp. 1-6, 2017.
- [150] L. Lu, et al., *RSC Advances*, vol. 8, pp. 16455-1663, 2018.
- [151] A. Abelenda, et al., *Solar Energy Materials and Solar Cells*, vol. 137, pp. 164-168, 2015.
- [152] P. J. Snyder, et al., *Small*, vol. 13, p. 1700481, 2017.
- [153] H. Fang, et al., *Nano Letters*, vol. 12, pp. 3788-3792, 2012.

- [154] J. N. Coleman, et al., *Science*, vol. 331, pp. 568-571, 2011.
- [155] J. Liu, et al., *Journal of Materials Chemistry*, vol. 5, pp. 11239-11245, 2017.
- [156] K.-K. Liu, et al., *Nano Letters*, vol. 12, pp. 1538-1544, 2012.
- [157] M. Mattinen, et al., *Advanced Materials Interfaces*, vol. 8, p. 2001677, 2021.
- [158] U. Hutten, et al., *2D Material*, vol. 8, p. 045015, 2021.
- [159] M Nakano, et al., *Nano Letters*, vol. 9, pp. 5595-5599, 2017.
- [160] M. Samadi, et al., *Nanoscale Horizons*, vol. 3, pp. 90-204, 2018.
- [161] K.-K. Liu, et al., *Nano letters*, vol. 12, pp. 1538-1544, 2012.
- [162] J. Yang, et al., *Nanoscale*, vol. 7, p. 9311, 2015.
- [163] H. Yang, et al., *Chemistry of Materials*, vol. 29, pp. 5772-5776, 2017.
- [164] O. A. Abbas, et al., *Scientific Reports*, vol. 10, p. 1696, 2020.
- [165] A. V. Averchenko, et al., *Materials Today Advances*, vol. 17, p. 100351, 2023.
- [166] C. C. Huang, et al., *Nano Lett.*, vol. 16, pp. 2463-2470, 2016.
- [167] K. Tian, et al., *Thin Solid Films*, vol. 668, pp. 69-73, 2018.
- [168] G. Siegel, et al., *APL Mater.*, vol. 3, p. 56103, 2015.
- [169] S. Durbach, et al., *ACS nano*, vol. 16, pp. 10412-10421, 2022.
- [170] M. Wang, et al., *ACS Nano*, vol. 14, pp. 11169-11177, 2020.
- [171] H. Föll, et al., "Mater. Sci. Eng. R Rep.," *Mater. Sci. Eng. R Rep.*, vol. 39, pp. 93-141, 2002.
- [172] M. P. Stewart, et al., *Adv. Mater.*, vol. 12, pp. 859-869, 2000.
- [173] E. Vazsonyi, et al., *Thin Solid Films*, vol. 388, pp. 295-302, 2001.
- [174] O. Kuntiy, et al., *Adv. Mater. Sci. Eng.*, 2022.
- [175] D. H. Ge, et al., *Electrochim. Acta*, vol. 88, pp. 141-146, 2013.
- [176] H. Sohn, in *Handbook of Porous Silicon*, 2014, pp. 231-243.
- [177] A. Loni, et al., *Thin Solid Films*, vol. 276, pp. 143-146, 1996.
- [178] V. Torres-Costa, et al., *J. Mater. Sci.*, vol. 45, pp. 2823-2838, 2010.
- [179] T. Hutter, et al., *Proceedings of COMSOL Conference*, 2010.
- [180] S.M. Weiss, et al., *Physica E Low Dimens.*, vol. 41, pp. 1071-1075, 2009.
- [181] P. Azuelos, et al., *Journal of Optics*, vol. 20, p. 085301, 2018.
- [182] A. M. Rossi, et al., *Appl. Phys. Lett.*, vol. 78, pp. 3003-3005, 2001.
- [183] K. Kim, et al., *Opt. Express*, vol. 21, pp. 19488-19497, 2013.
- [184] M. T. Postek, et al., *Scanning*, vol. 18, pp. 269-274, 1996.
- [185] J. Hamuyuni, et al., *Encyclopedia of Physical Organic Chemistry*, pp. 1-23, 2017.
- [186] T. J. Barnes, et al., *Int. J. Pharm.*, vol. 417, pp. 61-69, 2011.
- [187] T. Stephan, *Planet. Space Sci.*, vol. 49, pp. 859-906, 2001.

- [188] "STIL – CCS Optima – Operation and maintenance manual CCS-102-P1 Rev. S," [Online]. Available: https://www.music.mcgill.ca/caml/lib/exe/fetch.php?media=equipment:ccs_optima_user_manual-rev_s.pdf. [Accessed 30 07 2023].
- [189] H. Zeng, et al., *Phys. Rev. B*, vol. 86, p. 241301, 2012.
- [190] B. Chakraborty, et al., *J. Raman Spectrosc.*, vol. 44, pp. 92-96, 2013.
- [191] S. E. Panasci, et al., *Applied Physics Letters*, vol. 119, 2021.
- [192] I. A. Salimon, et al., *Metals*, vol. 10, p. 114, 2020.
- [193] I. A. Salimon, et al., *Solid State Sciences*, vol. 128, p. 106887, 2022.
- [194] A. Ionin, et al., *Applied Physics B*, vol. 111, pp. 419-423, 2013.
- [195] S. Ono, et al., *Electrochimica Acta*, vol. 110, pp. 393-401, 2013.
- [196] "Nist x-ray photoelectron spectroscopy database," [Online]. Available: <https://srdata.nist.gov/xps/Default.aspx>.
- [197] L. Brown, et al., *The Journal of Physical Chemistry*, vol. 100, pp. 7849-7853, 1996.
- [198] B. Schwartz, *C R C Critical Reviews in Solid State Sciences*, vol. 5, pp. 609-624, 1975.
- [199] F. Bastiman, et al., *Journal of Physics: Conference Series*, vol. 209, p. 012066, 2010.
- [200] L. Kucharikova, et al., *Metals*, vol. 8, p. 581, 2018.
- [201] I. A. Salimon, et al., *Micromachines*, vol. 14, p. 1036, 2023.
- [202] A. Castellanos-Gomez, et al., *Nano Letters*, vol. 12, pp. 3187-3192, 2012.
- [203] J. L. Brito, et al., *Thermochimica Acta*, vol. 256, pp. 325-338, 1995.
- [204] T. T. D. Huynh, et al., *Applied Physics A*, vol. 116, pp. 1429-1435, 2014.
- [205] M. Mastellone, et al., *Nano Letters*, vol. 21, pp. 4477-4483, 2021.
- [206] A. N. Desikan, et al., *Journal of Physical Chemistry*, vol. 95, pp. 10050-10056, 1991.
- [207] N. Ott, et al., *J. Appl. Phys.*, vol. 95, pp. 497-503, 2004.
- [208] J. S. Fletcher, *Biointerphases*, vol. 10, 2015.
- [209] S. Hohm, et al., *Applied physics A*, 110(3), 5, vol. 110, p. 5, 2013.
- [210] C. V. Shank, et al., *Physical Review Letters*, vol. 50, p. 454, 1983.
- [211] N. M. Bulgakova, et al., *Applied Physics A*, vol. 73, pp. 199-208, 2001.
- [212] J. E. Sipe, et al., *Physical Review B*, vol. 27, p. 1141, 1983.
- [213] A. Margiolakis, et al., *Physical Review B*, vol. 98, p. 224103, 2018.
- [214] J. I. Ahuir-Torres, et al., *Optics and Lasers in Engineering*, vol. 103, pp. 100-109, 2018.
- [215] M. Mezera, et al., *Journal of laser micro nanoengineering*, vol. 13, pp. 105-116, 2018.

- [216] S. Hohm, *J. Appl. Phys.*, vol. 112, p. 014901, 2012.
- [217] C. Homann, et al., *Applied Physics B*, vol. 104, pp. 783-791, 2011.
- [218] E. M. Conwell, et al., *IEEE Transaction on Electron Devices*, vol. 13, pp. 22-27, 1966.